



UNIVERSITAT POLITÈCNICA
DE CATALUNYA
BARCELONATECH

Development of high-capacity substation connectors compatible with HTLS technology

by
Francesca Capelli

ADVERTIMENT La consulta d'aquesta tesi queda condicionada a l'acceptació de les següents condicions d'ús: La difusió d'aquesta tesi per mitjà del repositori institucional UPCommons (<http://upcommons.upc.edu/tesis>) i el repositori cooperatiu TDX (<http://www.tdx.cat/>) ha estat autoritzada pels titulars dels drets de propietat intel·lectual **únicament per a usos privats** emmarcats en activitats d'investigació i docència. No s'autoritza la seva reproducció amb finalitats de lucre ni la seva difusió i posada a disposició des d'un lloc aliè al servei UPCommons o TDX. No s'autoritza la presentació del seu contingut en una finestra o marc aliè a UPCommons (*framing*). Aquesta reserva de drets afecta tant al resum de presentació de la tesi com als seus continguts. En la utilització o cita de parts de la tesi és obligat indicar el nom de la persona autora.

ADVERTENCIA La consulta de esta tesis queda condicionada a la aceptación de las siguientes condiciones de uso: La difusión de esta tesis por medio del repositorio institucional UPCommons (<http://upcommons.upc.edu/tesis>) y el repositorio cooperativo TDR (<http://www.tdx.cat/?locale-attribute=es>) ha sido autorizada por los titulares de los derechos de propiedad intelectual **únicamente para usos privados enmarcados** en actividades de investigación y docencia. No se autoriza su reproducción con finalidades de lucro ni su difusión y puesta a disposición desde un sitio ajeno al servicio UPCommons. No se autoriza la presentación de su contenido en una ventana o marco ajeno a UPCommons (*framing*). Esta reserva de derechos afecta tanto al resumen de presentación de la tesis como a sus contenidos. En la utilización o cita de partes de la tesis es obligado indicar el nombre de la persona autora.

WARNING On having consulted this thesis you're accepting the following use conditions: Spreading this thesis by the institutional repository UPCommons (<http://upcommons.upc.edu/tesis>) and the cooperative repository TDX (<http://www.tdx.cat/?locale-attribute=en>) has been authorized by the titular of the intellectual property rights **only for private uses** placed in investigation and teaching activities. Reproduction with lucrative aims is not authorized neither its spreading nor availability from a site foreign to the UPCommons service. Introducing its content in a window or frame foreign to the UPCommons service is not authorized (*framing*). These rights affect to the presentation summary of the thesis as well as to its contents. In the using or citation of parts of the thesis it's obliged to indicate the name of the author.



UNIVERSITAT POLITÈCNICA
DE CATALUNYA
BARCELONATECH

DEVELOPMENT OF HIGH-CAPACITY SUBSTATION CONNECTORS COMPATIBLE WITH HTLS TECHNOLOGY

by

Francesca Capelli

A thesis submitted in partial fulfillment
of the requirements for the degree of
Doctor of Philosophy in Electrical Engineering

Supervisor:

Prof. Jordi-Roger Riba Ruíz

Department of Electric Engineering
Universitat Politècnica de Catalunya
Barcelona, Spain
December, 2016



ELECTRIC ENGINEERING DEPARTMENT



Abstract

In the last years there has been a considerable increase in electrical power consumption; moreover, there has been a growing in incorporation of generation sources of renewable technologies. Previsions suggest that this trend will be growing in the coming years. This challenge requires the construction of new power lines or the increase of the capacity of existing power lines. However, due to the difficulty in planning new tower sites and the related environmental impacts and social concerns, it is often extremely difficult to build new transmission and distribution lines, especially in urban areas or in regions of ecological interest. This problem leads to the energy sector to search a feasible solution to solve saturation problems of electrical lines due to increased demand and generation. A solution that some countries have chosen, due to its technological and economic viability, is replacement of conventional conductors with others operating at high temperature, known as HTLS (High-Temperature Low-Sag) conductors. HTLS conductors, with an almost identical section of conventional ones, allow increasing the nominal current capacity, with an allowable increase in operating temperature. Some HTLS conductors can operate continuously at temperatures as high as 250 °C, due to their innovative design with strength core that allows reaching high temperature without compromising mechanical resistance of conductor.

Although cables manufacturers have developed a new methodology design to increase the capacity of the lines, manufacturers of components involved in power transmission and distribution, such as substation connectors, have not developed yet devices compatibles with this technology.

The thesis presented by the author is dedicated to develop a new family of high-capacity substation connectors compatible with HTLS conductor's technology. The new family of high-capacity connectors to be developed in this thesis must pass the mandatory standard tests dictated by the international regulations. Therefore, the aim of this thesis is to improve the materials used in the connectors and the installation procedure to fulfill the thermal and mechanical constraints of the standard tests and to develop software tools to aid the optimal thermal design of such connectors.

The doctoral thesis has been carried out by means of collaboration agreement between UPC and the company SBI Connectors, within the framework of the Industrial Doctorates Plan, promoted by the Generalitat de Catalunya. Furthermore, the thesis is developed within the project Retos de Colaboración RTC-2014-2862-3 "Desarrollo de Conectores de Subestación compatibles con Tecnología HTLS y las Técnicas de Ensayo Asociadas", which main objective is the development of high-capacity substation connectors and associated testing methods. The project, supported by Spanish Ministry of Economy and Competitiveness, was granted in 2014 under the Plan for Scientific and Technical Research and Innovation for 2013-2016.



Acknowledgments

First of all I would like to thank my advisor, Jordi Riba. Words are not sufficient to express all my gratitude to him. Just wanted to tell that I am truly thankful for his help, guidance, and the sincere affection with which he has accompanied and supported me during these three years.

A special thank also to SBI Connectors, in particular to Josep Sanllehi, for giving me the opportunity to undertake this doctorate. Thanks for showing a lot of faith towards me, for listening always with interest to my proposals and for supporting and recognizing my projects. I would like to thank him also for always make me feel part of SBI although I was not physically there during my PhD.

I would like to thank all the staff of AMBER, MCIA and SBI Connectors, especially my colleagues Albert Rodriguez, Carlos Abomailek, David Gonzalez and Pau Casals. I have learned a lot working with them and I will be always grateful for their precious assistance and support in the development of my thesis, but, above all, for their friendship.

Moreover, I would like to thank Irene Pla and Jose Bailón for their support in experimental measurements.

I am very grateful to Elisa Rupérez, for advising me with the part of my thesis dedicated to aluminum alloys, but, above all, for her patience and willingness during these three years. A special thank also to Joan Esteve, for dedicating his time to develop a system for my resistivity measurements and give me access to the laboratory facilities of his faculty. Moreover I would like to thank Carlos David Segarra, for solving some doubts about thermal equations.

I would like to thank my husband Jesús, my North Star, who have supported me during these years, both by keeping me always happy and optimist and cheering myself up when things were not going in the right direction and I was lost. He has always had the superpower to make all my fears disappear with a smile. I will be grateful forever for his love.

Un ringraziamento speciale va a mio padre Dino e mia madre Ilde. Da loro ho ricevuto l'educazione, l'esempio e l'affetto e se oggi sono quella che sono è solo grazie al loro infinito amore. La distanza può separare due corpi, ma non due cuori.

Finalmente, quiero expresar mi más sincero agradecimiento a Cecilio, Josefa y Jaime, por darme el calor de una familia y quererme como a una hija y una hermana.

Contents

Abstract	3
Acknowledgments	5
List of Figures	9
List of tables	13
1. Introduction	15
1.1 Objectives	19
1.2 Main Contributions	19
1.3 Thesis Publications	20
1.3.1 Conferences:	20
1.3.2 Journals:	21
2 State of the art	22
2.1 Substation Connectors	22
2.2 Testing standard for substation connectors	24
2.2.1 Temperature rise test	25
2.2.2 Thermal cycle test	26
2.2.3 Peak withstand current and short-time withstand current test	27
2.2.4 Short-circuit test	28
2.2.5 Other tests	28
2.3 HTLS Technology	29
2.3.1 Materials and properties	30
3. Materials for high-capacity substation connectors	34
3.1 Introduction	34
3.2 Microstructure of Al-Mg-Si alloys	35
3.3 Heat treatments	40
3.4 Chemical modification	42
3.4.1 Modification of A356.0 alloy for substation connectors	43
3.4.2 Microstructure of un-modified and Sr-modified A356.0 alloy	44
3.4.3 Effect of the heat treatment and the chemical modification on electrical conductivity and thermal properties of A356.0 alloy	45
3.5 Characterization of physical properties in un-modified and Sr-modified A356.0 alloy	45
3.5.1 Mechanical properties	45
3.5.2 Electrical Properties	49
3.5.3 Thermal conductivity	56
4. Contact Resistance	61
4.1 Chemical cleaning to reduce the contact resistance	61
4.1.1 Analyzed substation connectors and installation procedures	62
4.1.2 Contact resistance measurements	63
4.1.3 Components of connector's resistance	64
4.2 Improved thermal behavior due to the chemical cleaning	64
4.2.1 Traditional Installation Procedure vs Chemical Cleaning	65
4.2.2 Experimental validation of the thermal improvement due to the chemical cleaning	66
4.3 Determination of temperature dependence of contact resistance	72
4.3.1 Results	73

4.4	GA-Optimized Fractal Model to Predict the Constriction Resistance of Substation Connectors	74
4.4.1	Surface Roughness Parameters	76
4.4.2	The proposed GA-Optimized Fractal Model	77
4.4.3	Reference ECR Models	80
4.4.4	Experimental.....	82
4.4.5	Results	85
5.	Electromagnetic-thermal model for high-capacity substation connectors	89
5.1	State of the art.....	89
5.1.1	Ampacity models for conductors	89
5.2	Electromagnetic-thermal simulation of power devices.....	91
5.3	Electromagnetic-Thermal model for substation connectors.....	93
5.3.1	Electromagnetic analysis	93
5.3.2	Thermal analysis	93
5.3.3	Heat transfer coefficients	94
5.4	3D-Finite Element Analysis of the Short-Time and Peak Withstand Current Tests in Substation Connectors.....	97
5.4.1	Introduction	97
5.4.2	The Short-Time Withstand Current And Peak Withstand Current	99
5.4.3	The Analyzed Connectors.....	100
5.4.4	The 3D-FEM Model.....	101
5.4.5	Simulation and experimental results	103
5.5	3D-Finite element analysis of the temperature rise test in substation connectors.....	109
5.5.1	Introduction	109
5.5.2	The 3D-FEM model	110
5.5.3	The analyzed high-capacity and bimetallic connectors	112
5.5.4	Simulation and Experimental Results	113
6.	Testing and validation of High-Capacity substation connectors	119
6.1	Short time and peak withstand current test	119
6.1.1	Requirements	119
6.1.2	Test Setup	120
6.1.3	Results	121
6.2	Temperature rise test.....	122
6.2.1	Thermal requirements.....	122
6.2.2	Test Setup	123
6.2.3	Results	124
7.	Conclusions	126
	References.....	130
	Appendix	138
A.	Inductance of the testing loop.....	138
	Calculation of the inductance of conductive nonmagnetic conductors: round conductor forming a circular loop	138
	Optimization of short-circuit test based on finite-element analysis	142

List of Figures

Figure 2.1. Electrical substation	22
Figure 2.2. Substation connectors and their position in an electrical substation.	23
Figure 2.3. Results of temperature rise test performed at 100%, 125% and 150% of n % of nominal current established for conductor.	26
Figure 2.4. General graph of an heat cycle provided by the IEC 61238-1 standard.....	27
Figure 2.5. Short-time withstand current (I_k) and peak withstand current (I_p).....	28
Figure 2.6. Method for increasing current line capacity.	30
Figure 3.1. Ashby plot of different properties involved in material's selection for high voltage applications. a) Electrical resistivity vs cost and b) Strength vs density.	35
Figure 3.2. Al-Si phase diagram.....	36
Figure 3.3. Microstructure obtained with different solidification rate. a) Sand cast. b) Permanent mold cast and c) die cast. (from [45]).	40
Figure 3.4. Temperature and time required for T6 (a) and T4 heat treatments (b)	41
Figure 3.5. precipitation sequence for A356.0 alloy proposed by Dutta and Allen [35].	42
Figure 3.6. Microstructure of unmodified (a) and modified (b) hypo-eutectic alloy.	43
Figure 3.7. Different phases of the A356-Sr modified sample's casting.	44
Figure 3.8. . General stress–strain curve. Engineering stress (σ) is shown as a function of engineering strain (ϵ)....	46
Figure 3.9. a) Drawing and dimensions of the test specimen used in the mechanical tensile tests. b) Specimen gripping system employed for the experimental test.	47
Figure 3.10. Vertical bench of 5 tons used to perform the mechanical tensile tests.....	48
Figure 3.11. Scheme of the test setup for measuring electrical resistivity of the alloys.....	51
Figure 3.12. Experimental setup for the measurement of the temperature coefficient of electrical resistivity a) Simplified scheme of the test setup for the measurement from room temperature to 200°C. b) Stabilized current source and voltage and current measurement system. c) Temperature-controlled electric oven d) Resistance measurement of the test specimen at temperature of boiling point of liquid nitrogen stored in a vacuum flask. e) Resistance measurement of the test specimen at temperature of sublimation temperature of dry ice placed in an insulated box	53
Figure 3.13. Test specimen use for the measurement of thermal conductivity.	57
Figure 3.14. Experimental setup for the measurement of thermal conductivity.	58
Figure 3.15. Semplificated scheme wich explain the mechanism of thermal conduction. the quantity of heat, ΔQ , is transmitted during time Δt through a thickness ΔL , in a direction normal to a surface of area A, due to a temperature difference ΔT	59
Figure 3.16. Example of 3D-FEM thermal simulation used to estimate convective and radiative heat flux on external boundaries of the testing specimens.	60
Figure 4.1. Conductor's surfaces on the micro scale. Current flow is restricted to contact points established during installation.	61
Figure 4.2. The substation connectors analyzed. a) S330TLS t-type connector. b) S330SLS coupler connector.c) S330SNS coupler connector.....	62
Figure 4.3. Resistance measurement with the Kelvin 4-wire method.....	63

Figure 4.4. Components of contact resistance for the three installation procedures analyzed.....	64
Figure 4.5. The substation connectors analyzed. a) S330TLS t-type connector. b) S330SLS coupler connector.c) S285TLS t-type connector	66
Figure 4.6. Experimental temperature rise test. Testing loop with connectors with different installation procedures. Connectors assembled with procedure No. 1 are indicated in red, whereas connectors installed with procedure No. 2 in blue.	67
Figure 4.7. a) Results of the experimental temperature rise test. In red it is shown the temperature of the connectors installed with procedure No.1, while in blue connectors assembled with procedure No. 2. b) Zoom of the third step, performed at 150% of nominal c current.	68
Figure 4.8. Heat-cycle test. Experimental setup.	69
Figure 4.9. Determination of the temperature dependence of contact resistance. Heating of the testing loop. Resistance measurement with the 4-wires method and thermocouples' position.	73
Figure 4.10. Contact resistance as a function of the contact interface temperature. Measured values and linear approximation.....	74
Figure 4.11. . a) Results of the experimental short time withstand current tests. In red it is shown the temperature of the connectors installed with procedure No.1, while in blue connectors assembled with procedure No. 2.....	72
Figure 4.12. Scheme of an electrical joint with conforming surfaces in contact.....	76
Figure 4.13. GA-based optimized fractal model of the ECR.....	80
Figure 4.14. Contact interfaces ($Aa1 = Aa2 = Aa$) between the conductors and the substation connector.	82
Figure 4.15. Analyzed substation connectors. a) S330TLS T-type substation connector. b) S330SLS coupler connector. c) S330SNS coupler connector.	83
Figure 4.16. Roughness measurements performed with Mitutoyo Surftest 211 surface roughness tester on both connector's and conductor's surfaces.....	84
Figure 4.17. ECR measurement by using a micro-ohm meter based on the 4-terminal method.	85
Figure 4.18. Apparent area (in blue) of contact in the three analyzed substation connectors a) S330TLS, b) S330SLS and c) S330SNS.....	85
Figure 4.19. Plot of the three-dimensional fractal surface [m] of a 100 μ m x100 μ m square section (0.01 mm ² with a resolution of 500x500 points) of the contact interface of the substation connectors analyzed. a) S330TLS. b) S330SLS. c) S330SNS.	87
Figure 5.1. Estimated ACSS conductor temperature using different analyzed correlations (in black) and experimental measurements (in red).....	96
Figure 5.2. Short time withstand current (I_k) and peak withstand current (I_p).	100
Figure 5.3. a) Two-cap J33SPK coupler substation connector. b) Bimetallic YAT450AM20C T connector.	100
Figure 5.4. a) Model A. Mesh of the two-cap J33SPK coupler substation connector. b) Model B used to validate the 3D-FEM model proposed in this thesis. Mesh of the YAT450AM20C bimetallic compression connector.....	101
Figure 5.5. Experimental voltage and current values during the peak withstand current test.	104
Figure 5.6. Experimental voltage and current values during the short-time withstand current test.....	104
Figure 5.7. Model A. a) Simulated temperature distribution ($^{\circ}$ C) upon completion of the peak withstand current test ($t = 0.3$ s) according to the IEC-62271-1:2007 standard. a) Simulated temperature distribution ($^{\circ}$ C) upon completion of the short-time withstand current test.....	104
Figure 5.8. a) Tested loop. b) Test circuit to perform the short-time withstand current test and peak withstand current test.	105
Figure 5.9. Temperature evolution during the peak withstand current test until reaching the equilibrium temperature. Bottom part of the J33SPK coupler substation connector (connector's body) and AAC conductor. Experimental versus 3D-FEM simulation results.	105

Figure 5.10. Temperature evolution during the short-time withstand current test until reaching thermal equilibrium. Bottom part of J33SPK coupler substation connector (connector's body) and AAC conductor. Experimental versus 3D-FEM simulation results.	106
Figure 5.11. Test voltage and current measured during the short-circuit test.	107
Figure 5.12. Model B. a) Simulated temperature distribution (°C) upon completion of the short-circuit test (t = 2.275 s) according to the IEC-61238-1:2003 standard. Conductors and YAT450AM20C bimetallic compression connector. b)) Simulated temperature distribution (°C) of the YAT450AM20C bimetallic compression connector at equilibrium temperature (t = 450 s).....	107
Figure 5.13. a) Experimental setup. Tested loop composed of an AA-8030 AL conductor and class-A YAT450AM20C terminals. b) Bimetallic YAT450AM20C terminals. Thermocouples are placed at the barrel's surface. c) Test circuit to perform the short-circuit test.	108
Figure 5.14. Temperature evolution during the short-circuit test according to the IEC 61238-1 standard and until reaching thermal equilibrium. Experimental versus 3D-FEM simulation results.	109
Figure 5.15. a) Model I. Mesh of the analyzed S210ZTLS high-capacity substation connector. b) Model II used to validate the simulation system proposed in this paper. Mesh of the analyzed ICAUL185 low-voltage bimetallic terminal connector.	110
Figure 5.16. a) 2-D plot of the analyzed substation T-connector (Model I). b) 2-D plot of the analyzed bimetallic connector (Model II).	113
Figure 5.17. Experimental test setup. a) Test loop composed of an ACSS conductor, a T-connector S210ZTLS and two terminal connectors S210ZA4P23LS. b) T-connector S210ZTLS. The five thermocouples placed in the different parts of the connector.	114
Figure 5.18. Model I. Evolution of the convective coefficients h a) with temperature and b) with time.....	114
Figure 5.19. Model I. Three-dimensional plot of the simulated temperature distribution (°C) under steady-state conditions (t = 9000 s) when circulating a total current of 986 Arms. a) Conductors and T-connector. b) T-connector. c) Temperature rise test according to.....	115
Figure 5.20. a) Experimental setup. Tested loop composed of an AAC conductor and twelve bimetallic connectors ICAUL185. b) Bimetallic connector ICAUL185. Thermocouples are placed at the barrel's surface.....	117
Figure 5.21. Model I. Evolution of the convective coefficients h a) with temperature and b) with time.....	117
Figure 5.22. Model II. Three-dimensional plot of the simulated temperature distribution (°C) under steady-state conditions (t = 3000 s) when circulating a current of 517 Arms. a) Conductors and bimetallic connector. b) Bimetallic connector. c) Thermal cycling test according to ANSI C119.4. Bimetallic connector n ^o 4 (barrel). Experimental versus FEM simulation results when circulating a current of 517 Arms.	118
Figure 6.1. Experimental setup for Peak Withstand Current and Short-Time Withstand Current Tests	120
Figure 6.2. Peak withstand current test. Temperature evolution for HTLS conductors and high capacity substation connectors (mean values).	121
Figure 6.3. Short-time withstand current test. Temperature evolution for HTLS conductors and high capacity substation connectors (mean values).	121
Figure 6.4. Experimental setup of the proposed temperature rise test performed to validate high-capacity substation connectors. The terminals placed at both the extremities of testing loop are making the connection with the power transformer and are not object of the test.	123
Figure 6.5. Ultimate tensile strength and Yield Strength as function of temperature for standard A356.0 Aluminum alloy.	125
Figure 6.6. Round conductor forming a circular loop.	138
Figure 6.7. a) Total inductance obtained from the analytical formula (6.1) and FEM simulations of a circular loop of round conductor. a = 5 mm, R = 20 mm. b) External and internal partial-self inductances.	139
Figure 6.8. Experimental loop used to measure the conductor's inductance.	140

Figure 6.9. Optimization of short-circuit test. Testing loop setup..... 143
Figure 6.10. Reference scheme to measure the resistance of the T-connector and the ACSS Lark Conductor. 144

List of tables

Table 2.1. Main testing standards for substation connectors.	25
Table 3.1. Eutectic reaction and evolution of the microstructure for a hypo-eutectic alloy.....	36
Table 3.2. Composition of A356.0 alloy.	38
Table 3.3. Microstructure of un-modified and Sr-modified A356.0 alloy with different magnifications.....	44
Table 3.4. Dimensions of the test specimen used in the mechanical tensile tests.....	47
Table 3.5. Results of mechanical tests performed on samples of un-modified A356.0 alloy with different heat treatments.	48
Table 3.6. Results of mechanical tests performed on samples of A356.0-Sr modified alloy with different heat treatments.	49
Table 3.7. Specimens used for the measurement of the electrical resistivity and the resistivity coefficient.	51
Table 3.8. Average resistivity of the standard A356.0 and A356.0-Sr0.03 modified at 20°C.	52
Table 3.9. Average thermal conductivity of the standard A356.0 and A356.0-Sr0.03 modified at 25°C.	60
Table 4.1. Installation procedures applied to substation connectors.	62
Table 4.2. Measured values of contact resistance a total connector's resistance.....	63
Table 4.3. Installation procedures applied to analyzed connectors.	66
Table 4.4. Current values settled during the temperature rise test.	67
Table 4.5. Temperature rise test. Steady state temperatures of analyzed connectors, at the third current step.	68
Table 4.6. Heat cycle test. Steady state temperatures of analyzed connectors. cycle No. 15.	69
Table 4.7. Heat cycle test. Resistance measurements of analyzed connectors before and after thermal cycles.	70
Table 4.8. Parameters for short-time withstand current tests.....	71
Table 4.9. Aluminum properties.....	82
Table 4.10. Substation connectors' parameters.....	85
Table 4.11. Surface roughness measurements.....	86
Table 4.12. Parameters used in the GA-fractal model.	86
Table 4.13. ECR Results. Comparison Between Measured and Predicted Values Of The ECR From The Different Models Analyzed.	87
Table 5.1. Dimensionless numbers related with convective phenomena description.	90
Table 5.2. Final conductor temperature in steady state condition, calculated by applying the different analyzed correlations.	95
Table 5.3. Analyzed connectors.....	101
Table 5.4. Electric and magnetic parameters considered in the model.....	101
Table 5.5. Thermal Parameters Considered In the model.....	102
Table 5.6. Emissivity Values Considered In the Model.....	103
Table 5.7. Prescribed and achieved Parameters For Peak Withstand Current And Short-Time Withstand Current Tests.	103
Table 5.8. Maximum temperature reached during the test for model a. Experimental versus simulation results. ...	106
Table 5.9. Values Achieved During The Short-Circuit Test Conducted According To The IEC-61238-1:2003 Standard.	107
Table 5.10. Maximum temperature reached during the test for Model B. Experimental versus FEM simulation results.	108
Table 5.11. Main Electric and Magnetic Parameters.....	111
Table 5.12. Main Thermal Parameters.	111

<i>Table 5.13. Emissivity values used in 3D-FEM simulation.</i>	112
<i>Table 5.14. Summary of the main characteristics of the analyzed connectors.</i>	113
<i>Table 5.15. Steady state temperature for Model I. Experimental versus FEM simulation results.</i>	116
<i>Table 5.16. Steady state temperature for model ii. Experimental versus fem simulation results.</i>	118
<i>Table 6.1. Prescribed and achieved Parameters for Peak Withstand Current and Short-Time Withstand Current Tests</i>	119
<i>Table 6.2. Measured resistance of each connector before and after the short-time and peak withstand current test.</i>	122
<i>Table 6.3. Main characteristics of the HTLS conductor used to perform the test.</i>	123
<i>Table 6.4. Three current level settled to perform the temperature rise test.</i>	124
<i>Table 6.5. Test results and evaluation of the condition of the high-capacity substation connectors after the test.</i>	124
<i>Table 6.6. Experimental and estimated values of loop inductance.</i>	141
<i>Table 6.7. Optimization of short-circuit test. Main Electric and Magnetic Parameters used in FEM simulations.</i>	143

1. Introduction

In the last years there has been a considerable increase in electricity consumption, particularly in developing countries. Forecasts indicate that this trend will continue in the coming years. According to the International Energy Agency (IEA), in the next years there will be an increase in world energy consumption and a very important part of the generation (around 50%) will come from renewable energy sources. It is also estimated that in 10 years electricity consumption from renewable sources will increase about 25% in many European countries [1]. This increase in power consumption has caused the risk of line saturation in some areas and the consequent need to increase power lines capacity. However, it is often extremely difficult to build new distribution and transmission lines, especially in urban areas or in regions of ecological interest [2].

Considering the high cost of installing new power lines, the difficulty in planning new tower sites and the related environmental impacts, social concerns, and the time involved in building new lines, a solution that some countries have chosen due to its technological and economic feasibility, is the replacement of conventional conductors with others operating at high temperature, known as **HTLS conductors** (High- Temperature Low-Sag). These conductors, with a similar section than the conventional ones, allow increasing the nominal current capacity, with a consequent increase in operating temperature. HTLS conductors can operate continuously (in steady-state conditions) at temperatures from 150 to 250° C, and allow, in many cases, doubling the capacity of existing lines [3].

The definition of an electric connector, according to the ANSI/NEMA CC 1-2009 standard [4] is “a device that joins two or more conductors for the purpose of providing a continuous electrical path”. Therefore, substation electrical connectors, the joints that physically connect power transmission lines with substation conductors and busbars, play a critical role in the efficiency and reliability of transmission systems and power distribution. It is recognized that a failure in a single connector can cause the failure of the entire line. For this reason electrical connectors can be regarded among the weaker elements in electric transmission lines [5] and therefore their reliability must be ensured.

Although cables manufacturers have developed a new methodology design to increase the capacity of the lines, manufacturers of components involved in power transmission and distribution, such as substation connectors, have not developed yet devices compatibles with this technology. Currently, in the market there are not available substation connectors compatible with HTLS systems. The new families of high-capacity substation connectors compatible with HTLS technology have to be designed to withstand, under rated operating conditions, temperatures higher than the traditional application, to prevent failures that could have serious consequences on the power transmission and distribution systems.

Therefore, the proposed project has a high degree of innovation, having the objective to develop a new product with very high technology requirements, ensuring a proper electrical, thermal and mechanical behavior under severe operating conditions introduced by HTLS technology.

The first aspect to be analyzed to accomplish the requirements of high-capacity substation connectors is the **selection of the base material**. At present, substation connectors are manufactured by using A356 cast aluminum alloy due to its good castability and physical properties. This aluminum alloy is rarely used in the as-cast condition, because it exhibits relatively poor mechanical properties due to the presence of eutectic silicon in the form of coarse acicular plates [6], which act as internal stress raisers when a mechanical load is applied. As a consequence, the A356 alloy in as-cast conditions cannot be used in high-voltage applications and it has to be exposed to heat or chemical treatments.

Heat treatments, very common processes in foundry, are used to obtain higher mechanical properties. The most common heat treatment for A356 alloy is the T6, which consists of a solution heat treatment, water quenching and artificial aging [7]. T6 dissolves precipitates (Mg_2Si) in the Al matrix, homogenizes the casting and spheroidizes the eutectic silicon. Currently, it is a common practice to expose substation connectors to T6 heat treatment before installation.

On the other hand, **chemical treatment** is not currently used in manufacturing connectors even though it can improve both electrical and mechanical properties, compared to the un-modified alloy. The chemical treatment, also known as modification, consists in the addition of small quantities of a modifier element to the melt. It allows changing the morphology of the eutectic silicon phase from flake-like to fine fibrous [8], which results in an improvement of the mechanical and electrical properties of the alloy [9]. The main physical properties of the traditional and the improved material will be characterized in order to ensure the reliability of the high-capacity substation connectors. Electrical resistivity, which is the main parameter, which affects the operating temperature of the connector, will be evaluated in a wide range of temperatures, from cryogenic up to 200 °C.

Moreover, to design the new family of substation connectors it is necessary to take into account the **contact resistance**. It is an accepted fact that the electrical contact resistance greatly influences the thermal behavior of substation connectors and other electrical equipment. Therefore, during the design stage of such electrical devices it is essential to accurately predict the contact resistance to achieve an optimal thermal behavior, thus ensuring contact stability and extended service life.

If contact resistance is low and stable in time, a good electrical connection and a long life of substation connector is guaranteed; whereas, if it is high and unstable, it could cause overheating of the connector and, consequently, a reduced operating life [10]. Connector's long term performance is directly related to the contact points established during installation [11]. The restriction of current flow to these few contact points, also known as "a-spots," constitutes a first contribution to the total contact resistance; this component is usually called constriction resistance [12].

Moreover, it is necessary to take into account the effect on contact interface of a thin oxide film layer. It is well known that aluminum and its alloys reacts quickly with atmospheric oxygen, and a passivation layer of few nanometers of aluminum oxide, usually known as alumina, grows on atmospheric exposed aluminum surfaces [13]. Since aluminum oxide is very insulating, electrical current can transfer across the alumina layer only thanks to tunneling and frittting mechanisms [14]. As a consequence, the film resistance is the second component of the total contact resistance of a joint. However, a good electrical contact between two conductors can be established only if the contact spots can be created due to the mechanical rupture of the oxide insulating film [14].

Contact surface preparation is essential to guarantee proper contact between connector and conductor since the contact resistance can notably degrade substation connectors' performance. The most common installation procedures found in technical literature for aluminum-to-aluminum and aluminum-to-copper connections and their performances under thermal cycling are analyzed and compared [12], [15]–[18]. Most of these works have shown that the mechanical abrasion reached by brushing surfaces, and lubrication through contact aid compound application is the most efficient method to ensure an adequate contact resistance in aluminum-to-aluminum connections [14]. However, many studies demonstrated that if HTLS cables will replace traditional conductors, the installed population of connectors will age more rapidly and the number of connector failures will increase due to the increased aging effects of higher temperature and current density. Therefore, also the installation procedure needs to be improved, with the aim to improve the thermal behavior of high-capacity substation connectors. In this thesis a surface treatment for high-capacity substation connectors, which consists on a chemical cleaning before conventional installation will be proposed to improve their performance. The thermal behavior of connectors installed with the new installation procedure will be compared with the traditional one. To this end, temperature rise, thermal cycle and short-time withstand current tests will be performed with connectors installed with both traditional and new installation procedure.

To predict the thermal behavior of high-capacity substation connectors in operating conditions imposed by HTLS conductors, it is important to be able to **estimate the electrical constriction resistance**.

First of all different ECR models available in the technical bibliography have been analyzed and compared find out the most suitable model for substation connectors. It will be shown that the model that shows the better agreement with experimental data is The Kogut and Komvopoulos fractal model for conductive rough surfaces, which assumes fractal geometry, elastic-plastic asperities and size-dependent micro-contacts ECR to estimate ECR. However, fractal-based models are based on several variables whose values need to be tuned for each particular application, since they depend on the nature of the contacting surface and specifically the surface roughness. A genetic algorithm (GA) approach to determine the optimal values of the parameters in the fractal model to accurately fit the measured surface roughness with that predicted by the fractal model will be proposed in this thesis.

This thesis will be also dedicated to the implementation of the **electromagnetic-thermal multiphysics model** developed to simulate the thermal behavior of high capacity substation connector. Joule power losses calculated in the electromagnetic analysis are the heat source used as input data of the thermal analysis, which allows predicting the temperature evolution and distribution in the considered domain.

This model will be used to implement a FEM-based simulation tool to predict the result of **short-time and peak withstand current tests** and **temperature rise test** in substation connectors.

It is well-known that short-circuits generate thermal and electromechanical stresses [19], [20], so power systems are designed and tested to ensure that electrical and mechanical devices involved can withstand short-circuit conditions. To this end such devices are tested and certified in accordance with the short-time withstand current and peak withstand current tests, as defined by different international standards [21]–[23].

Temperature rise test allows determining the substation connector's thermal behavior under both transient and steady state conditions and thus evaluating if its size and design is compatible with the electromagnetic-thermal stress at which it is subjected during normal operational conditions. According to the ANSI/NEMA CC1-2009, the temperature rise must be performed at 100%, 125%, and 150% of the rated current.

Thermal stress generated by short-circuit and temperature rise currents may increase the contact resistance, thus affecting contact stability [24] and therefore the expected service life, due to the increase of the electrical resistance and associated power losses.

Therefore, to ensure reliable operation, connectors should not suffer from excessive overheating [25], thus their suitable thermal behavior must be ensured.

Due to the huge current requirements in terms of instantaneous power of these demanding short-circuit tests [26], they must be carried out in very specific and expensive laboratory facilities. On the other hand, temperature rise tests usually last a long time, are very power-consuming and therefore are very expensive. Therefore the development of a realistic simulation tool is essential for anticipating the results of the mandatory laboratory tests in a fast inexpensive way.

In this thesis an advanced 3D-FEM modelling tools to perform realistic simulations to determine the thermal stresses at which substation connectors are subjected during short-time withstand current and peak withstand current and temperature rise tests will be developed.

By using this modelling tools to assist the connectors' design and optimization process, an optimized design can be achieved, thus satisfying the electromagnetic and thermal requirements imposed by the international standards [22], [27] and ensuring to pass the compulsory laboratory tests imposed by the standards. The simulation tools will be validated through experimental test.

Finally, the test and validation of the high-capacity substation connectors will be described. Short-time and peak withstand current and temperature rise tests according to international standards will be performed with the aim to validate the new design, material and installation procedure of the new product.

In annex A the problem of the loop inductance will be introduced. A critical problem that arises when performing short-circuit tests to large loops involving substation connectors is the inductive component of the loop impedance. Transformers used to perform short-circuit tests usually have a secondary winding with very few turns, producing a low output voltage. The reactive component of the impedance, which is related to loop size, limits the current output capacity, because it tends to saturate the output of the transformer since it consumes large amounts of reactive power. The inductance of the most typical testing loop configuration (round nonmagnetic conductor forming circular loop) under alternating current supply will be analyzed, since it significantly determines voltage drop in the loop, thus increasing reactive power consumption, limiting conductor's ampacity and the current output capacity of the power transformers used to perform the tests. In addition an initial estimation of the loop inductance is required to determine the voltage set-point during the short-time current withstand and peak withstand current tests. Finally, a simple method to minimize the power requirements when conducting short-circuit tests, based on the reduction of reactive power consumption will be proposed.

1.1 Objectives

This work aims to contribute to the development of a new family of high-capacity substation connectors compatible with HTLS technology.

The main objectives of this work are listed as follows:

1. Concept phase

This phase consists in defining the requirements of the new aluminum alloy for high-capacity substation connectors and selecting and testing the new alloy.

1.1 Definition of high-capacity substation connector's requirements.

1.2 Study, selection and optimization of the suitable materials for manufacturing high-capacity substation connectors.

1.3 Electrical, mechanical and thermal characterization of the conventional aluminum alloy used for substation connectors and the optimized alloy for high-capacity substation connectors.

1.4 Analysis of the electrical contact resistance in substation connectors. Improvement of the installation procedure for high-capacity substation connectors.

2. Objectives of the prototyping phase.

This phase consists in defining the main design parameters for this application as well as to develop a multi-physics FEM model to assist the design process of the connectors and ensuring appropriate electrical and thermal behavior.

2.1 Identification of the key design parameters to develop a new family of high-capacity substation connectors

2.2 Developing multi-physics software tools for modeling and simulating the electromagnetic and thermal behavior of the connector.

2.3 Design optimization of high-capacity substation connectors with the aid of multi-physics simulations of temperature rise and short-circuit tests.

3. Objectives of the testing phase.

This phase consists in adapting the standard temperature rise and the short-circuit laboratory tests for high-capacity substation connectors operating at high temperature, as well as to test the new products.

3.1 Short-time and peak withstand current test for high capacity substation connectors.

3.2 Temperature test for high capacity substation connectors.

1.2 Main Contributions

1. Settling the requirements of the material for high capacity substation connectors.

2. Analysis and optimization of the alloy to manufacture substation connectors. Settling of the requirements for heat and chemical treatments for the alloy. Characterization of the microstructure of conventional and optimized alloy.
3. Characterization of the mail electrical, mechanical and thermal properties of the conventional and optimized alloy to manufacture substation connectors.
4. Analysis of the electrical contact resistance in substation connectors. Improvement of the installation procedure through a chemical cleaning with the aim to reduce contact resistance. Characterization of the thermal behavior of substation connectors installed with the proposed installation procedure and comparison with traditional connectors.
5. Analysis of different available models of electrical constriction resistance in technical bibliography. Development of the GA-optimized fractal model to predict the electrical constriction resistance in substation connectors. Experimental validation through resistance measurements.
6. Development of electromagnetic-thermal Multiphysics models to simulate the thermal behavior of substation connectors. Development of 3D-Finite Element tool to simulate the result of the short-time and peak withstand current tests in substation connectors. Development of 3D-Finite Element tool to simulate the result of the temperature rise tests in Substation Connectors. Validation of the simulation tools with experimental data.
7. Test and validation of high-capacity substation connectors through standardized short-time and peak withstand current test and temperature rise test.
8. Introduction to the problem of the inductance of the testing loop. Analysis of formulas to estimate inductance of round conductor forming a circular loop.
9. Optimization of short circuit test. Analysis of a simple setup to minimize the power requirements when conducting short-circuits tests for substation connectors. Validation through experimental test.

1.3 Thesis Publications

Publications in international conferences and journals have been carried out during the development of this research and are listed as follows:

1.3.1 Conferences:

- 1 Capelli, F., Riba, J.-R., Gonzalez, D.: 'Optimization of short-circuit tests based on finite element analysis', in '2015 IEEE International Conference on Industrial Technology (ICIT)' (IEEE, 2015), pp. 1368–1374.
- 2 Capelli, F., Riba, J.-R., Rodriguez, A., Lalaouna, S.: 'Research Towards Energy-Efficient Substation Connectors', in (Springer International Publishing, 2017), pp. 295–301.
- 3 Capelli, F., Riba, J.-R., Gonzalez, D.: 'Thermal behavior of energy-efficient substation connectors', in '2016 10th International Conference on Compatibility, Power Electronics and Power Engineering (CPE-POWERENG)' (IEEE, 2016), pp. 104–109.

- 4 Capelli, F., Abomailek, C., Riba, J.-R., Sanllehi, J.: 'Analysis of electrical contact resistance models for substation connectors', in '2016 IEEE International Conference on Power System Technology (POWERCON)' (IEEE, 2016), pp. 1–6.
- 5 F. Giacometto, F. Capelli, E. Sala, J.-R, Riba, L. Romeral, Temperature Rise Estimation of Substation Connectors Using Data-Driven Models Case: Thermal conveccion response, 41st Annual Conference of the IEEE Industrial Electronics Society IECON 2015, Yokohama (Japan), 9-12 Nov. 2015.
- 6 C. Abomailek, F. Capelli, J.-R. Riba, P. Casals-Torrens, M. Moreno-Eguilaz, Transient Thermal Modelling of Short-Circuit Test for Conductors by Means of Dimensional Reduction, International Conference on Power Systems Technology (Powercon 2016), Wollongong, Australia, 28 Sept.- 1 Oct. 2016.

1.3.2 Journals:

- 1 Francesca Capelli, Jordi-Roger Riba, Joan Pérez, Three-Dimensional Finite-Element Analysis of the Short-Time and Peak Withstand Current Tests in Substation Connectors, *Energies*, 9, 418, May 2016, DOI: 10.3390/en9060418
- 2 Francesca Capelli, Jordi-Roger Riba, Analysis of formulas to calculate the AC inductance of different nonmagnetic conductors' configurations, *Electrical Engineering*, pp. 1-11, Published Online 16 October 2016, DOI 10.1007/s00202-016-0455-5.
- 3 Francesca Capelli, Jordi-Roger Riba, Josep Sanllehi, Finite Element Analysis to Predict Temperature Rise Tests in High-Capacity Substation Connectors, *IET Generation, Transmission & Distribution*, Minor revision 08/12/2016.
- 4 Francesca Capelli, Jordi-Roger Riba, Elisa Rupérez, Josep Sanllehi, A GA-Optimized Fractal Model to Predict the Constriction Resistance of Substation Connectors, *IEEE Trans. Instrumentation and Measurement*, Under revision
- 5 Francisco Giacometto, Francesca Capelli, Luis Romeral, Jordi-Roger Riba, Enric Sala, Thermal Response Estimation in Substation Connectors Using Data-Driven Models, *Advances in Electrical and Computer Engineering (AECE)*, vol.16, no.3, pp.25-30, 2016, doi:10.4316/AECE.2016.03004
- 6 Carlos Abomailek, Francesca Capelli, Jordi-Roger Riba, Pau Casals-Torrens, Transient Thermal Modelling of Substation Connectors by Means of Dimensionality Reduction, *Applied Thermal Engineering* (2017), pp. 562-572, DOI: 10.1016/j.applthermaleng.2016.09.110

2 State of the art

In this chapter the state of the art about substation connectors and the main testing standards to evaluate their performance will be presented. Moreover a digression about HTLS conductors, their properties, materials and technology will be shown with the aim to introduce the framework in which this thesis has been developed.

3.1 Substation Connectors

Electrical substations are localized in the proximity of a production plant, at the point of delivery to the end user and the points of interconnection between the lines since they constitute the nodes of electricity transmission grid.

Depending on their characteristics, size and function, substations can be divided into four categories [5]:

- Switchyard at generating station. It connects the generators to the utility grid and provides off-site power to the plant.
- Customer substation. This one functions as the main source of electric power supply for one particular customer.
- Switching substation. It involves the transfer of bulk power across the network. Typically it is the end point for transmission line originated by generating switchyard and it provisions the electrical power for circuits that feed distribution stations. It does not have transformers and operates only at a single voltage level.
- Distribution Substation. It supplies the distribution circuits that directly furnish the electric customers.



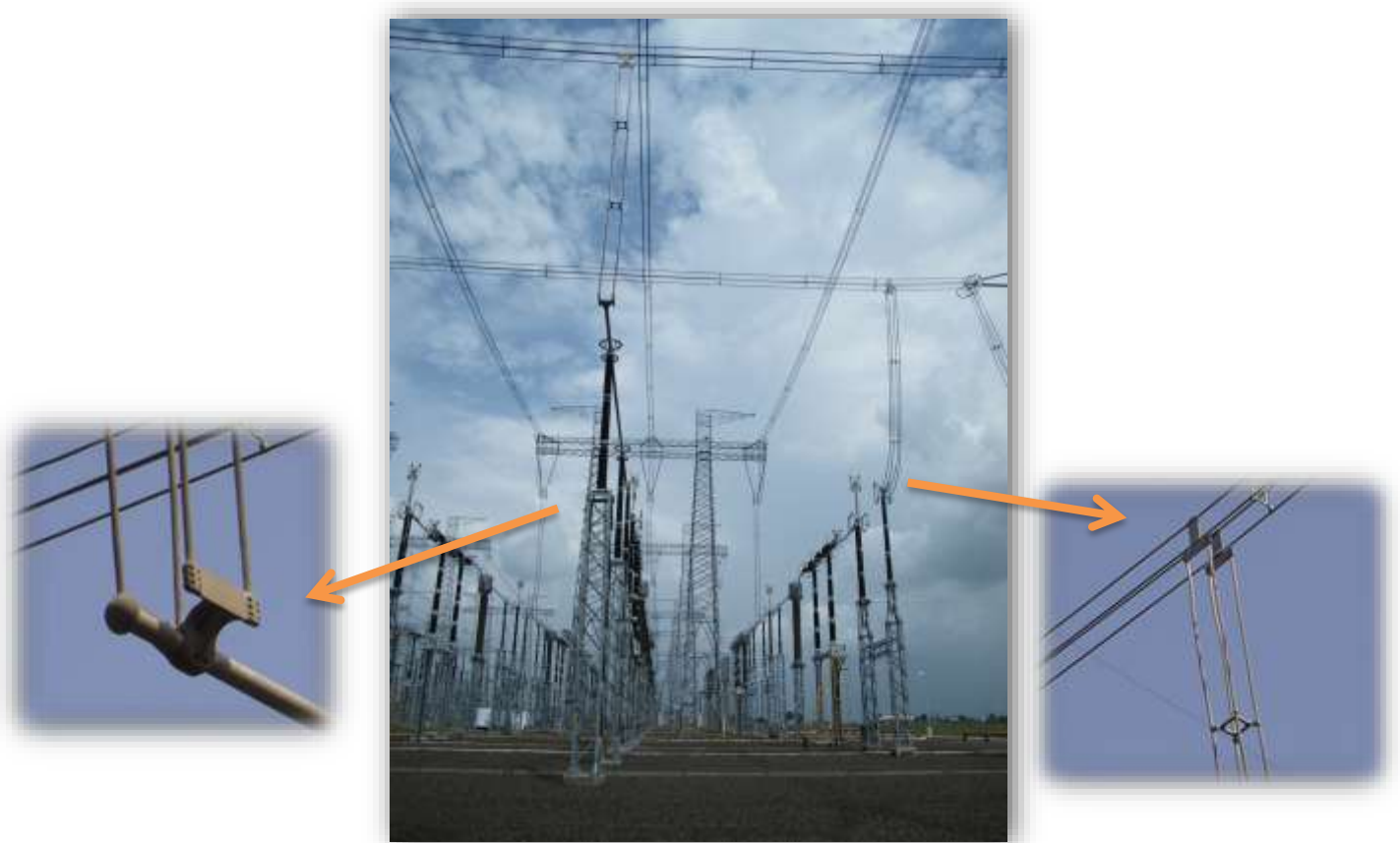
Figure 2.1. Electrical substation

Substations employ various devices for safety, switching, voltage regulation and measurement. Busbars are the main current carrying conductors within a substation. Busbars are made of copper or aluminum, and are supplied in many configurations, including rectangular bars, round tubing, square tubing, stranded cables, etc.

Substation connectors are the joints that physically link the power transmission line and the substation conductors and busbars [7].

They are usually divided into different categories, depending on the physical junction between the connector and the conductor: mechanical, welded, and compression type are the most common ones. The challenge for substation connector design is to meet dimensional, mechanical and electrical constraints. Mechanical connectors are often used for substation connections due to their adaptability to sizing [6].

Substation connectors, which will be considered in this thesis, are, therefore, aluminum alloy devices of mechanical type, where coupling parts, that is the parts which transmit electrical power, are mechanically joined by applying a specific torque by means of bolts and nuts, with the aim to maintain



the connection integrity and ensure an adequate contact resistance between connector and conductor.

Figure 2.2. Substation connectors and their position in an electrical substation.

Mechanical type substation connectors have a wide range of geometries and sizes.

Fig. 2.2 shows two types of substation connectors belonging to SBI Connectors Spain catalogue.

Advantages that make mechanical type widely used in transmission systems include:

- Achieve desired resilience. This helps to reduce the stress due to thermal expansion which tends to cause excessive creep.
- Simple installation and usage. They permit to disassemble the components without damage, enabling their re-use.

Disadvantages of mechanical connections include:

- Specific torques must be applied to provide proper clamping force. Installers rarely apply calibrated torques. Hence, tightening torques applied on identical installations are usually not repeatable.
- Mechanical connections in areas of high vibration may require more maintenance and periodic inspection.
- If insulated connection is required, their geometries make it difficult an appropriate coverage.

Being the high-capacity connector constrained by definition to the HTLS conductors' technology, in this study will be considered the substation connectors that joins two or more HTLS cables, such as the T-connectors shown in Fig. 2.

3.1 Testing standard for substation connectors

International standards must be considered in order to evaluate substation connectors' performance. The ANSI/NEMA CC1 standard [7] provides standard test methods and performance requirements to evaluate the electrical and mechanical characteristics of substation connectors under normal operating conditions.

Current standard tests are performed at room temperature. However, it is well known that HTLS cables operate at much higher temperatures and therefore possibly the associated connectors. For high-capacity substation connectors, the standard framework does not exist yet because it raises complex technical challenges that must be addressed in the near future.

Although, from the design point of view, substation connectors are subjected to a large amount of variables, this thesis will be focused in those particular parameters that affect their performance when connectors are used coupled with HTLS cables. Therefore, with the aim to develop a methodology to design high-capacity substation connectors, this work is mainly focused on **temperature rise**, **thermal cycle** and **short-circuit** tests. Table 2.1 summarizes testing standards considered in this thesis.

Table 2.1. Main testing standards for substation connectors.

Name	Description	Test	Year	Ref.
ANSI NEMA CC1	Electrical power connections for substations	Temperature rise test	2009	[4]
ANSI C119.4	Connectors for use between aluminum to aluminum and aluminum to copper conductors designed for normal operation at or below 93 degree C and copper to copper conductors designed for normal operation at or below 100 degree C.	Thermal cycle test	2011	[28]
IEC 62271-1	High-voltage switchgear and controlgear - Part 1: Common specifications	Peak withstand current and short-time withstand current test	2007	[29]
IEC 61238-1¹	Compression and mechanical connectors for power cables for rated voltages up to 30 kV (Um = 36 kV) - Part 1: Test methods and requirements	Short-circuit test	2003	[30]

¹ Referred to compression and mechanical connectors for power cables for rated voltages up to 30 kV.

In the following sub-sections test methods summarized in Table 2.1 are presented, with the aim to understand the international standard requirements for substation connectors.

2..1 Temperature rise test

The temperature-rise test method is described in the ANSI NEMA CC1- 2009 standard [4], which is the main standard reference for substation connectors.

The temperature rise test is useful to determine the substation connector's thermal behavior under both transient and steady state condition and thus evaluate if its size and design is compatible with the electromagnetic-thermal stress, at which it is subjected. The standard explains that, at the discretion of the manufacturers, the temperature rise test on electric power connectors may be conducted either indoors or outdoors.

The temperature rise shall be determined at 100, 125, and 150% of the rated current, with equilibrium temperatures obtained at each level. The standard describes equilibrium temperature as a constant temperature (+/-2°C) between three successive measurements taken five minutes apart. Measurements are made at the end of the first 30 minutes and at one-hour intervals thereafter until completion of the test.

The rated current shall be in accordance with tabulated values that established this value as function of conductor size.

In order to eliminate heat sinks or hot spots on the test loop, conductors of the correct size and type may have a length from each opening of the connector to the point where the connection is made to the circuit of at least 8 times the conductor diameter (but not less than 1.2 m).

Moreover, it has to be taken into account that various types of connectors require to be tested in accordance with the following specifications:

- Terminal connectors: The current shall be either the current rating of the equipment to which the connector is connected, or the current rating of the conductor for which the opening is designed, whichever is lower.
- Angle and straight connectors: The values of current shall be selected as a function of the conductor that has the lower current-carrying value where the openings are of two sizes, and on the basis of the conductor that is common to both openings where the openings are of the same size.
- "T" connectors: The test current shall be based on the conductor having the lowest current rating in the assembly.

ANSI NEMA CC1 requires that the temperature rise of the tested electric power connector does not exceed the temperature rise of the conductor with which it is intended to be used. The temperature rise of an electric power connector, which connects conductors of different sizes, shall not exceed the temperature rise of the conductor having the highest temperature rise.

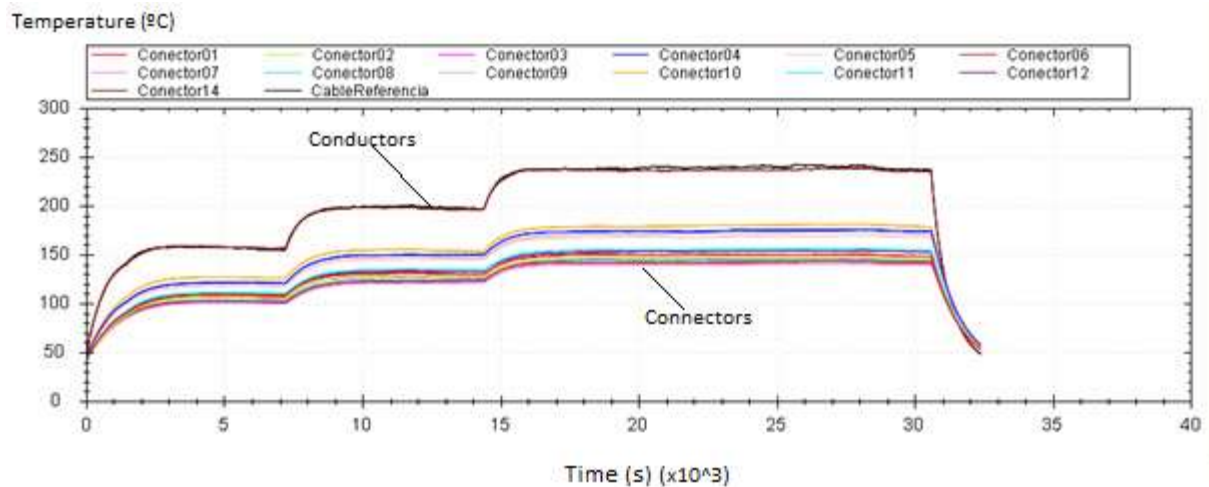


Figure 2.3. Results of temperature rise test performed at 100%, 125% and 150% of n % of nominal current established for conductor.

2.2 Thermal cycle test

Connector's thermal behavior can also be evaluated by means of the standard current cycle test regulated by the ANSI C119.4-2011 standard [28]. The current cycle test is a very important tool to evaluate the aging process of connectors. Thermal cycles result in thermal expansion and contraction of the electrical contact interface, which contributes to degrading the contact points [14]. The test current

must be adjusted to result in a steady-state temperature rise on the control conductor between 100°C and 105°C above ambient temperature. Temperature measurements of the connectors, conductors, and ambient air have to be made at the end of the specified heating cycle, immediately before the current is turned off, whereas resistance measurements have to be made at the end of the heating cycle period, with all connectors thermally stabilized at the room temperature.

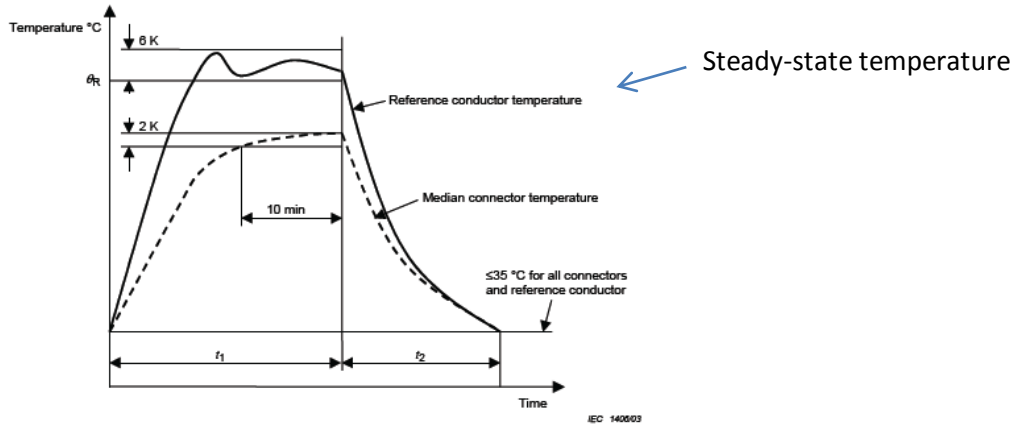


Figure 2.4. General graph of an heat cycle provided by the IEC 61238-1 standard.

The resistance of the tested connection shall be stable. Stability is achieved if any resistance measurement, including allowance for measurement error, does not vary by more than $\pm 5\%$ from the average of all the measurements at specified intervals during the course of the test. Moreover, the temperature of the tested connector shall not exceed the temperature of the control conductor.

2.3 Peak withstand current and short-time withstand current test

According to IEC 62271-1:2007 [29] standard the rated short-time withstand current, often denoted as I_k , is the root-mean-square (RMS) value of the current that the analyzed electrical device can withstand under specified conditions during a prescribed period of time, while the rated peak withstand current, denoted as I_p , is defined as the peak value of the first major loop (Fig. 2.5) of the rated short-time withstand current which the electrical device under analysis can withstand under specified conditions. For a frequency of 50 Hz, the rated peak withstand current is equal to 2.5 times the rated short-time withstand current. The standard duration of short circuit is 1 s. If necessary, a value lower or higher than 1 s may be chosen (most used values are 0.5 s, 2 s and 3 s).

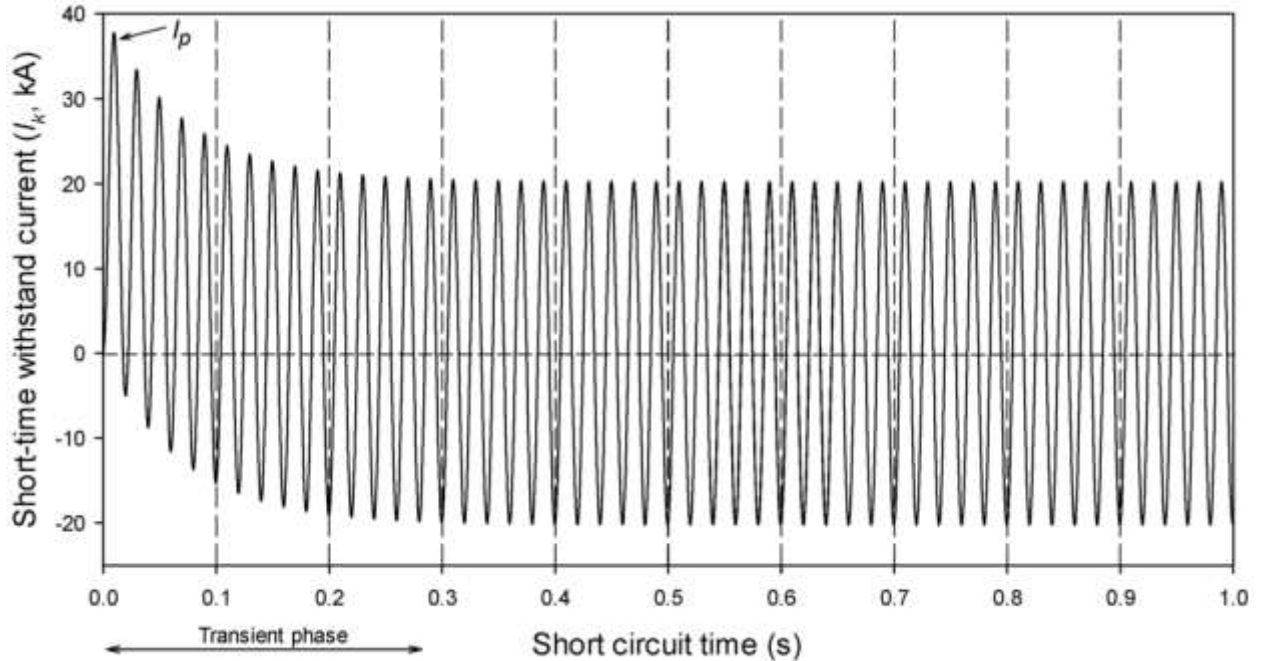


Figure 2.5. Short-time withstand current (I_k) and peak withstand current (I_p).

To verify that the connector has not suffered significant damage due to the peak and short-time withstand current tests, it has to accomplish a main requirement: the connector must not have suffered visible damages. Moreover, the resistance of the connectors shall be measured; if the resistance has increased by more than 20 %, and if it is not possible to confirm the condition of the contacts by visual inspection, an additional temperature-rise test should be performed.

2.4 Short-circuit test

According to the IEC 61238-1:2003 Standard [30] which regulates the short-circuit tests for low- and medium-voltage connectors, the short-circuit current must raise the temperature of the reference conductors from an initial value of 35 °C up to 250–270 °C. The duration of the short-circuit current shall be in the range [0.9, 1.05] s when applying a maximum current of 25 kA. If the required short-circuit current exceeds this value, a longer duration up to 5 s with a current level between 25 kA and 45 kA can be applied to reach temperatures of 250–270 °C.

2.5 Other tests

Although other tests will be treated briefly, it is necessary to clarify those improvements on high current, and thus high temperature performances will not worsen the connector behavior when performing other tests. The mandatory tests required for substation connectors [4] to ensure their performance once installed in high voltage transmission systems are listed as follows.

- **Pullout strength test:** in this test the connector is fastened to the conductor by means of bolts at a recommended torque. Then, a tensile load is applied to the conductors. As a result, the pulling velocity must not exceed 20.8 mm·min⁻¹ per meter length.

- **Corona and radio interference voltage test:** this is maybe the most complex test since it consists on determining the voltage at which corona appears. This test requires a high voltage generator to energize the test samples at these voltage levels. It also requires a shielded room protected against external EMI sources. Although, tests are usually performed under dry atmospheric condition, also there exist standard procedures to perform wet and artificial pollution tests.
- **Torque strength test:** in this test the conductors shall be assembled in the connector and the bolts tightened uniformly and alternately at 113 N·m and being tightly incremented until a 50% over the nominal torque value is achieved without fracture.

3.1 HTLS Technology

With the growth in electrical power demand, problems associated to the increasing electric power demand and minimal constructions of new power lines are ensured.

This problem has led to find for other realistic and feasible solutions to solve this saturation problem. Different possibilities have been proposed in the last years. However, the solution which appears more feasible from a technological, economic and social point of view is based on increasing the capacity of existing lines by replacing conventional conductors with new conductors that either have lower electrical resistance and/or are capable to operate at higher temperature within the existing line limits of sag and tension [31]. Many methods of increasing thermal rating have been presented, some of which are described below:

- Increasing the ampacity of an existing line using a replacement conductor larger than the original one (having lower resistance). The main negative effect is the increase of both ice and wind loads and tension loads on existing structures. A larger conventional conductor, thus, requires the reinforcement of suspension structures.
- Increasing the ampacity of an existing line by using a replacement conductor with nearly the same diameter as the original conductor but capable of operation at higher temperature (within existing sag clearance and loss-of-strength constraints). This second solution does not suffer the problems of the first one and avoids the need for reinforcement of suspension structures. These conductors are known as High-Temperature Low-Sag (HTLS) conductors; HTLS conductors can operate continuously at temperatures as high as 200°-250° C, allowing in many cases almost doubling the capacity of existing lines [3].

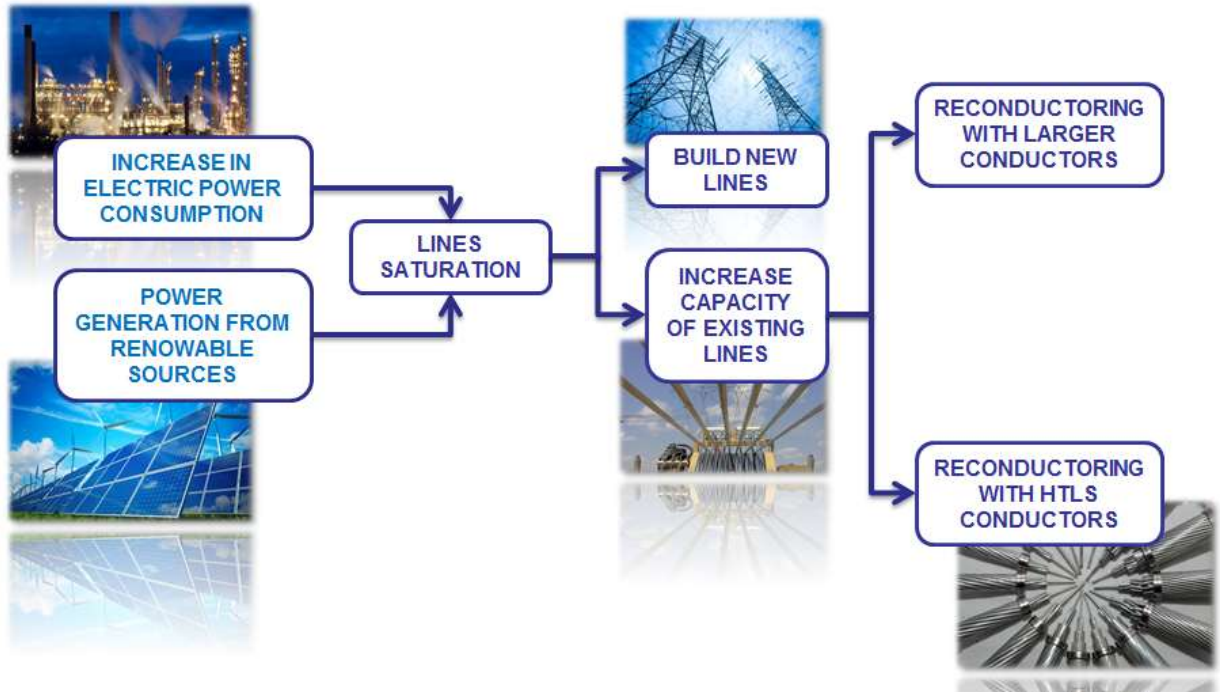


Figure 2.6. Method for increasing current line capacity.


Therefore, the main advantage of HTLS conductors is an increased line ampacity with minimal changes in the mechanical structure of the existing line.

2.1 Materials and properties

HTLS conductors are constructed with a combination of aluminum (or aluminum alloy) wires, which provide conductivity, and core wires to offer mechanical strength. The main constituent materials used in HTLS conductors are diverse: some cores are common steel strands coated with zinc, zinc alloy, or aluminum. Other conductors utilize new materials like fiber reinforced aluminum composites or fiber reinforced polymer composites [32]

There are several basic categories of HTLS transmission conductors as shown in Table 2.2. It is worth noting that each conductor is a combination of structural core material and conductive material [31].

Table 2.2. Basic categories of HTLS transmission conductors.

Acronym	Name		External wires	Core wires
ACSS	Aluminum Conductor. Steel Supported		Aluminum	Steel

ACSS - TW	Trapezoidal shaped strands, Aluminum Conductor. Steel Supported		Aluminum (Trapezoidal shaped)	Steel
G(Z)TACSR	Gap Type (Ultra) Thermal Resistant Aluminum Alloy Conductor, Steel Reinforced		Aluminum Alloy	Steel
T(K)(Z)ACSR	Thermal (High Strength) (Ultra) Resistant Aluminum Alloy Conductor, Steel Reinforced		Aluminum Alloy	Steel
X(Z)TACIR	Extra (Ultra) Thermal Resistant Aluminum Alloy Conductor, Invar Reinforced		Aluminum Alloy	Invar
ACCR	Aluminum Conductor, Composite Reinforced		Aluminum	Composite
ACCC	Aluminum Conductor, Composite Core		Aluminum	Composite

The thermal rating of alloy aluminum conductor steel reinforced (ACSR) based lines is limited by the maximum sag or by the annealing of aluminum strands. The standard thermal limit of Al-alloys is about 90°C - 100°C. The thermal limit is established in this range of temperature because any further heating can anneal the conductor.

To avoid annealing three techniques are possible:

- Anneal intentionally the aluminum used to produce conductors before installation; factory annealed aluminum uses the acronym ACSS.
- Provide an alloy that is immune to annealing at high temperature.
- Alloy the aluminum with zirconium. This is done in varying degrees to produce TAL, ZTAL/UTAL and XTACIR designated alloys.

The improved performance of HTLS conductors therefore originates lower thermal expansion coefficients and enhanced behavior of tensile strength with temperature. There is a great variation of commercially available HTLS conductors; several types can be considered depending on the core and conducting material [33], [34].

- ACSS (Aluminum Conductor Steel Supported): Fully annealed aluminum strands over a conventional steel stranded core.
- GTACSR (Gapped TAL Alloy Aluminum Conductor Steel Reinforced): High-temperature aluminum alloy strands (TAL) separated by an oil-filled gap from a conventional steel stranded core.
- (Z)TACIR (Zirconium Alloy Aluminum Conductor Invar Steel Reinforced): High-temperature aluminum alloy strands (TAL, ZTAL, KTAL and XTAL) over a low-thermal elongation steel alloy (INVAR).
- ACCR (Aluminum Conductor Composite Reinforced): ZTAL wires over a low-thermal elongation metal matrix composite core.
- ACCC (Aluminum Conductor Composite Core): Fully annealed aluminum strands over a low-thermal elongation polymer matrix composite core.

Only the XTAL version reaches thermal limits as high as the annealed standard alloy. This kind of alloy also modestly increases the aluminum's resistance whereas annealing reduces it. These alloyed conductors are combined with standard or special steel core materials and have the same weight to diameter ratios as ACSR counterparts and almost the same sag-temperature relationship. The sags are large at high temperatures because the thermal expansion characteristics are basically unchanged from the standard ACSR values [31].

The material properties and phenomena that control transmission line design are [32]:

- **Tensile strength, density and elongation to failure** are the main properties that can affect line design tension and sag.
- **Elastic modulus of core materials** affects the line sag. A high value of this property causes a minimal sag change; conversely, low value of elastic modulus can cause large sags under conditions of heavy mechanical load. Heavy ice and wind represents high mechanical loads.
- **Coefficient of thermal expansion.** Thermal elongation is defined by the coefficient of thermal expansion (CTE). For HTLS conductors, since aluminum has a larger CTE than the core, the CTE of the core affects the maximum sag of the conductor. At high temperature operation the aluminum transfers its mechanical load to the core, so the core has to withstand most of the mechanical load.
- **Electrical conductivity** concerns to the outer aluminum material, which provides the majority of the electrical conduction.
- **Fatigue resistance** is affected by aeolian vibration (low amplitude, high frequency process; occurs in a range of 10-100 million cycles) and galloping (high amplitude, low frequency process; it occurs in a range of 10-100 thousand cycles). It does not represent a problem for steel and

composite cores. Fretting the aluminum layers at support locations typically causes fatigue failures in conventional conductors.

- **Creep** is a time dependent permanent elongation of the conductor under a sustained mechanical load. Aluminum and Al-alloys can suffer this problem (they exhibit a higher creep rate). Conversely, steel and fiber reinforced composite core have very low levels of creep.
- **Corrosion resistance**, steel cores need a corrosion protection like zinc (galvanized) coatings, aluminum cladding, or zinc- 5% aluminum-mischmetal coatings. Aluminum has good corrosion resistance in almost all environments; but aluminum corrosion can occur in particular environments like oxygen deficient cells, in salt polluted environment. Corrosion in metal matrix composites can occur in the interfacial boundary between fiber and matrix. Furthermore, it is necessary to evaluate the formation of galvanic coupling between the core and the outer aluminum strands.
- **Environmental aging of polymer constituents** (moisture, heat, UV) can decrease tensile and flexural strength, or can induce changes in glass transition temperature “ T_g .”
- **Brittle fracture** is a stress-corrosion phenomenon and can occur in glass reinforced polymer and carbon polymer systems. The brittle fracture occurs with stress in water or an acidic environment (acid rain or acids generated from the interaction of electrical corona and humid air).
- **Resistance to sustained high temperature** (core) and **heat resistance**: all the materials that compose the conductor (core, outer aluminum, grease) have to resist high temperature exposure without appreciable changes in fundamental properties. Steel cores are limited by coating breakdown to either 200-250°C (galvanized) or 250-300°C (aluminum-clad and “zinc-5% aluminum-mischmetal alloy coated steel wire) due to reaction and breakdown of the protection layers.
- **Glass transition temperature of polymer composites** (T_g) is the knee point of the curve in which the polymer matrix begins to soften. In the proximity of T_g the capacity of the matrix to transfer loads between the load-bearing fibers decreases.
- **Flexural strength of polymer composites**: the flexural strength of metals and metal matrix composites affects the tensile strength of the conductor.
- **Thermal cycling**: in fiber reinforced composite materials, due to the different CTE of different materials present, thermal cycling induces alternating stress state. It can cause de-lamination, matrix aging or cracking in polymer matrix.

3. Materials for high-capacity substation connectors

High capacity substation connectors, compatible with HTLS conductors, will be forced to work continuously at higher temperatures when compared to traditional applications. Thus, high-capacity connector's material has to resist high temperature exposure without appreciable changes in its fundamental properties. It is possible to define main requirements for high-capacity substation connector's material:

- Maximize mechanical strength (ultimate tensile strength, yield strength, elongation to failure);
- Maximize electrical conductivity;
- Maximize thermal conductivity;
- Minimize coefficient of thermal expansion;
- Minimize corrosion behavior;

To meet these requirements it is necessary to improve the materials currently used to manufacture substation connectors.

The main mechanical, thermal and electrical properties of the traditional and the improved material have to be characterized in order to ensure the reliability of the high-capacity substation connectors. Electrical resistivity, which is the main parameter affecting the operating temperature of the connector, needs to be evaluated in a wide range of temperatures, from cryogenic up to 200 °C that correspond to the maximum temperature that can be experienced from connector's material when operates with HTLS conductors.

3.1 Introduction

Aluminum and aluminum alloys are the most-used materials in high voltage applications. Aluminum is a metal of the 3rd group, with atomic number 13 and atomic weight 26.98. It is one of the most abundant elements in the Earth's crust, but it is not present in nature as metallic aluminum, but in the form of oxides (bauxite). It is one of the most widely used and inexpensive engineering materials and has a great number of applications in almost all industrial sectors [35]. Aluminum has high electrical and thermal conductivity, paramagnetic behavior, excellent resistance to oxidation and corrosion, good workability and low density; all this properties make it very attractive for manufacturing cables and substation connectors for high voltage transmission systems.

Fig. 3.1 shows the Ashby plot of different properties involved in material's selection for high voltage applications. Fig. 3.1 a) shows electrical resistivity in $\Omega \cdot m$ as function of cost ($\text{£}/m^3$), whereas in Fig. 3.1 b) strength in MPa is plotted as function of density (kg/m^3), for different materials.

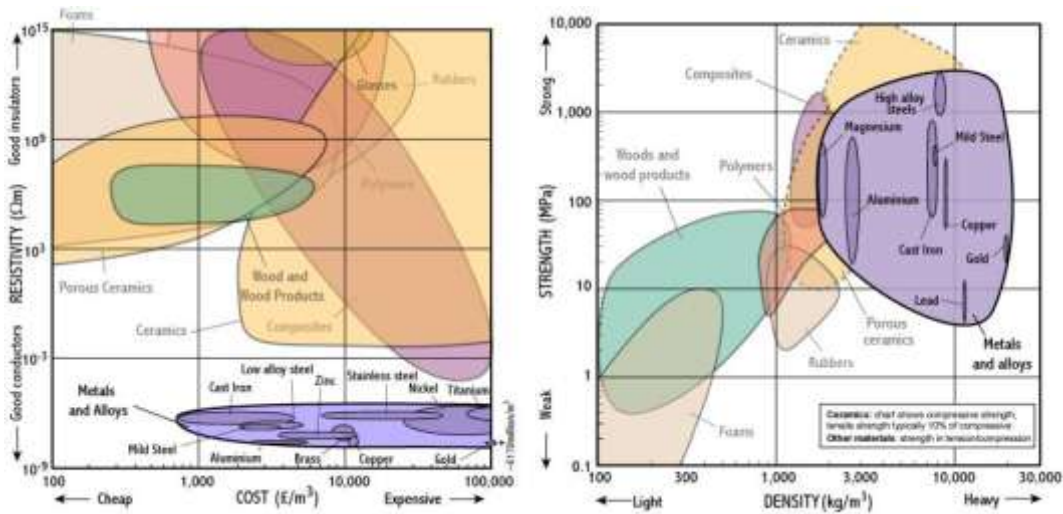


Figure 3.1. Ashby plot of different properties involved in material's selection for high voltage applications. a) Electrical resistivity vs cost and b) Strength vs density.

Since aluminum has an FCC crystal structure, it is very ductile even at very low temperatures. The main limitation of aluminum is its low melting temperature (660 °C) that restricts the maximum temperature at which it can be used. Moreover, pure aluminum has poor mechanical properties, which do not allow withstand the stresses to which connectors are subjected.

The mechanical strength of casting aluminum may be enhanced by many methods (alloying, grain size reduction, heat treatment, etc.); however, these processes decrease resistance to corrosion, and most of the electrical proprieties. Principal alloying elements are copper, magnesium, silicon, manganese, and zinc [36].

Currently substations connectors are usually manufactured by sand casting. The process, characterized by using sand as the mold material is widely used in industrial application since it is relatively cheap.

The main objective of the next sections (3.2 and 3.3) is to present the state of the art about:

- Microstructure of Al-Mg-Si alloys and its relation with main physical properties;
- Optimizing alloys' microstructure;

3.2 Microstructure of Al-Mg-Si alloys

Due to the combination between excellent castability and good physical properties, aluminum-silicon alloys are the most commonly used in most industry sectors and provide about 90% of all the casting manufactured [35]. They contain enough silicon to cause the eutectic reaction. Silicon confers low melting point and fluidity. As shown in Al-Si phase diagram (Fig. 3.2) the Al-Si binary system forms a simple eutectic at the temperature of 577°C and at composition of 12.6% Si. The maximum solubility of silicon in aluminum is 1.5 % at the eutectic temperature, and the solubility of silicon increases with temperature to 0.016% Si at 1190°C [37].

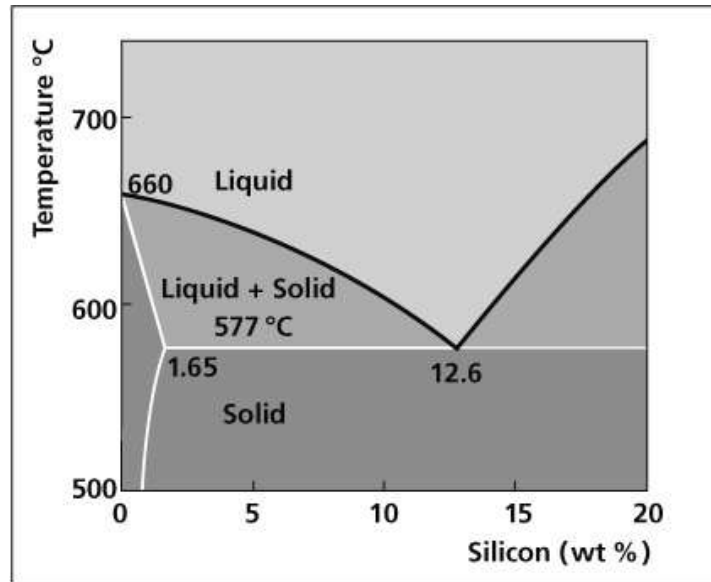
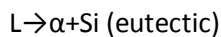


Figure 3.2. Al-Si phase diagram.

There is only one invariant reaction in the phase diagram, the eutectic reaction:



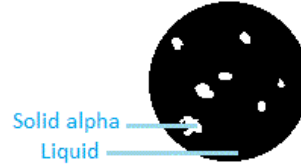
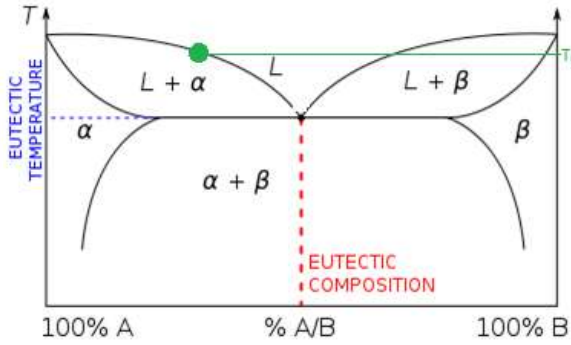
The eutectic reaction takes place at 577 °C and at a silicon percentage of 12.6%. The Al–Si eutectic can form as follows, in function of the Si concentration [37]:

- Directly from the liquid in the case of a silicon concentration of 12.6% (**eutectic Al–Si alloy**);
- In the presence of primary aluminum in the case of silicon contents <12.6% (**hypoeutectic Al–Si alloys**);
- In the presence of primary silicon crystals in the case of silicon contents >12.6% (**hypereutectic Al–Si alloys**).

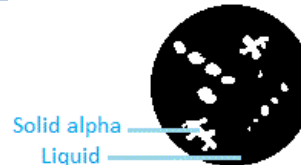
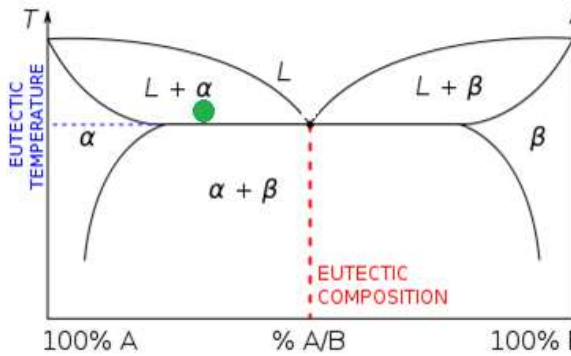
The following table explains how the eutectic reaction takes place and the evolution of the microstructure, with reference to the phase diagram for a hypo-eutectic alloy, as the A356.0, currently used to produce substation connectors.

Table 3.1. Eutectic reaction and evolution of the microstructure for a hypo-eutectic alloy.

Phase Diagram	Microstructure
	<p>Mixture of Al and Si with a composition at the left of the eutectic point. The alloy is fully liquid.</p>

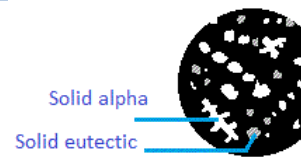
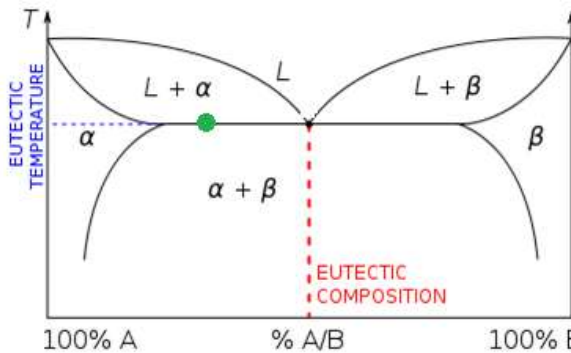


The mixture is slow cooled until it reaches temperature T_L (liquid line). At this temperature α -Aluminum phase starts to solidify as dendrites at any favorable nucleation sites. Dendrites grow to become grains of α .



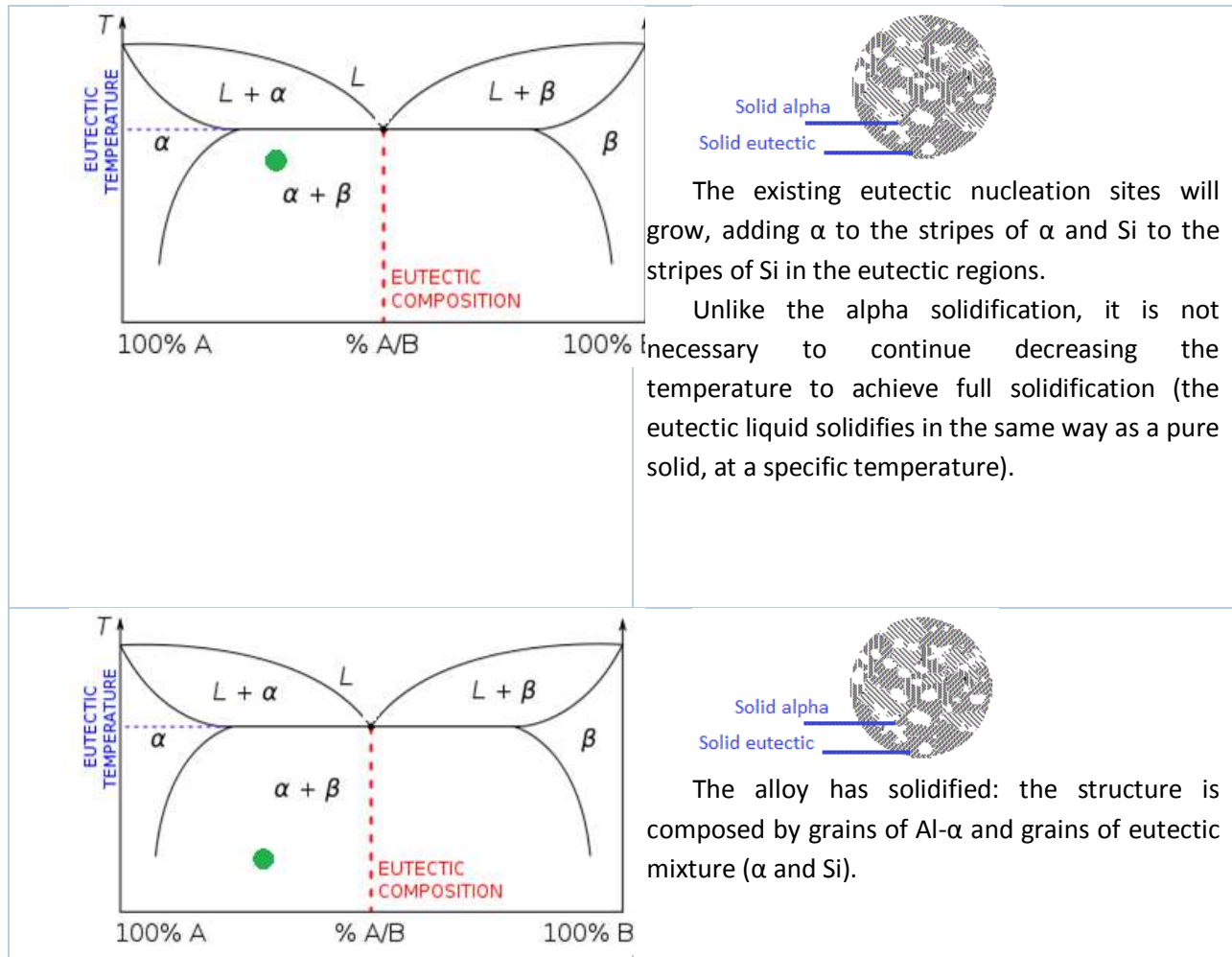
The alloy continues to cool. Nucleating and growing regions of solid alloy form grains and grain boundaries.

The remaining liquid becomes richer in Si. The composition of the solid alpha also becomes richer in Si.



Solidification of α phase continues until enough Al has been removed; liquid is of eutectic composition.

This composition is obtained at eutectic temperature, where α stops forming as a discrete solid and the remaining liquid starts to solidify into the lamellar eutectic composition of α and Si. Solid eutectic forms.



Generally, hypoeutectic and near-eutectic Al-Si alloys are used when good castability and corrosion resistance are required. Moreover, in this class of alloys, the addition of Mg provides age-hardening, through Mg-Si precipitates, and improves mechanical properties of the material [35].

Currently, hypo-eutectic cast **A356** alloy, also known as Al-Mg0.3-Si7 alloy, whose composition is shown in Table 3.2, is the most used alloy of the entire class, and, also, it can be considered the common used material to produce substation connectors.

Table 3.2. Composition of A356.0 alloy.

Element	Percentage
Aluminum, Al	91.1 - 93.3 %
Copper, Cu	≤ 0.20 %
Iron, Fe	≤ 0.20 %
Magnesium, Mg	0.25 - 0.45 %
Manganese, Mn	≤ 0.10 %
Other, each	≤ 0.05 %

Other, total	<= 0.15 %
Silicon, Si	6.5 - 7.5 %
Titanium, Ti	<= 0.20 %
Zinc, Zn	<= 0.10 %

Microstructure and physical properties of alloys are strongly related.

The main parameters that control physical properties of A356 are:

- Grain size and morphology;
- Primary (DAS) and secondary dendrite arm spacing (SDAS);
- Shape and distribution of eutectic silicon particles;
- Secondary phases;
- Porosity.

The quality of the microstructure of alloys depends on chemical composition, melting process, casting process and solidification rate [38]–[40]. The effects of these variables on microstructure are reported in the technical literature [41]–[43].

Solidification in hypo-eutectics alloys, as A356, begins with the development of a primary aluminum dendrite network. It is well known that fine dendritic microstructures in castings, characterized by low dendrite arm spacing, have higher mechanical properties, particularly if the tensile strength and ductility are considered.

The secondary dendrite arm spacing (SDAS), which controls the size and the distribution of porosity and intermetallic particles, depends on chemical composition of the alloy, cooling rate, local solidification time and temperature gradient. If it is desired that porosity and second phase constituents result finely dispersed, SDAS have to be as smaller as possible. Analytical and empirical models correlating the main solidification parameters and the secondary dendrite arm spacing have been studied by many authors [44], [45].

The morphology of the silicon phase can be rod-like (fine-fibrous) or flake-like depending on many factors. Day and Hellawell [6] identified the different forms of silicon in Al-Si eutectic as a function of the temperature gradient, growth rate and alloy composition. The silicon rod particle diameter, silicon spacing and silicon rod length describe the morphology of the silicon phase.

The solidification rate determines the coarseness of the microstructure including the fraction, size and distribution of intermetallic phases. Fig. 3.3 [46] shows the variation of microstructure with cooling rate for a hypo-eutectic alloy. Sand casting is the most common process to produce substation connectors and presents the lowest cooling rate among the three processes (sand cast, permanent mold cast and die cast). The dendrite cells in sand cast are larger, the silicon flakes (shown in dark) are coarser. Moreover, the defect size such as pore size is also controlled by the solidification rate.

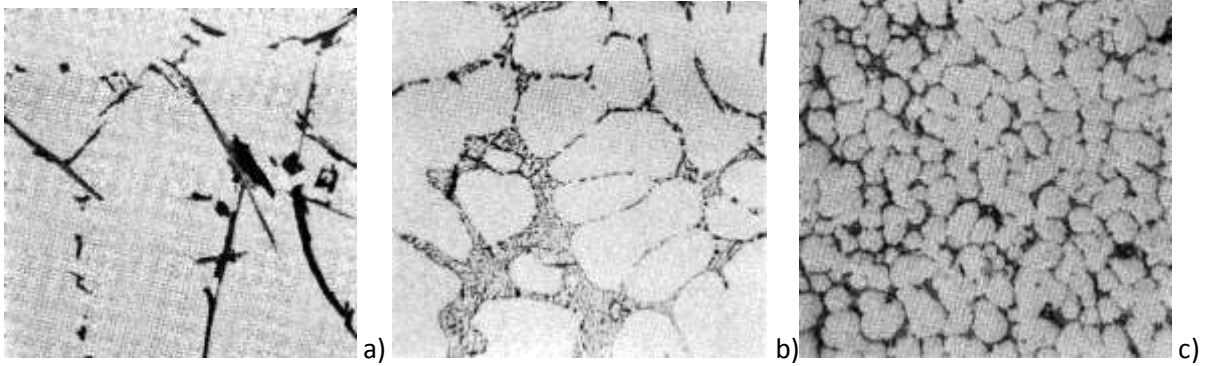


Figure 3.3. Microstructure obtained with different solidification rate. a) Sand cast. b) Permanent mold cast and c) die cast. (from [46]).

In aluminum casting alloy a small equiaxed grain structure improves not only the resistance to hot cracking and mass feeding, but also enhances main mechanical properties of alloy [35]. The most evident effects of reduction in grain size are the more uniform distribution of gas porosity and eutectic structure. Grain refinement is affected by alloy composition, cooling rate, temperature gradient in the melt and, as explained above, casting method. When a casting method characterized by slow cooling is used (e.g. sand casting) grain refinement can be achieved by blocking the columnar growth using mechanical or electromagnetic forces to detach dendrite arms, or by adding additives (nucleants), that provide more nuclei (nucleants provide a surface for growth at the liquid temperature of alloy).

A356 alloy is rarely used in the as-cast condition, because it exhibits relatively poor mechanical properties due to the presence of eutectic silicon in the form of coarse acicular plates which act as internal stress raisers when a mechanical load. As consequence of poor mechanical properties, A356 alloy in as-cast conditions cannot be used in high-voltage applications.

The two main processes used to improve the properties of this alloy are [47]:

- Heat treatment
- Chemical treatment

The heat treatment, a very common process in foundry, is used to obtain desired mechanical properties (in terms of tensile strength, ductility and hardness) although it also can affect the electrical properties. Heat treatment dissolves precipitates (Mg_2Si) in the Al matrix, homogenizes the casting and spheroidizes the eutectic silicon.

The chemical treatment, also known as modification, consists in the addition of small quantities of modifier element to the melt. It results in a change of the morphology of the eutectic silicon phase from flake-like to fine fibrous, which results in an improvement of the mechanical and electrical properties.

3.3 Heat treatments

In order to improve the low mechanical properties of the A356 alloy in as-cast conditions, in industrial practice, substations connectors are usually subjected to a heat treatment before being installed. The most common heat treatments for A356 alloy are T4 and T6.

T4 heat treatment consists of solution heat treatment, water quenching and natural aging at room temperature to a substantially stable condition, whereas T6 heat treatment consists of a solution heat treatment, water quenching and artificial aging.

Heat treatments, also known as precipitation hardening, are based on the precipitation of small dispersed particles of Mg_2Si within the phase matrix, which permit to enhance the strength and hardness of the alloy. The presence of the precipitate particles and the strain fields in the matrix surrounding the coherent particles provide higher strength by hindering the movement of dislocations.

An alloy is heat treatable if these requirements are accomplished [36]:

- Appreciable (on the order of several percentual points) maximum solubility of one component in the other;
 - Alloying elements exhibit increasing solid solubility in aluminum as the temperature increases
- A356 alloy meets these requirements.

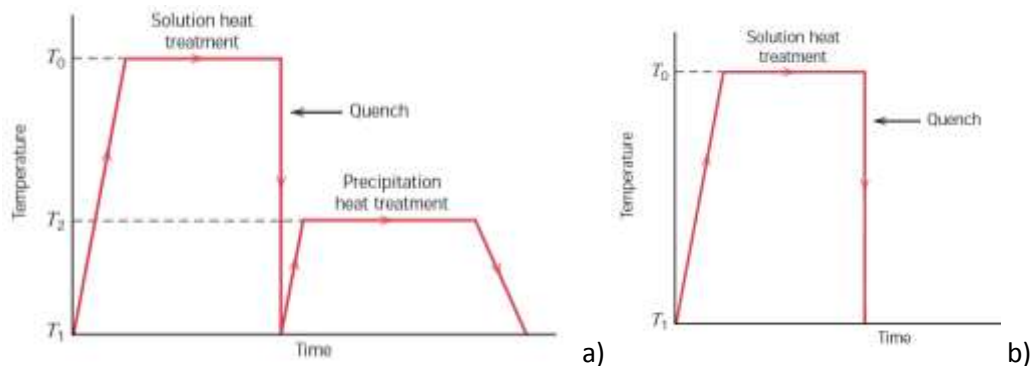


Figure 3.4. Temperature and time required for T6 (a) and T4 heat treatments (b).

In detail, T6 heat treatment consists of [16]:

- 1) **Solution heat treatment:** Formation of a single-phase solid solution by dissolution of all solute atoms. It consists of heating the alloy to a temperature within the α phase field (T_0) and waiting until all the β phase is completely dissolved.

Solution heat treatment allows obtaining:

- dissolution of the hardening elements (Mg and Si) into α -Al,
- homogenization of the casting
- spheroidization and coarsening of the eutectic silicon.

In the metallurgical literature, for A356 alloy, for both T4 and T6, it is reported as reference temperature for this treatment 540°C for 12 h [35]; however, many authors [48], [49] have suggested both lower temperatures (500°C) and higher temperatures (up to 560°C) with different treatment times.

- 2) **Quenching** to temperature T_1 (room temperature). Thanks to the rapid cooling, diffusions and the accompanying formation of any of the β phase are prevented.

- 3) **Precipitation hardening:** The supersaturated α -Al solid solution is heated to temperature T_2 within the region $\alpha+\beta$, at which temperature diffusion rate is appreciable. The β precipitate phase begins to form (like finely dispersed particles).

In the metallurgical literature, for A356 alloy, it is reported as reference temperature for this treatment 155°C for 3-5 h [35]. After the appropriate aging time at T_2 , the alloy is cooled to room temperature.

In T4 heat treatment the first two steps (**solution heat treatment** and **quenching**) are the same described for T6 treatment, whereas precipitation hardening is substituted by **natural aging**, this process occurs spontaneously at room temperature until the metal reaches a stable condition.

The purpose of T4 and T6 treatments is to precipitate out of solution the hardening particles (Mg_2Si) that were dissolved during the solution heat treatment. The precipitation sequence has been proposed by many authors; Dutta and Allen [35] proposed the precipitation sequence in this alloy system as:



Figure 3.5. Precipitation sequence for A356.0 alloy proposed by Dutta and Allen [35].

Where SSSS is the super-saturated solid solution of alpha-phase and solute clusters are clusters of Mg and Si atoms. GP is the Guiner Preston zone; precipitation usually starts from the formation of GP zones, which can be considered as fully coherent metastable precipitates. The following evolution of the microstructure involves the replacement of the GP zones with more stable phases. GP zones elongate in the [100] matrix direction and assume a needle shape. The needles grow with time and become rods and, finally, platelets (β represents Mg_2Si equilibrium precipitates).

3.4 Chemical modification

Silicon modification is a practice used to refine the eutectic structure in A356 alloy. The eutectic silicon phase in unmodified alloys is present in the form of flake-like or plate-like. Eutectic silicon modification can be defined as the transformation of eutectic silicon phase from coarse and plate-like to a fine and fibrous. Through this modification, mechanical properties improvement is guaranteed as consequence of structure refinement [50].

Modification can naturally occur at rapid solidification rates (this process is known as quench modification) but in the practice, for sand casting characterized by slow cooling rates, modification is achieved by small addition of elements of groups IA, IIA and rare earths europium, lanthanum, cerium, praseodymium and neodymium (chemical modification) [35].

In the technical literature the most accepted theory that explains the modification mechanism is the one based on growth mechanisms, proposed by Lu and Hellawell [51], which is based on the assumption that modifiers retard the growth rate of silicon. Modified action is due to impurity incorporation in

silicon structure, that contains more imperfections than unmodified silicon phases; thus, if imperfections are a potential site for branching; silicon when grows in a modified structure have to bend and twist, and it results in forming a fibrous morphology.

Fig. 3.6 (source [8]) shows the comparison between the microstructure of unmodified and modified hypo-eutectic alloy. Silicon phase is present in the form of coarse and plate-like in first one (a) and as fine and fibrous in the second one (b).

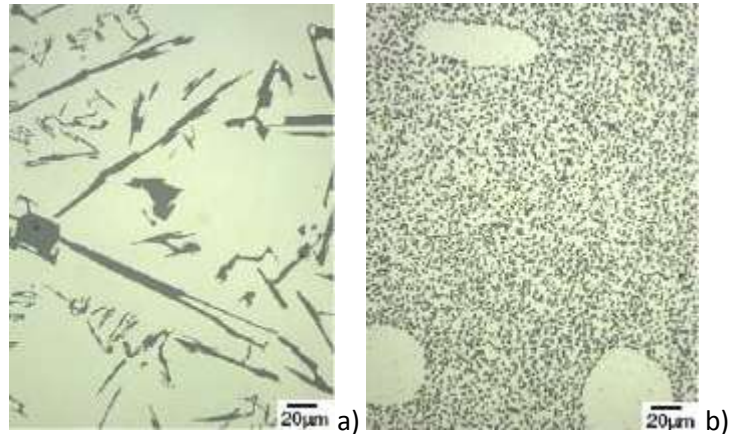


Figure 3.6. Microstructure of unmodified (a) and modified (b) hypo-eutectic alloy.

The size requirements for modifier element is [35]:

$$\frac{R_{modifier}}{R_{Si}} > 1.64$$

Where $R_{modifier}$ is the atomic radius of modifier element and R_{Si} is the atomic radius of silicon.

The most used modifier agents in industrial application are sodium and strontium, due to the strong modifying action at low concentrations.

Strontium is usually added to the melt in the form of low-strontium master alloys such as Al-10 wt% Sr in the temperature range of 670° C-720° C [35]. Other authors report optimum treatment temperatures ranging from 680°C to 750°C in A356 alloy.

It is reported in literature that is preferable the use of strontium as modifier agent, compared to sodium, due to higher recovery (>90%) and lower rate of loss [35]. However, the effect of strontium is weaker than that of sodium, especially at low cooling rates.

3.4.1 Modification of A356.0 alloy for substation connectors

Chemical treatment, as abovementioned, is not currently used to manufacture connectors even though it can improve both electrical and mechanical properties, when compared with the un-modified alloy. The chemical treatment, also known as modification, consists in the addition of small quantities of a modifier element to the melt. It results in a change of the morphology of the eutectic silicon phase from coarse acicular to fine fibrous, which results in an improvement of both electrical and mechanical properties.

With the aim to characterize the microstructure and main physical properties of the A356-modified alloy, some sample material was melted in Giga Foundry (Santpedor, Barcelona) and subsequently the T6 heat treatment was applied. Strontium was chosen as modifier agent, due to the strong modifying

action at low concentrations. It has been performed the modification with the addition of 0.03% of Strontium, that was added to the melt in the form of low-strontium master alloys (Al-10 wt% Sr) at a temperature of about 700° C.

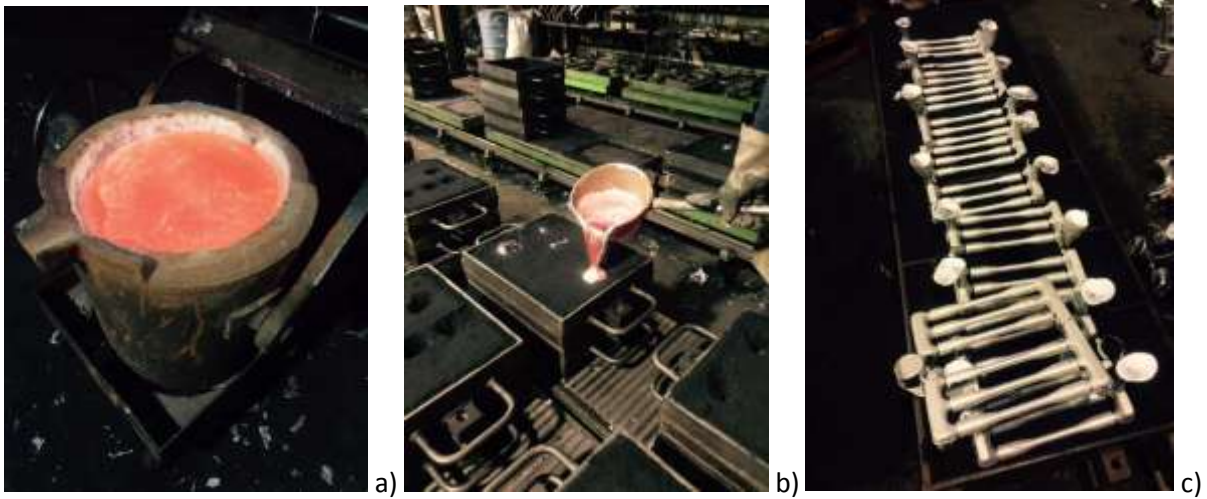


Figure 3.7. Different phases of the A356-Sr modified sample’s casting.



Figs.3.7 shows the main phase of A356-modified sample’s casting. In fig. 3.7 a) it is shown the molten metal after the degassing process; in Fig. 3.7 b) the metal is poured into the mold to fill the cavity and all the channels. The filling time is very short in order to prevent early solidification of metal. Fig. 3.7 c) shows the samples before machining and heat treatment.

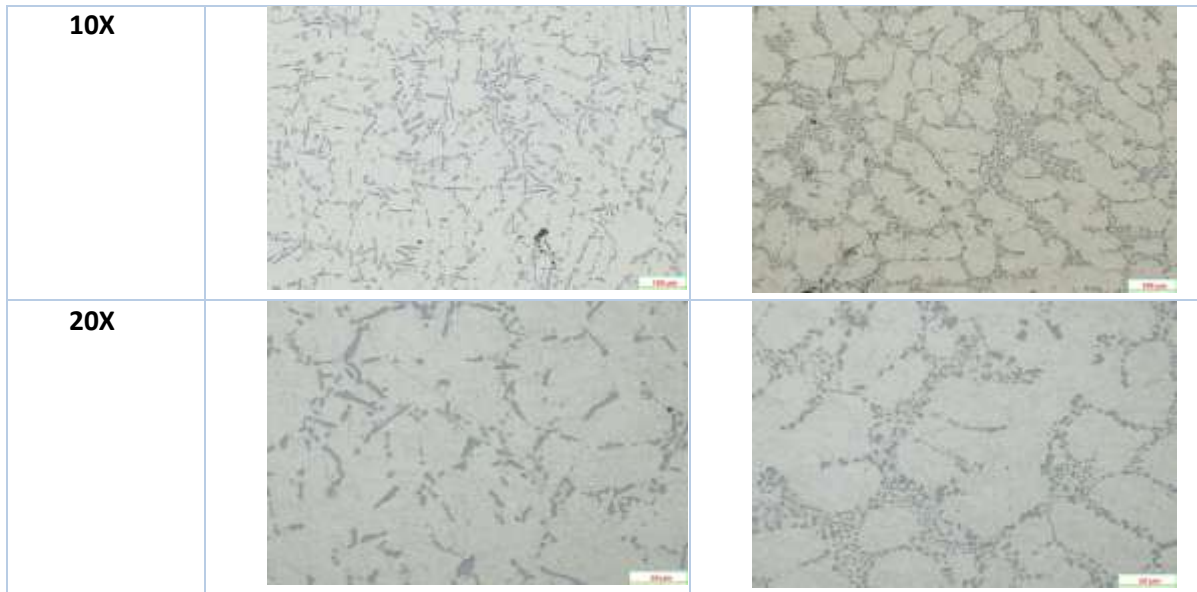
3.4.2 Microstructure of un-modified and Sr-modified A356.0 alloy

The microstructure of un-modified and Sr0.03-modified A356 alloy, has been analyzed and compared. The pictures with different magnifications have been taken by means of an optical microscope from the Department of Materials of UPC, Barcelona.

By analyzing the results presented in Table 3.3, it can be observed that the Sr-modified alloy presents a fine fibrous eutectic silicon structure (in grey), while in the un-modified alloy, the silicon is present as coarse-flakes.

Table 3.3. Microstructure of un-modified and Sr-modified A356.0 alloy with different magnifications.

Magnification	A356.0 un-modified	A356.0 Sr-modified
5X		



3.4.3 Effect of the heat treatment and the chemical modification on electrical conductivity and thermal properties of A356.0 alloy

The effect of heat treatment on electrical conductivity has been studied in the technical literature [47]. It has been shown that when applying a solution heat treatment, the electrical conductivity value is related to the changes in silicon morphology. The precipitation of Mg_2Si during artificial aging, improves the electron flow in the aluminum matrix and, therefore, electrical conductivity increases.

Many authors have studied the effect of strontium modification on electrical conductivity. It has been found that strontium modified Al-Si and Al-Si-Mg alloys exhibit a larger electrical conductivity [9], [52]. The increase in electrical conductivity is due to the differences in the eutectic silicon shape, since the electrons flow more easily through smaller eutectic regions.

3.5 Characterization of physical properties in un-modified and Sr-modified A356.0 alloy

3.5.1 Mechanical properties

A tensile test, also known as tension test, is the most fundamental type of mechanical test that can be performed to characterize the basic properties of a material. In tensile tests the sample is subjected to a controlled tension until failure. The test is simple, relatively inexpensive, and fully standardized.

The strength of interest may be measured as the stress necessary to cause appreciable plastic deformation or the maximum stress that the material can withstand. These measures of strength are used during the design stage of substation connectors. The material's ductility, which is a measure of the deformation before it fractures, is also a property of great interest in connector's design.

The tensile test process involves placing the test specimen in the testing machine and slowly extending it until it fractures. During this process, the elongation of the gauge section is recorded

against the applied force. The **engineering strain**, ϵ , is calculated from the elongation measurement by means of equation (1) [53]:

$$\epsilon = \frac{\Delta L}{L_0} = \frac{L - L_0}{L_0} \quad (3.1)$$

where L_0 is the initial gauge length in m, and L is the final length in m.

The **engineering stress**, σ , is calculated from the force measurement with the following equation [53]:

$$\sigma = \frac{F}{A_0} \quad (3.2)$$

where F is the tensile force in N and A_0 is the nominal cross-section of the specimen.

Data collected from the machine can be graphed into a stress–strain curve, shown in the Fig 3.8.

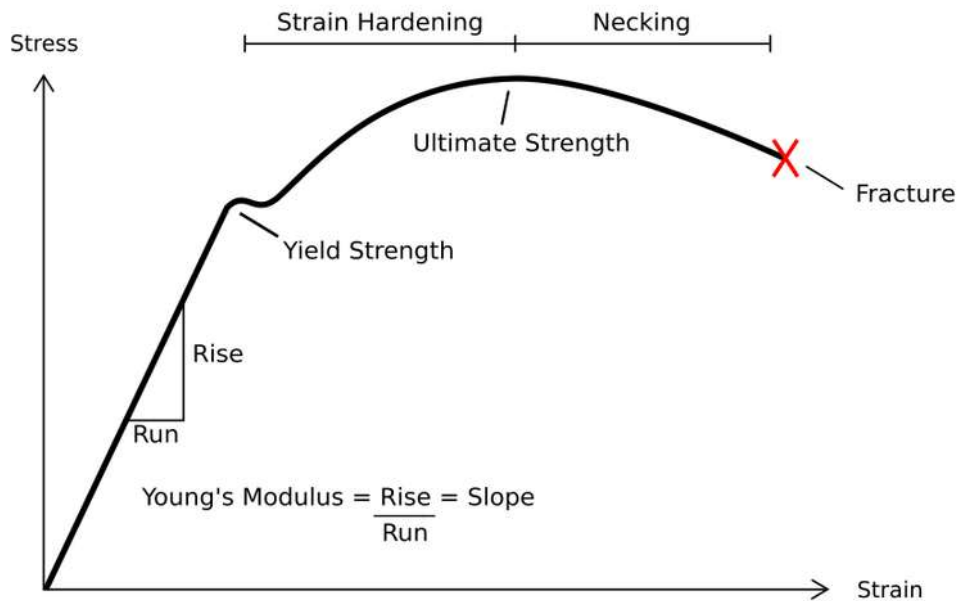


Figure 3.8. . General stress–strain curve. Engineering stress (σ) is shown as a function of engineering strain (ϵ).

The mechanical properties that have been evaluated to characterize and compare the behavior of the un-modified and Sr-modified alloys are:

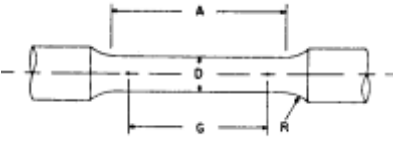
- **Ultimate Tensile Strength (UTS)**. Ultimate tensile strength is defined as the maximum stress in Mpa that a material can withstand while being stretched or pulled before breaking. The UTS is usually found by performing a tensile test and recording the engineering stress versus strain. The highest point of the stress–strain curve (see point on the engineering stress/strain diagram in Fig. 3.8) is the UTS. It has been calculated as the maximum load withstander by the specimen divided by its initial section.
- **Elongation to fracture (A%)**. It is the increase in length that has suffered the specimen before its fracture. It is measured between two points whose position is normalized and expressed as a percentage.

Both the ultimate tensile strength (UTS) and elongation to failure (A%) are intensive properties, i.e., its value depends on the size of the test specimen. However, it depends on other factors such as the preparation of the specimen, the presence of surface defects, the presence of internal pores and the temperature of the environment and material. For this reason it is necessary to consider that there is significant variability in the values obtained in the measurement of mechanical properties.

3.5.1.1 Tensile Specimens

The tensile specimen employed for experimental measurements, shown in Fig. 3.9, has enlarged ends for gripping and a circular gage section, which cross-sectional area is reduced so that deformation and failure will be localized in this region. Measurements are made in the gage length and the distances between the ends of the gage section and the shoulders should be great enough to produce the fracture in the gage length. Moreover, the gage length should be large enough compared to its diameter. Fig 3.9 shows the 2D-drawing and Table 3.4 summarizes the dimensions of the specimens used in this study.

Table 3.4. Dimensions of the test specimen used in the mechanical tensile tests

Dimension	Value (mm)	
Gauge length G	56 ± 1	
Diameter D	14 ± 0.3	
Radius of fillet R	R 74	
Length of reduced section A	80 ± 1	
Total length L	200 ± 2	

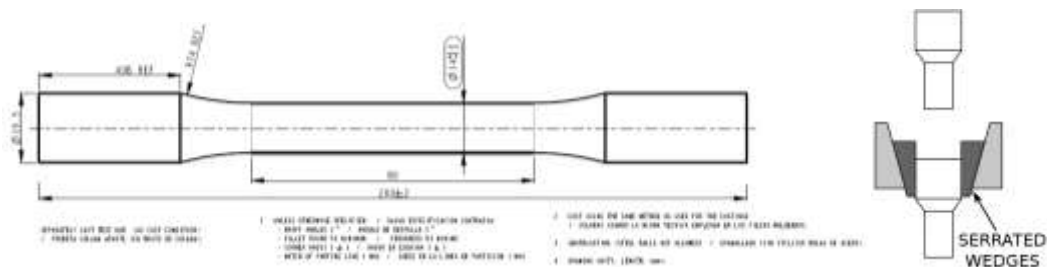


Figure 3.9. a) Drawing and dimensions of the test specimen used in the mechanical tensile tests. b) Specimen gripping system employed for the experimental test.

There are various ways of gripping the specimen. In the tests performed in this project serrated grips (shown in fig 3.9 b)) have been employed. The most important concern in the selection of a gripping method is to ensure that the specimen can be held at the maximum load without slippage or failure in the grip section.

3.5.1.2 Experimental setup

Tensile strength and **elongation to failure** are obtained by performing a tensile test with a universal vertical testing machine of 5 tons, as shown in Figure 3.10, placed in the Amber-UPC laboratory. This

type of machine has two crossheads. The first one is adjusted for the length of the specimen and the other is driven to apply tension to the test specimen.



Figure 3.10. Vertical bench of 5 tons used to perform the mechanical tensile tests.

The software integrated in the test machine measures and records in a graph the engineering stress σ against the engineering strain ϵ . The highest point of the stress-strain curve is the ultimate tensile strength (UTS). The test specimens, although belonging to the same batch and are apparently identical, can still produce considerably different results. Therefore, multiple tests (3 per alloy and for each heat treatment) have been performed to determine the mechanical properties. These results are summarized in tables 3.5 and 3.6. In addition, the mean and the standard deviation of values are reported in order to show the variability of the results.

3.5.1.3 Results

Tables 3.5 and 3.6 present results of tensile test for both un-modified and Sr-modified A356.0 alloy.

Table 3.5. Results of mechanical tests performed on samples of un-modified A356.0 alloy with different heat treatments.

Alloy/Item		Heat treatment	Ultimate tensile strength UTS [MPa]	Mean UTS [Mpa]	Standard deviation UTS	Elongation A [%]	Mean A[%]	Standard deviation A
A356.0	A	T0	146,88	144,45	8,17	2,2	2,20	0,2
	B		151,12			2,0		

	C		135,33			2,4		
6.0	A	T4	190,56	194,48	12,01	4,0	3,87	0,81
	B		184,93			3,0		
	C		207,96			4,6		
6.0	A	T6	273,95	262,99	9,65	2,1	2,17	0,21
	B		259,25			2,4		
	C		255,78			2,0		

Table 3.6. Results of mechanical tests performed on samples of A356.0-Sr modified alloy with different heat treatments.

Alloy/Item		Heat treatment	Ultimate tensile strength UTS [MPa]	Mean UTS [Mpa]	Standard deviation UTS	Elongation A [%]	Mean A[%]	Standard deviation A
A356.0-Sr 0,03	A	T0	156.23	159.22	2.59	3.32	3.62	0.28
	B		160.85			3.88		
	C		160.58			3.66		
A356.0-Sr 0,03	A	T4	211.44	220.71	9.88	6.24	6.57	0.58
	B		219.57			6.22		
	C		231.12			7,24		
A356.0-Sr 0,03	A	T6	267.39	263.77	3.57	2.16	2.22	0.18
	B		263.54			2.08		
	C		260.25			2.42		

From the results summarized in Tables 3.5 and 3.6, the following conclusions are drawn:

- For the A356.0-Sr0.03 modified alloy specimens with thermal treatment T0 and T4, both the ultimate tensile strength and the elongation to fracture are greatly improved;
- For the A356.0-Sr0.03 modified alloy specimens with heat treatment T6 there is a slight improvement in the ultimate tensile strength (less variation between different samples, lower standard deviation) and the percentage elongation to fracture, compared to the traditional A356.0 alloy.

From these results it can be stated that the modified alloy presents better mechanical properties than the standard alloy, especially for the thermal treatments T0 and T4.

3.5.2 Electrical Properties

Electrical resistivity (also known as specific electrical resistance or volume resistivity) is an intrinsic property that quantifies the intensity with which a given material opposes to the flow of electric current. A low electrical resistivity of the material indicates that it easily allows the movement of the electric charge. The SI unit of electrical resistivity is the ohm-meter ($\Omega \cdot m$).

In metals, crystalline defects serve as scattering centers for conduction electrons, therefore, their number determines the resistivity of material. The concentration of crystalline imperfections depends on temperature, composition, and the degree of cold work of a metal specimen. Experimental measurements collected in technical literature demonstrated that the total resistivity of a metal is the sum of the contributions from thermal vibrations, impurities, and plastic deformation and this phenomena act independently of one another [36].

The electrical resistivity of the un-modified A356.0 alloy and the A356.0-Sr0.03 modified alloy were measured at room temperature and also from room temperature to 200 °C in order to determine the temperature coefficient of the resistivity.

3.5.2.1 Resistivity measurements at room temperature

The resistivity ρ of a metal can be measured directly in a sample of constant section, when the total resistance of the sample R , the length L and the area A of the cross section of the bar are known.

$$\rho = \frac{R \cdot A}{L} \quad (3.3)$$

The experimental method requires great care to ensure that the results adequately represent metal resistivity. In this sub-section the procedure used to measure resistivity at room temperature is described and obtained results presented.

Specimens of both un-modified A356.0 and A356.0-0.03Sr modified alloys used for the electrical resistivity measurement were fabricated by sand casting and subsequently heat treated following the same manufacturing method of the substation connectors. Then they were machined to obtain a constant, square or circular section, with a total length of 150 mm. The dimensions of the test pieces with the relative dimensional tolerances are summarized in Table 3.7.

The **cross section area** of the specimen was measured with great precision to obtain a good measure of the resistivity. A digital micrometer was employed to measure the cross section area of the test specimens (the side l in the case of square section specimens and the diameter D in the case of circular section specimens). Side l and diameter D measurements were made at six points equidistant from each other along the total length of the specimen. For the calculation of the electrical resistivity, the average value of the cross section at the six points was considered.

Another important parameter is the **length L** or distance between the test points that was used to measure the voltage drop by applying the 4-point method. This distance was determined with a caliper.

During the test the room **temperature** was measured using a digital thermometer.

The effects of human body heat, the Joule heating due to the DC current flowing, and room temperature gradients can cause a temperature rise in the object under test. Therefore, the surface temperature of the conductor was monitored during the measurement through a K type thermocouple placed in contact with the surface of the specimen.

Finally, in order to determine the resistivity, **electrical resistance measurement R_x** of the test specimens was carried out. The Kelvin or 4-wire method was employed, using a Raytech Micro-Centurion II digital micro-ohmmeter, with the following characteristics: 0-200 A_{DC}, accuracy $\pm 0.1\%$ reading $\pm 0.01\mu\Omega$.

Measurements were performed between point A and point B of the testing specimen. Testing DC current was settled to 5 A_{DC}, this value was chosen with the aim to ensure an adequate accuracy but also to prevent the heating of the testing object due to the current flow.

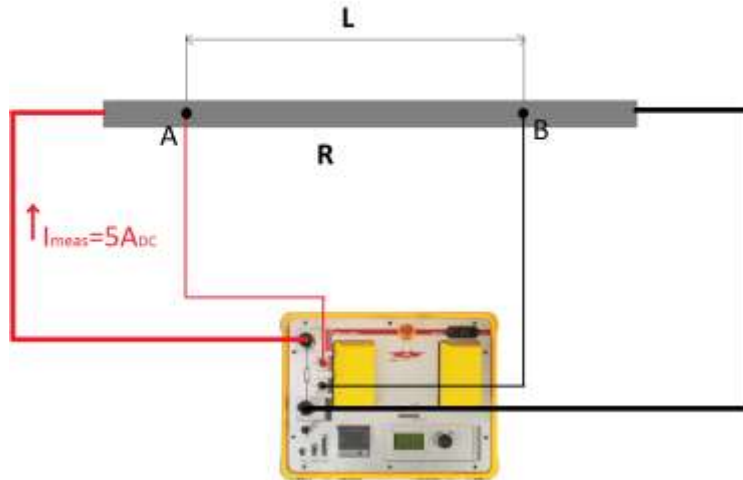
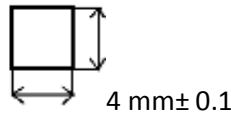
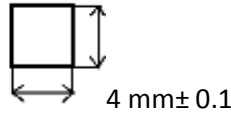
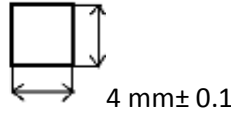
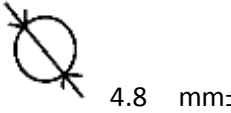


Figure 3.11. Scheme of the test setup for measuring electrical resistivity of the alloys.

Table 3.7. Specimens used for the measurement of the electrical resistivity and the resistivity coefficient.

Alloy	Heat Treatment	Number of specimens	Dimensions	Length
A356.0	T0	5	 4 mm ± 0.1	150 mm ± 1 mm
A356.0	T4	5	 4 mm ± 0.1	150 mm ± 1 mm
A356.0	T6	5	 4 mm ± 0.1	150 mm ± 1 mm
A356.0-0.03Sr	T0	4	 4.8 mm ± 0.1	150 mm ± 1 mm

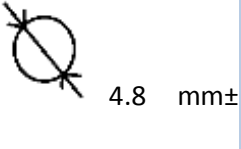
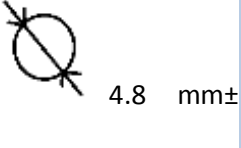
A356.0-0.03Sr	T4	3		150 mm ± 1 mm
A356.0-0.03Sr	T6	4		150 mm ± 1 mm

Table 3.8 shows the results of the electrical resistivity of the standard A356.0 and A356.0-Sr0.03 modified alloy obtained in this project, normalized at 20°C.

Table 3.8. Average resistivity of the standard A356.0 and A356.0-Sr0.03 modified at 20°C.

Alloy	Heat Treatment	Number of samples	Mean value of resistivity at 20°C (ρ, $10^{-8} \Omega \cdot m$)
A356.0	T0	5	5.27
A356.0	T4	5	5.24
A356.0	T6	5	5.21
A356.0- 0.03Sr	T0	4	4.46
A356.0- 0.03Sr	T4	3	4.45
A356.0- 0.03Sr	T6	4	4.27

Results presented in Table 3.8 show that for both alloys the T6 heat treatment is the one that allows obtaining a smaller resistivity, whereas the T0 (as cast) is the one that provides a higher resistivity. Comparing the electrical resistivity values of the un-modified A356.0 alloy and the A356.0-Sr0.03 modified alloy at 20 °C, a decrease of more than 15% of the resistivity can be observed in the case of the modified alloy for the three analyzed heat treatments. This fact is very important as it will allow a better thermal behavior of the high-capacity substation connector.

The decrease of the electrical resistivity is due to the differences in microstructure of the two alloys, in particular it can be observed that the eutectic silicon shape and size have an important influence on the determination of the electrical properties, since electrons flow more easily through smaller eutectic regions.

3.5.2.2 Temperature coefficient of resistivity

The electrical resistivity of conductive materials increases with temperature. The temperature dependence of resistivity in conductor materials can be considered linear within a limited temperature range and described by the following approximation:

$$\rho = \rho_0 \cdot [1 + \alpha \cdot (T - T_0)] \quad (4)$$

where α is the temperature coefficient of the electrical resistivity.

In order to measure the temperature coefficient of electrical resistivity, electrical resistance measurement of the analyzed specimens was carried out from cryogenic temperatures (boiling point of liquid nitrogen, $-195.79\text{ }^{\circ}\text{C}$) to 200°C . The Kelvin or 4-wire method was applied using a stabilized DC source of 3A and a digital voltmeter (Fig. 3.12 a).



Figure 3.12. Experimental setup for the measurement of the temperature coefficient of electrical resistivity a) Simplified scheme of the test setup for the measurement from room temperature to 200°C . b) Stabilized current source and voltage and current measurement system. c) Temperature-controlled electric oven d) Resistance measurement of the test specimen at temperature of boiling point of liquid nitrogen stored in a vacuum flask. e) Resistance measurement of the test specimen at temperature of sublimation temperature of dry ice placed in an insulated box .

The electric potential difference is measured through two tips placed in contact with the surface of the specimen, fastened through a ceramic bar, as it can be seen in Fig 3.13. The surface temperature of the sample was measured by using a T-type thermocouple placed in contact with the surface of the specimen.

A temperature controlled electric oven (Fig. 3.12 c) was employed to heat the specimen to the desired temperature from room temperature to 200°C .

Temperature coefficient of resistivity was also characterize at cryogenic temperatures. Specimen resistance was measured at the sublimation temperature of dry ice, the solid form of carbon dioxide, ($-78.5\text{ }^{\circ}\text{C}$) and liquid nitrogen boiling point ($-195.79\text{ }^{\circ}\text{C}$), as shown in fig. 3.12 d) and e).

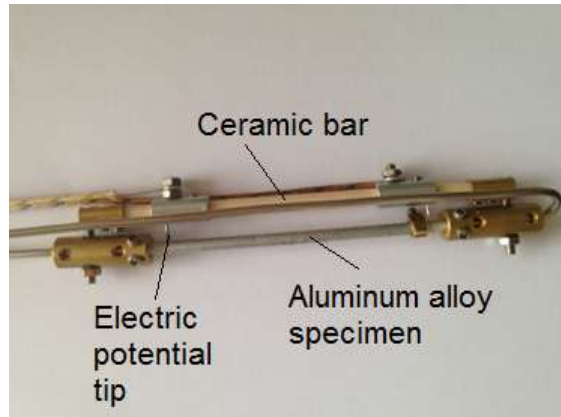


Figure 3.12. Experimental setup for the measurement of the temperature coefficient of electrical resistivity. Fixing system of the testing specimen.

Tables 3.9 and 3.10 show the variation of the temperature coefficient of resistivity of the un-modified A356.0 and A356.0-Sr0.03 modified alloys obtained in this project.

Table 3.9. Temperature coefficient of resistivity of the un-modified A356.0 and A356.0-Sr0.03 modified alloys from room temperature to 200°C.

Alloy	Heat treatment	Number of samples	Temperature range	Mean temperature coefficient ($\alpha, 10^{-3} \text{ }^{\circ}\text{C}^{-1}$)
A356.0	T0	5	20 < T <= 50 °C	27
			50 < T <= 100 °C	25
			100 < T <= 150 °C	23
			150 < T <= 200 °C	20
	T4	5	20 < T <= 50 °C	25
			50 < T <= 100 °C	23
			100 < T <= 150 °C	21
			150 < T <= 200 °C	16
	T6	5	20 < T <= 50 °C	24
			50 < T <= 100 °C	23

			100 < T <= 150 °C	19
			150 < T <= 200 °C	17
A356.0- 0.03Sr	T0	4	20 < T <= 50 °C	29
			50 < T <= 100 °C	25
			100 < T <= 150 °C	22
			150 < T <= 200 °C	19
	T4	3	20 < T <= 50 °C	27
			50 < T <= 100 °C	24
			100 < T <= 150 °C	21
			150 < T <= 200 °C	19
	T6	4	20 < T <= 50 °C	29
			50 < T <= 100 °C	26
			100 < T <= 150 °C	24
			150 < T <= 200 °C	19

Table 3.10. Temperature coefficient of resistivity of the un-modified A356.0 and A356.0-Sr0.03 modified alloys at cryogenic temperatures.

Alloy	Heat treatment	Number of samples	Temperature range	Mean temperature coefficient (α, $10^{-3} \text{ }^{\circ}\text{C}^{-1}$)
A356.0	T0	2	-78.5 < T <= 20 °C	31
			-196 < T <= -78.5 °C	32
	T4	2	-78.5 < T <= 20 °C	28
			-196 < T <= -78.5 °C	29
	T6	2	-78.5 < T <= 20 °C	30

			-196 < T <= -78.5 °C	30
A356.0- 0.03Sr	T0	2	-78.5 < T <= 20 °C	32
			-196 < T <= -78.5 °C	31
	T4	2	-78.5 < T <= 20 °C	27
			-196 < T <= -78.5 °C	27
	T6	2	-78.5 < T <= 20 °C	30
			-196 < T <= -78.5 °C	31

3.5.3 Thermal conductivity

Thermal conductivity is a material property describing its ability to conduct heat. Thermal conductivity can be defined as the quantity of heat transmitted through a unit thickness of a material (in a direction normal to a surface of unit area) due to a unit temperature gradient under steady state conditions. The SI unit of thermal conductivity is W/(m·K).

In solid materials heat transport is due to lattice vibration waves (phonons) and free electrons. Thermal conductivity is determined by these two mechanisms and the total conductivity is the sum of the two contributions. In metals a large numbers of free electrons participate in thermal conduction, consequently, metals usually exhibit high thermal conductivity [36].

Alloying metals with impurities results in a reduction in the thermal conductivity, for the same reason that has been explained for the electrical conductivity, that is, the impurity atoms act as scattering centers, which results in a decrease of electron motion efficiency. This effect is more accentuated if impurity atoms are in solid solution.

3.5.3.1 The Wiedemann–Franz law

The thermal conductivity of metals is quite high and those metals that are the best electrical conductors are also the best thermal conductors. At a certain temperature, the thermal and electrical conductivities of the metals are proportional, but increasing the temperature increases the thermal conductivity while decreasing the electrical conductivity. This behavior is quantified in the Wiedemann-Franz law [54]:

$$L = \frac{k}{\sigma T} \quad (5)$$

where the constant L is the Lorenz number, k the thermal conductivity in W/(m·K), σ the electrical conductivity in S/m and T the absolute temperature in K. This relationship is based on the fact that in both heat and electric transport, the free electrons of the metal are involved. The thermal conductivity

increases with the average velocity of the particles because these increase the energy transport. However, the electrical conductivity decreases with increasing particle velocity, because collisions divert electrons from the charge transport path. The ratio of thermal to electrical conductivity depends on the square of the mean velocity, which is proportional to the kinetic temperature.

3.5.3.2 Experimental setup

The system consists of three parts, the heating element (hot source), the testing object and the cold source.

The heating element consists of an embedded heating resistor with an electrically power supply system. The heating element acts as hot source with the objective to provide and control heat supplied to the testing specimen. A hole has been drilled on the top point of the testing specimens with the aim to insert the heating resistor, in order to create a temperature gradient along the test sample.

The testing specimen is an aluminum alloy bar with cylindrical section, which drawing is shown in Fig. 3.13.

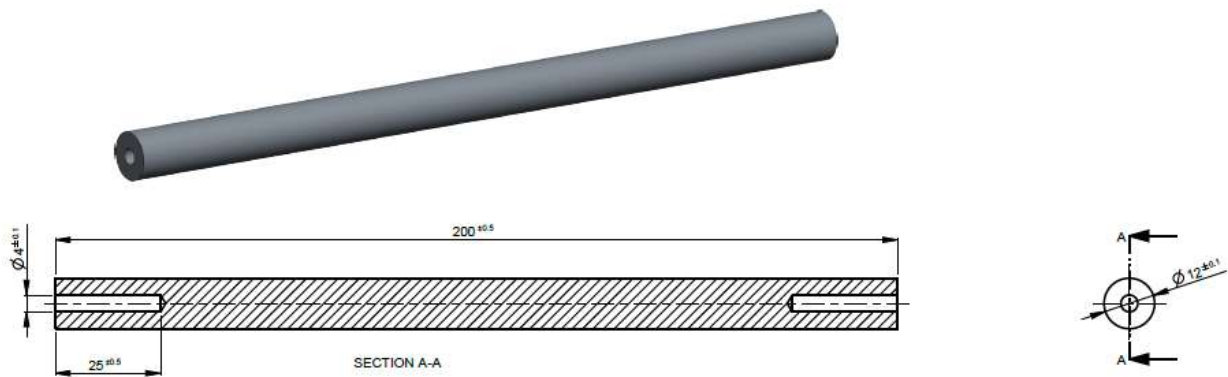


Figure 3.13. Test specimen use for the measurement of thermal conductivity.

A set of calibrated T-type thermocouple has been used to measure temperature at different points along the testing specimens. Five circular openings (of known length with 40 mm spacing) have been drilled through the specimen surface for the insertion of thermocouples for temperature measurements.

The cold-end source consists of an aluminum block with a volume of $0.12 \times 0.12 \times 0.04 \text{ m}^3$, which thermal inertia is sufficiently high to create the thermal gradient required for heat flow. The aluminum block was designed to hold the cylindrical specimen.

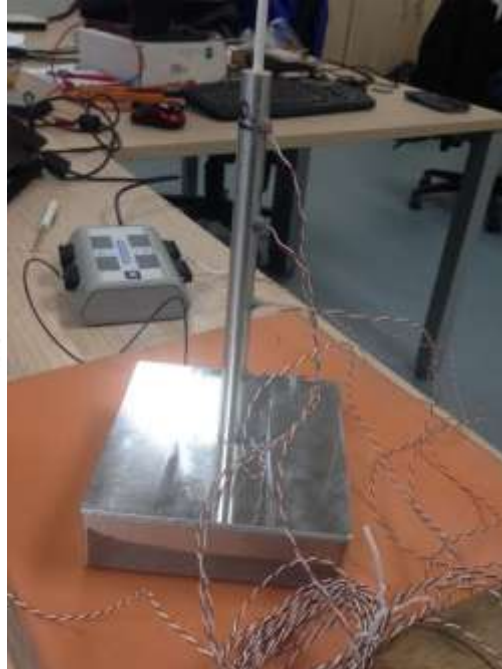
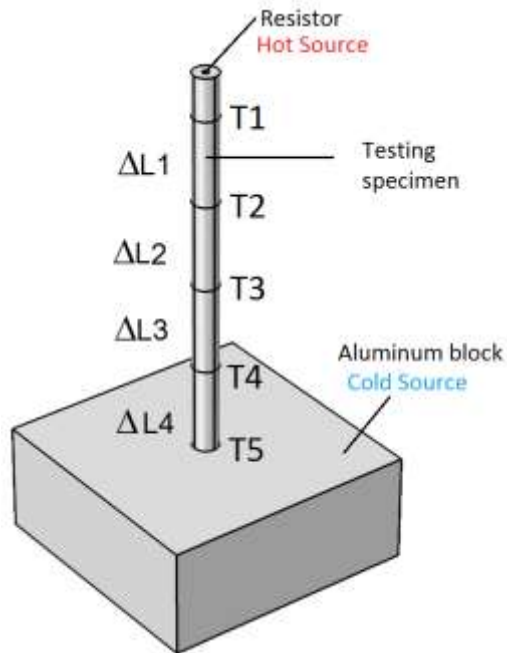


Figure 3.14. Experimental setup for the measurement of thermal conductivity.

3.5.3.3 Thermal conductivity calculation

Heat conduction occurs when a body is exposed to temperature gradient and heat flows from the higher temperature region to the lower region. Under the hypothesis that heat is transferred only by conduction, if the metal is uniform (in terms of composition and dimensions) the temperature along a chosen length decreases uniformly with distance from the relatively hot region to the cold point.

The designed system to measure thermal conductivity is based on the definition of thermal conductivity as the quantity of heat, ΔQ , transmitted during time Δt through a thickness ΔL , in a direction normal to a surface of area A , per unit area of A , due to a temperature difference ΔT , under steady state conditions and when the heat transfer is dependent only on the temperature gradient.

$$k = \frac{\Delta Q}{\Delta t} \frac{\Delta L}{A \Delta T} = P_{in} \frac{\Delta L}{A \Delta T} \quad (6)$$

Being ΔL the distance between measuring points in m , A the cross section of the testing specimen in m^2 , ΔT the temperature gradient in K , Q the thermal energy and t the time in s .

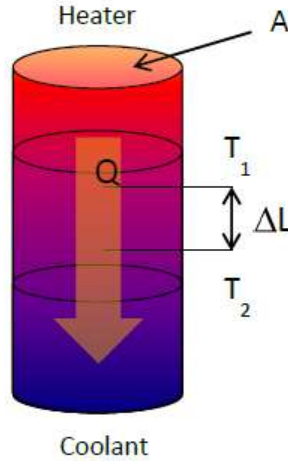


Figure 3.15. Simplificated scheme which explain the mechanism of thermal conduction. the quantity of heat, ΔQ , is transmitted during time Δt through a thickness ΔL , in a direction normal to a surface of area A , due to a temperature difference ΔT .

The ration $\frac{\Delta Q}{\Delta t}$ is the thermal energy in W which enter in the system and can be written as P_{in} .

If thermal energy is generated by electric heating system, like a resistor, P_{in} it can be expressed as function of the current I in A and voltage V in V applied to the heater.

$$P_{in} = P_{el} = V \cdot I \quad (7)$$

Moreover, it is necessary to take into account that in experimental measurement it is practically impossible to perfectly isolate the testing probe from the surrounding air. Therefore, heat transfer depends also on convective and radiative phenomena along the sample's boundaries, and has to be taken into account in the calculation of the thermal conductivity.

Convective and radiative heat flux can be calculated as follows:

$$Q_{conv} = S_{ext} \cdot h \cdot (T_{surf} - T_{air}) \quad (8)$$

$$Q_{rad} = S_{ext} \cdot \sigma \cdot \varepsilon \cdot (T_{surf}^4 - T_{air}^4) \quad (9)$$

where S_{ext} is the surface in contact with surrounding air in m^2 , h the convective coefficient in $W \cdot m^{-2} \cdot K^{-1}$, T_{surf} the surface temperature in K, T_{air} the room temperature in K, ε is the dimensionless emissivity coefficient and σ ($W / (m^2 \cdot K^4)$) is the Stefan–Boltzmann constant. To calculate the surface-to-ambient radiation, it is assumed that the ambient behaves as a black body at the temperature T_{air} .

Therefore, taking into account convective and radiative phenomena, thermal conductivity becomes:

$$k = (VI - Q_{conv} - Q_{rad}) \frac{\Delta L}{A \Delta T} \quad (10)$$

To estimate the conductive and radiative heat flux along the external surface of the testing specimen, thermal FEM simulations have been conducted for each testing sample. An example of results provided by thermal simulations is shown in Fig. 3.16.

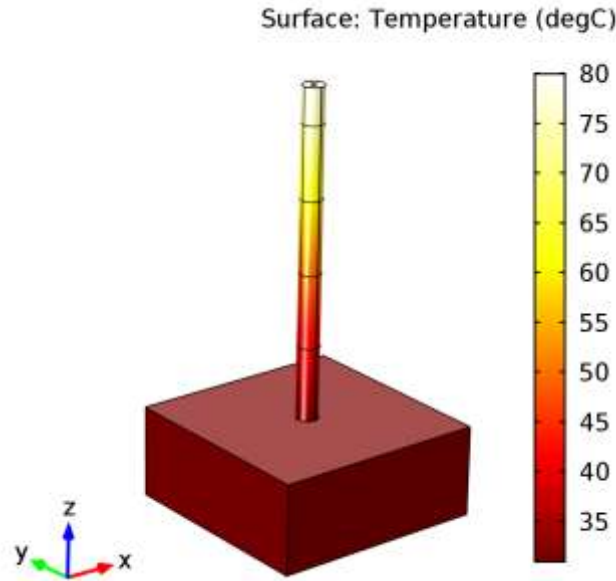


Figure 3.16. Example of 3D-FEM thermal simulation used to estimate convective and radiative heat flux on external boundaries of the testing specimens.

3.5.3.4 Results

Results presented in Table 3.11 show that for both alloys the T6 heat treatment is the one that allows obtaining a higher thermal conductivity. Analyzing thermal conductivity values of the unmodified A356.0 alloy and the A356.0-Sr0.03 modified alloy at room temperature, it can be observed that thermal conductivity in modified alloy increases by more than 15% for the three analyzed heat treatments, compared with the un-modified alloy. Higher thermal conductivity will allow a better thermal behavior of the high-capacity substation connector.

Table 3.9. Average thermal conductivity of the standard A356.0 and A356.0-Sr0.03 modified at 25°C.

Alloy	Heat Treatment	Number of samples	Mean value of resistivity at 20°C (ρ , $10^{-8} \Omega \cdot m$)
A356.0	T0	3	139.6
A356.0	T4	3	136.8
A356.0	T6	3	144.4
A356.0- 0.03Sr	T0	3	143.0
A356.0- 0.03Sr	T4	3	147.8
A356.0- 0.03Sr	T6	3	151.2

4. Contact Resistance

The contact resistance defines the energy-efficiency, the stable performance and the long-term service of an electrical connection. If the contact resistance is low and stable in time, a good electrical connection and a long-term performance of substation connector is guaranteed; whereas, if it is high and unstable in time, it could cause overheating of the connector and, consequently, a reduced operating life [10].

Substation connectors are usually considered the weakest points in the power grid, mainly due to the poor installation practice and the lack of knowledge of their degradation rate [55]. These facts often involve the difficulty to predict the useful life of a component. Moreover, it is worth mentioning that the mechanical, metallurgical, thermal and electrical processes involved in the establishment and the maintenance of the electrical contact are very complex and nowadays there is a lack of a unified model which describes the phenomena occurring at contact interface [55]. With the advent of HTLS conductors, the role of the substation connectors in the transmission and distribution system is even more critical, because high temperature operation of conductors increases the current density and operating temperature of associated connectors. As a consequence, the aging process of connectors is accelerated, and thus their expected service life reduced. Temperature cycling tests (at 125 °C and 150 °C) conducted on connectors that were originally rated for 70 °C operating temperature have detected the electrical and thermal deterioration in most types of connectors [56].

Thus, if HTLS cables will replace traditional conductors, the installed population of connectors will age more rapidly and the number of connector failures will increase due to the increased aging effects of higher temperature and current density.

4.1 Chemical cleaning to reduce the contact resistance

Connector's long term performance is directly related to the contact points established during installation [10]. The restriction of current flow to these few contact points, shown in Fig. 4.1, also known as "a-spots," constitutes a first contribution to the total contact resistance; this component is usually called constriction resistance [12].

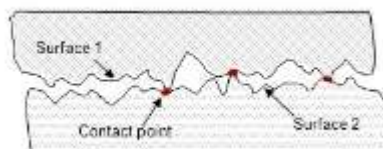


Figure 4.1. Conductor's surfaces on the micro scale. Current flow is restricted to contact points established during installation.

Constriction resistance depends on some properties of conductor materials, such as hardness and electrical resistivity, applied bolts torque, apparent contact area, or surface's conditions among others.

Moreover, it is necessary to take into account the presence of a contact interface due to a thin oxide film. The common used material to manufacture substation connectors is A356.0 aluminum cast alloy. It is well known that aluminum and its alloys react quickly with atmospheric oxygen, and a passivation layer of few nanometers of aluminum oxide, usually known as alumina, grows on atmospheric exposed aluminum surfaces [13]. Since the aluminum oxide is very insulating material, the electrical current can pass across the alumina only thanks to tunneling and fritting mechanisms [55]. As consequence, the film resistance is the second component of the total contact resistance of a joint. However, a good electrical contact between two conductors can be established only if the contact spots can be created by means of the mechanical rupture of the oxide insulating film [55].

This study aims to propose a surface treatment for substation connector's and the associated conductors, which allows reducing the contact resistance. This treatment consists on a chemical cleaning before conventional substation connector's installation. Contact surface preparation is essential to guarantee proper contact between connector and conductor since the contact resistance can notably degrade substation connectors' performance.

4.1.1 Analyzed substation connectors and installation procedures

Resistance measurements of contact resistance at room temperature has been conducted on a junction composed by different typologies of substation connectors from SBI Connectors catalogue and 32 mm diameter AAAC conductors. Specifically, analyzed connectors are listed below:



Figure 4.2. The substation connectors analyzed. a) S330TLS t-type connector. b) S330SLS coupler connector. c) S330SNS coupler connector

- T-connector S330TLS (I);
- Coupler with two caps S330SLS (II);
- Coupler with three caps S330SNS (III).

Different assembling procedures and surface treatments, summarized in Table 4.1, are studied.

Table 4.1. Installation procedures applied to substation connectors.

Installation procedure	Conductor's treatment	surface	Connector's Treatment	Surface
1	Not treated		Not treated	

2	Brushed Oxide inhibiting compound application	Brushed Oxide inhibiting compound application
3	Brushed Oxide inhibiting compound application	Chemical cleaning Oxide inhibiting compound application

The conventional assembling procedure consists in brushing both conductor and connector's surfaces just before assembling, with the aim to remove the aluminium oxide film (alumina). After brushing it is generally a recommended practice to paint both contact surfaces with an oxide inhibiting compound. These compounds ensure good contact and enhance the expected life of the connection [11].

Chemical cleaning treatment involves the application of a chemical solution on the contact surfaces between the connector and the conductor during about 45 minutes, after which the components were assembled according to the standard procedure.

4.1.2 Contact resistance measurements

The Kelvin or 4-wire method was employed to perform resistance measurements, as shown in Fig. 4.3. To this end a Raytech Micro-Centurion II digital micro-ohm meter (max. current 200 A_{DC}, accuracy ± 0.1% Reading ±0.01μΩ) was used. Resistance measurement was performed between points A and B as shown in Fig. 4.3. The theoretical resistance of the connectors was calculated through electromagnetic FEM-simulation, which was subtracted from the measured resistance, thus obtaining the contact resistance.

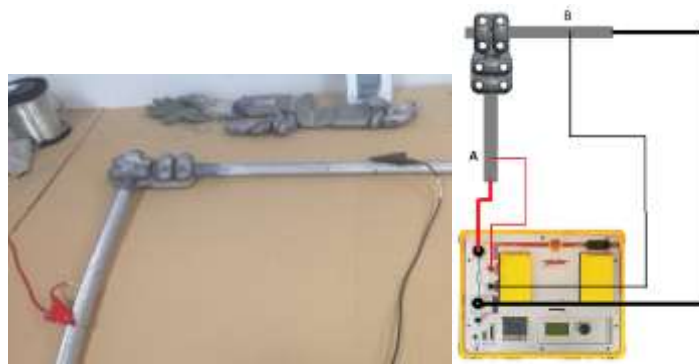


Figure 4.3. Resistance measurement with the Kelvin 4-wire method.

Table 4.2. Measured values of contact resistance a total connector's resistance.

	S330TLS		S330SLS		S330SNS	
Installation procedure	Contact Resistance (μΩ)	Total Resistance (μΩ)	Contact Resistance (μΩ)	Total Resistance (μΩ)	Contact Resistance (μΩ)	Total Resistance (μΩ)
1	32.16	36.37	51.42	55.28	52.33	57.13

2	8.74	12.95	11.01	14.87	9.89	14.69
3	4.88	9.09	4.54	8.40	5.87	10.58

Resistance measurements shown in Table 4.2 indicate that when no surface treatment is applied (procedure 1), the contact resistance is very high, since the rupture of the alumina film caused by the axial force due to the bolts assembly is not enough and, therefore, few contact points have been established between the contact surfaces of the conductor and connector. The conventional installing procedure (2) results in an important decrease of the contact resistance compared to procedure 1, due to the mechanical rupture of the oxide insulating film by brushing surfaces.

With procedure 3 a significant decrease of the contact resistance is obtained compared to the conventional procedure, through the almost complete removal of the oxide layer from the surface of the connector.

Experimental resistance measurements clearly demonstrate that oxides and contaminants difficult the establishment of a good electrical connection.

4.1.3 Components of connector's resistance

In Fig. 4.4 the different components of S330SNS connector's resistance with the three installation methods are shown. Thanks to estimated value of constriction resistance, calculated by means of Holm-Greenwood model (eq. 5), which will be fully described in section 4.4.3.1 it is possible to note that, with the novel chemical cleaning proposed by the authors (procedure 3), the contact resistance component due to the oxide film is practically eliminated.

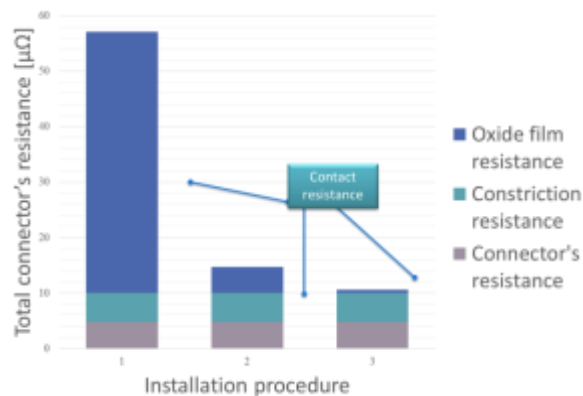


Figure 4.4. Components of contact resistance for the three installation procedures analyzed.

4.2 Improved thermal behavior due to the chemical cleaning

As introduced below, if HTLS cables will replace traditional conductors, the installed population of connectors will age more rapidly and the number of connector failures will increase due to the increased aging effects of higher temperature and current density.

Hence the need to characterize the thermal behavior of an electrical contact and optimizing the installation procedure of substation connectors in order to reduce contact resistance and ensure a lower temperature during normal operating conditions. In section 0 it has been shown that contact surface preparation is essential to guarantee proper contact between connector and conductor, since the contact resistance can notably degrade substation connectors' performance. In the technical literature the most common installation procedures for aluminum-to-aluminum and aluminum-to-copper connections and their performances under thermal cycling are analyzed and compared [12][15][16][17][18]. Most of these works, have shown that the mechanical abrasion (reached by brushing surfaces) and lubrication through contact aid compound application is the most efficient method to ensure an adequate contact resistance in aluminum-to-aluminum connections [55]. However, this practice can be further improved with the chemical cleaning described in section 4.1. Results presented have shown that the proposed installation procedure allows minimizing the contact resistance of substation connectors, and thus improving energy efficiency of the electrical connection.

The aim of this section is to characterize the relationship between installation procedure, the resulting contact resistance and the thermal performance of substation connectors. First of all the thermal behavior of substation connectors assembled with the traditional [11] and the new installation method proposed by the authors [57] will be characterized by means of the experimental Temperature Rise test according to the ANSI/NEMA CC1-2009 standard [4], the Current Cycle test according to ANSI C119.4-2011 standard [28] and the short-time withstand current test described in the IEC 62271-1:2007 [29] standard. Thanks to these results, the temperature and the variation of contact resistance due to thermal stress, with the two installation methods, will be analyzed and compared. Moreover, by means of experimental measurements, the temperature dependence of the contact resistance will be analyzed, with the aim to characterize the performance of an electrical contact at high operating temperatures.

Finally, to determine the temperature coefficient of the contact resistance, an experimental resistance measurement will be performed continuously during the cooling phase of a contact interface, which was previously heated at 200 °C.

4.2.1 Traditional Installation Procedure vs Chemical Cleaning

Experimental temperature rise and current cycle tests have been conducted on a loop composed by two different typologies of substation connectors from SBI Connectors catalogue and 32 mm diameter AAAC conductors. Specifically, the analyzed connectors are listed below:

- T-connector S330TLS (a);
- Coupler with two caps S330SLS (b);

The experimental test to characterize temperature dependence of the contact resistance has been conducted on a smaller loop composed by a S330SLS connector, which joined two 32 mm diameter AAAC conductors.

Also the experimental short-time withstand current test has been conducted on a smaller loop composed by a S285TLS connector, which joined two 27.6 mm diameter GTACSR conductors.



Figure 4.5. The substation connectors analyzed. a) S330TLS t-type connector. b) S330SLS coupler connector. c) S285TLS t-type connector

Different assembling procedures and surface treatments are analyzed and shown in Table 4.3.

Table 4.3. Installation procedures applied to analyzed connectors.

Installation Procedure	Surface's Treatments	
	AAAC Conductor	Substation Connector
1	<ul style="list-style-type: none"> • Brushed • Oxide inhibiting compound application 	<ul style="list-style-type: none"> • Brushed • Oxide inhibiting compound application
2	<ul style="list-style-type: none"> • Brushed • Oxide inhibiting compound application 	<ul style="list-style-type: none"> • Chemical cleaning • Oxide inhibiting compound application

4.2.2 Experimental validation of the thermal improvement due to the chemical cleaning

4.2.2.1 Test 1: Temperature rise test. Traditional procedure vs chemical cleaning.

The temperature rise test is useful to determine the substation connector's thermal behavior under both transient and steady state condition and thus to evaluate if its design and installation procedure are compatible with the electromagnetic-thermal stress at which it is subjected. The temperature rise is determined at 100, 125, and 150% of the rated current, with equilibrium temperatures obtained at each level. The standard describes equilibrium temperature as a constant temperature (± 2 °C) between three successive measurements taken five minutes apart. The rated current shall be in accordance with tabulated values that establish this value as function of conductor size.

A temperature rise test according to the requirements of the NEMA CC1-2009 [4] was conducted in the AMBER-UPC laboratory. The test object was a closed loop circuit composed of eight connectors, as shown in Fig. 4.6. It included four S210ZTLST-connectors, four S210ZA4P23LS terminals and an AAAC SALCA 593 conductor with diameter $d = 32$ mm. The two t-connectors closer to the transformer terminals were used with the sole purpose of connecting the loop to the power transformer, so they were not taken into account for this analysis. Three connectors were installed according to procedure n° 1, as shown in Fig. 4.6, whereas the remaining connectors were installed according to procedure No. 2, with the purpose of comparing the thermal behavior of connectors assembled with the different

procedures. The experimental test was performed at atmospheric conditions (18 °C). Current values settled during the test are shown in Table 4.4.

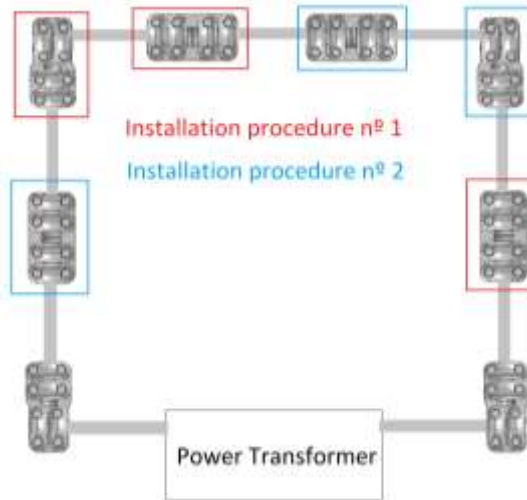


Figure 4.6. Experimental temperature rise test. Testing loop with connectors with different installation procedures. Connectors assembled with procedure No. 1 are indicated in red, whereas connectors installed with procedure No. 2 in blue.

Table 4.4. Current values settled during the temperature rise test.

Step	Testing current	
	% of nominal current	Value [A _{RMS}]
1	100 %	1015
2	125 %	1270
3	150%	1525

The experimental setup consists of a single-phase variable autotransformer connected in series with a single-phase transformer (120 kVA, 0-10 kA, 50 Hz). They are connected to the test loop, which includes the eight connectors described above. A calibrated Rogowski coil probe (Fluke i6000s Flex) was employed to measure the output current provided by the transformer at each current level. Current measurements have an uncertainty of about 2%.

To measure the temperature evolution during the transient phase and in steady state condition, 16 K-type thermocouples with an AISI 316 external sheath of 1 mm diameter were placed on the connectors' bodies and on the top points of two AAAC conductors. A small hole was drilled through the connector body, to ensure the contact of the thermocouple with the connector surface. The thermocouples were connected to an acquisition card and the signal was processed by a PC. Measures were acquired every 10 seconds.

Results

The temperature rise test allows determining the substation connector’s thermal behavior under both transient and steady state condition. The test was performed at three current levels, as indicated in Table II. Fig. 4.7 shows the temperature rise for the three current levels, and the zoom of the third current step, that is at 150% of nominal current, for the six connector analyzed.

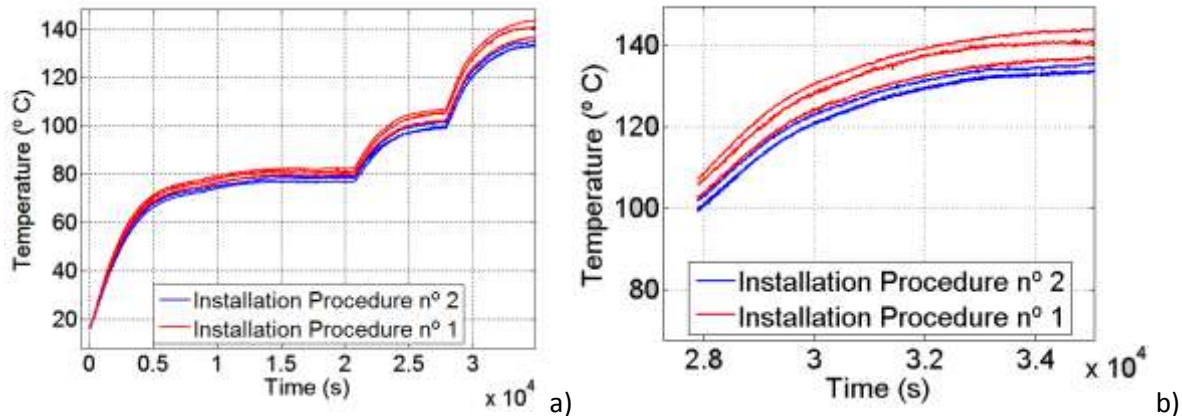


Figure 4.7. a) Results of the experimental temperature rise test. In red it is shown the temperature of the connectors installed with procedure No.1, whereas in blue connectors assembled with procedure No. 2. b) Zoom of the third step, performed at 150% of nominal c current.

The test demonstrates a better thermal behavior of the connectors installed with procedure No. 2, showing a lower transient and steady-state temperature, compared to the temperature of connectors assembled with the traditional procedure.

Table 4.5. Temperature rise test. Steady state temperatures of analyzed connectors, at the third current step.

Connector			Steady-state Temperature (°C) at $I_3= 1522 A_{RMS}$		
				Mean	Std. Deviation
Type	Item	Inst. Procedure			
T	3	1	141.4	140.8	3.4
Coupler	4		143.9		
Coupler	7		137.15		
Coupler	2	2	133.5	134.3	1.1
Coupler	5		133.8		
T	6		135.6		

Moreover it should be noted that, as summarized in Table 4.5 with procedure No. 2 there is less variation of temperature between the three specimens analyzed with the same treatment. This behavior is very important to evaluate the stability and the reliability of a connector.

4.2.2.2 Test 2: Current Cycle test. Traditional procedure vs chemical cleaning.

Connector's behavior can also be evaluated by means of the standard current cycle test regulated by the ANSI C119.4-2011 standard [28]. The current cycle test is a very important tool to evaluate the aging process of connectors. Thermal cycles result in thermal expansion and contraction of the electrical contact interface, which contributes to degrade the contact points [55]. The test current must be adjusted to result in a steady-state temperature rise on the control conductor between 100°C and 105°C above ambient temperature.

Temperature measurements of the connectors, conductors, and ambient air have to be made at the end of the specified heating cycle, immediately before the current is turned off, whereas resistance measurements have to be made at the end of the heating cycle period, with all connectors thermally stabilized at the room temperature. Fifteen thermal cycles according to the requirements of the ANSI C119.4-2011 standard were conducted in the AMBER-UPC laboratory. The test object and the experimental setup, shown in Fig. 4.8, were the same explained in the previous section. Experimental tests were performed at atmospheric conditions (15 °C). An additional K-type thermocouple was used to measure the room temperature.



Figure 4.8. Heat-cycle test. Experimental setup.

Results

As explained in the previous chapter, the current cycle test allows determining the thermal aging of substation connectors. Fifteen thermal cycles according to the requirements of the ANSI C119.4-2011 standard were conducted in the AMBER-UPC laboratory. Table IV shows the temperature measurements performed at the end of the last heating cycle, immediately before the current is turned off. Table V shows the connector's resistance, the contact resistance and its variation before and after the test.

The theoretical resistance of the connector was calculated through electromagnetic FEM-simulation, which was subtracted from the measured resistance, thus obtaining the contact resistance. Results summarized in Table 4.6 show that connectors assembled according to procedure No. 2 have a lower steady-state temperature, compared to the connectors assembled with the traditional procedure.

Table 4.6. Heat cycle test. Steady state temperatures of analyzed connectors. Cycle No. 15.

Connector	Steady-state Temperature (°C)
-----------	-------------------------------

			Cycle 15
Type	Item	Inst. Procedure	
T	3	1	86.3
Coupler	4		88.5
Coupler	7		84.0
T	2	2	81.4
Coupler	5		80.6
Coupler	6		82.6

Moreover, observing results summarized in Table 4.7, the contact resistance variation of the connectors assembled with procedure No. 1 is high and instable. Conversely, the contact resistance variation for the connectors assembled with procedure No. 2 is lower and stable for both analyzed geometries.

Table 4.7. Heat cycle test. Resistance measurements of analyzed connectors before and after thermal cycles.

Connector			Connector Resistance ($\mu\Omega$)		Contact Resistance ($\mu\Omega$)		
			Before (Cycle 0)	After (Cycle 15)	Before (Cycle 0)	After (Cycle 15)	Var
Type	Item	Inst. Proc.					
T	3	1	9.14	9.84	4.22	4.96	+17.5%
Coupler	4		11.3	12.04	7.00	7.77	+11%
Coupler	7		9.40	8.78	5.10	4.51	-11.6%
Coupler	2	2	6.78	6.82	2.48	2.55	+2.8 %
Coupler	5		6.80	6.70	2.50	2.43	+2.8 %
T	6		9.60	9.45	4.68	4.57	+2.3 %

4.2.2.3 Test 3: Short-time withstand current test. Traditional procedure vs chemical cleaning.

With the aim to compare the thermal behavior of substation connectors, installed with the new and the traditional installation procedure, subjected to a short-circuit current, two short-time withstand current tests according to IEC 62271-1:2007 [29] standard were performed in the AMBER-UPC laboratory.

In the first one, the S280TLS connector was assembled with installation procedure No. 1 (with reference to Table X), whereas in the second test another sample of S285TLS connector was installed by means of procedure No. 2 with the purpose of comparing the thermal behavior of connectors assembled with the different procedures. Experimental tests were performed at atmospheric conditions (15 °C).

The experimental setup includes a 120 kVA single-phase variable autotransformer [0V- 400V] connected to a 120 kVA 400/10 V transformer whose rated output values are 0-10 V, 0-10 kA. The output of this transformer was connected to the test loop. The loop current was measured with a calibrated Fluke i6000s-Flex Rogowski coil with an uncertainty of 2%. Temperature measurements were performed with 5 T-type thermocouples placed on the second layer of strands of the tested conductor and different points of the connector. Thermocouples signals were acquired every 0.4 ms by means of an OMEGA DAQ USB-2400 acquisition card. An additional T-type thermocouple was used to measure the room temperature.

The parameters of the short-time withstand current tests are summarized in Table 4.8

Table 4.8. Parameters for short-time withstand current tests

Test	Highest current (kA_{peak})	RMS value of the ac component (kA)	Joule-integral (kA²·s)	Test duration (ms)
Short-time withstand current 1 (inst. Proc. No 1)	14.946	9.456	269.80	3017
Short-time withstand current 1 (inst. Proc. No 2)	14.803	9.679	281.92	3008

Results

Fig. 4.11 shows the temperature rise during the short time withstand current test for the T-connector S285TLS and the HTLS conductor for both installation procedures, due to the short-circuit current.

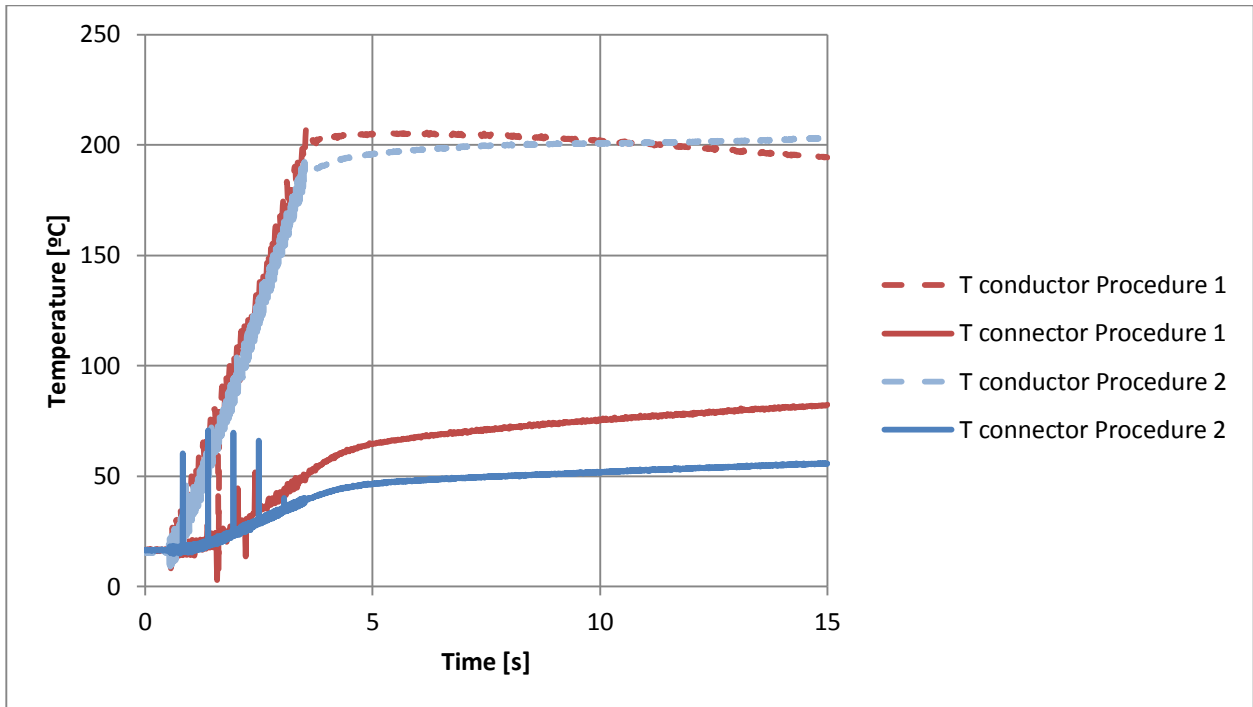


Figure 4.9. . a) Results of the experimental short time withstand current tests. In red it is shown the temperature of the connectors installed with procedure No.1, while in blue connectors assembled with procedure No. 2.

The test demonstrates a better thermal behavior of the connector installed with procedure No. 2 (chemical cleaning), providing a lower transient and steady-state temperature (of about 20°C), compared to the temperature of the connector assembled with the traditional procedure.

4.3 Determination of temperature dependence of contact resistance

With the aim to characterize the temperature dependence of the contact resistance in substation connectors, an experimental test was performed in AMBER/UPC laboratory. The contact interface between a substation connector and a conductor, assembled with procedure No. 2, was heated at 300% of nominal current of the conductor until reaching the equilibrium temperature. Then, the power transformer was switched off and disconnected from the testing loop. At this point, the contact resistance was measured continuatively during the cooling phase. The test object was a closed loop with only one connector, as shown in Fig. 4.8. The elements that composed the loop were a S330SLS connector and AAAC SALCA 593 conductor with diameter $d = 32$ mm. Four T-type thermocouples were placed on the connector' body (on the top points of AAAC conductor and in the contact interfaces between connector and conductor) to measure the temperature of the test object.

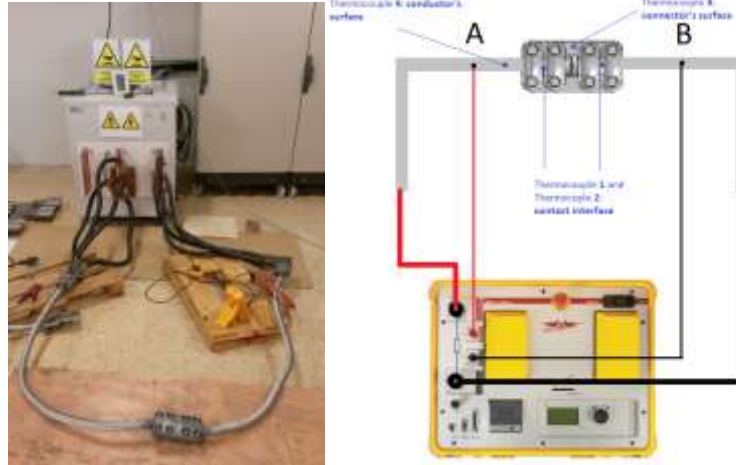


Figure 4.10. Determination of the temperature dependence of contact resistance. Heating of the testing loop. Resistance measurement with the 4-wires method and thermocouples' position.

The Kelvin or 4-wire method was employed to perform continuous resistance measurements, as shown in Fig. 5. To this end a Raytech Micro-Centurion II digital micro-ohm meter (max. current 200 A_{DC}, accuracy ±0.01μΩ) was used. Resistance measurement was performed between points A and B as shown in Fig. 4.9. Simultaneously, the associated temperature was recorded by using thermocouples.

The contact resistance is obtained by subtracting the resistance of the portion of the conductor and the resistance of the connector at the resistance measured between A and B. The theoretical resistance of the connector was calculated through electromagnetic FEM-simulation, while conductor resistance was obtained.

4.3.1 Results

The contact interface between a substation connector and a conductor, assembled with procedure No. 2, has been heated at 300% of nominal current, reaching an equilibrium temperature of 200° C. During the cooling, the resistance between points A and B, and the temperature of the test objects were measured continuously.

The contact resistance was calculated as:

$$R_c(T) = R_{A-B}(T) - R_{Conn}(T) - R_{Cond}(T) \quad (4.1)$$

where R_c is the contact resistance, R_{A-B} the resistance measured between points A and B, R_{Conn} the resistance of the connector calculated by means of FEM simulation and R_{Cond} the conductor's resistance, determined by means of experimental measurements.

Conductor's and connector's resistance are assumed to be temperature dependent:

$$R_{Cond}(T_{Cond}) = R_{0,Cond} \cdot [1 + \alpha_{Cond}(T_{Cond} - T_{0,Cond})] \quad (4.2)$$

$$R_{Conn}(T_{Conn}) = R_{0,Conn} \cdot [1 + \alpha_{Conn}(T_{Conn} - T_{0,Conn})] \quad (4.3)$$

where T_{cond} and T_{conn} are the temperature of the conductor and connector's surfaces measured by means of T-type thermocouples, R_0 the resistance at reference temperature ($T_0 = 293.15$ K) and α is the temperature coefficient.

Fig. 4.10 shows the contact resistance as function of the contact interface temperature. From the analysis of the collected data, it can be concluded that the contact resistance has an almost linear behavior between room temperature and 200 °C. Through the linear fit a temperature coefficient $\alpha = 0.0055 \text{ }^\circ\text{C}^{-1}$ was obtained. These results very are useful for simulation purposes, since they allow taking into account the dependency of the contact resistance with temperature.

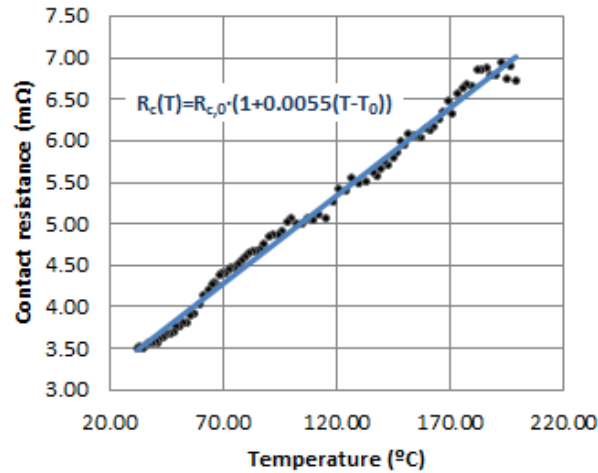


Figure 4.11. Contact resistance as a function of the contact interface temperature. Measured values and linear approximation.

4.4 GA-Optimized Fractal Model to Predict the Constriction Resistance of Substation Connectors

Since the contact interface restricts the current carrying capacity of any electrical connection [58], it is of paramount importance to develop accurate and reliable models to determine the electrical contact resistance and therefore the current density distribution across the contact interface in order to design optimized and competitive connectors and other electrical devices. The electrical contact resistance has two main components. The first term, known as electrical constriction resistance (ECR), leads to an additional resistance due to the roughness of the contacting surfaces since the electrical current has to flow through the geometric constriction. The second term, known as film resistance, is attributed to poorly conductive films or oxides formed at the contacts' interface [59]. In this work this latter term is almost removed by applying a previous chemical cleaning of the interface so that the main term of the contact resistance is the constriction resistance. The restriction resistance is greatly influenced by different variables such as the applied mechanical load, mechanical and electrical properties of the surfaces in contact or environmental conditions [60].

Early studies were pioneered by Holm [61] and Greenwood [62], who proposed analytical formulas to calculate the ECR due to round shaped clusters [59]. In the literature one can find different methods

to model the contact resistance of rough surfaces, including statistical, multiscale and fractal models [63]. Rough contact surfaces form multiple microscopic contact points which tend to form clusters defining a real contact area within the apparent or macroscopic contact area [64]. In a work based on finite simulations, Leidner et al. [58] concluded that the current distribution across the contact interface of two spherical surfaces is highly influenced by the surface roughness. They observed a steady increase of the maximum current density with increasing values of the surface roughness which was attributed to a decreasing number of contact spots.

Surface measurements have revealed that peaks and valleys profiles associated to rough surfaces show a multiscale pattern [59] with no evident smallest scale [64]. Fractal-based models are good candidates to reproduce constrictive effects taking into account such different scales [59] since most of the statistical models do not consider this phenomenon [63]. An accurate fractal description can be achieved by adequately characterizing the physics of the problem. Therefore it is expected that when increasing the number of scales, the ECR approaches a limit value even under the elastic approach in which the real contact area is assumed to be proportional to the mechanical load intensity [59]. However, when considering a limit case with infinite scales, that is, a perfect fractal surface, the true area of contact comprises an infinite number of zero size contact spots, which are subjected to an infinite contact pressure [65]. According to Kwak et al. [64] and Wilson et al. [63], at sufficient small scale, asperities experiment a plastic deformation because the mechanical load intensity exceeds the critical value, and the areas of contact tend to group into clusters. Compared to pure elastic contacts, the pressure in elastic-plastic contacts decreases at the peak points and increases at the valleys and the plastic flow flattens the surface roughness [65]. Therefore accurate ECR models must be able to reproduce this effect. The description of surface roughness with an increasing scale resolution leads to a progressive increasing number of contact points with smaller area, thus accumulating the individual contributions to the area of contact. Since they are connected in parallel, the sum of these resistances decreases, because this is a dominating effect [59]. The number of microcontact clusters determines the real contact area, their distribution being severely influenced by the small-scale surface roughness whereas their locations are determined by the large scale surface waviness. The ECR depends upon both the size and number of microcontacts and their grouping into clusters [66].

Due to its random and multiscale nature, an accurate prediction of the ECR of rough surfaces is still a challenging problem [59]. Kogut and Kompoupoulos [67] developed a model to determine the contact resistance of conductive rough surfaces, assuming a fractal geometry, elastic-plastic asperities and size-dependent micro-contacts ECR. However, fractal-based models are based on several variables whose values need to be tuned for each particular application, since they depend on the nature of the contacting surface and specifically the surface roughness. The tuning of these parameters is not a trivial task, so an automatic system to perform this operation is highly desirable.

In this thesis, a genetic algorithm (GA) approach to determine the optimal values of the parameters in the fractal model to accurately fit the measured surface roughness with that predicted by the fractal model of the rough surface, is proposed. The proposed surface roughness measurement can be done with an inexpensive surface roughness tester which is available in many industry laboratories. Therefore, from the fractal model of the rough surface a reliable and accurate prediction of the ECR can be done if the parameters such as the surface roughness, the apparent area of contact and the contact pressure are known. Although the work developed focuses on the calculation of the contact resistance

of substation connectors during the design stage, the proposed method can be applied to many other electrical devices with electrical contacts.

4.4.1 Surface Roughness Parameters

This section describes the main indexes used to characterize surface roughness according to the EN-ISO 4287 international standard [68]. The arithmetical mean roughness R_a [m] is defined as the mean or average value of the absolute roughness height $|z_i|$ along the sampling length L ,

$$R_a = \frac{1}{n} \sum_{i=1}^n |z_i| \quad (4.4)$$

n being the number of points considered within the sampling length L , and z_i the roughness height value at point i -th.

The root-mean-square roughness R_q [m] is calculated as,

$$R_q = \sqrt{\frac{1}{n} \sum_{i=1}^n z_i^2} \quad (4.5)$$

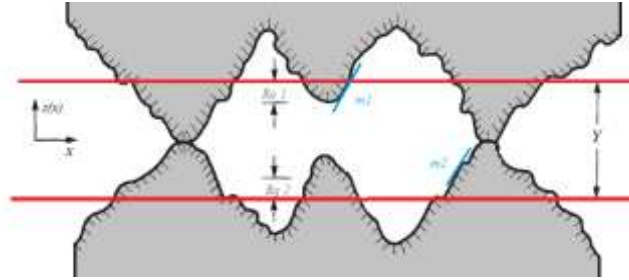


Figure 4.12. Scheme of an electrical joint with conforming surfaces in contact.

Many simple surface roughness testers assume idealized asperities exhibiting a full-wave rectified sinewave shape, thus R_q can be determined from the measurement of R_a as [69], [70],

$$R_q = 1.11 \cdot R_a \quad (4.6)$$

However, when dealing with rough surfaces with asperities exhibiting a Gaussian distribution, the relationship between R_q and R_a can be expressed as [71],

$$R_q = \sqrt{\pi/2} \cdot R_a \cong 1.25 R_a \quad (4.7)$$

As expected, the relationship between R_q and R_a depends on the distribution of the asperities, so the application of (3) and (4) can lead to inaccurate results.

Other important roughness-related parameters are the maximum height of the profile, R_y and the average maximum height of the profile, R_z , which is defined as the average of the ten greatest peak-to-valley deviations in the evaluation length.

$$R_y = R_p - R_v \quad (4.8)$$

where R_p is the maximum peak height and R_v the maximum valley depth.

The average maximum height of the profile R_z is calculated as,

$$R_z = \frac{1}{10} \sum_{i=1}^{10} R_{pi} - R_{vi} \quad (4.9)$$

where R_{pi} and R_{vi} are, respectively, the i -th highest peak, and the i -th lowest valley.

The dimensionless mean and root-mean square slopes, m_a and m_q respectively, are other parameters used to characterize the morphology of the asperities,

$$m_a = \frac{1}{n} \sum_{i=1}^n \left| \frac{dz_i}{dx} \right| \quad (4.10)$$

$$m_q = \sqrt{\frac{1}{n} \sum_{i=1}^n \left(\frac{dz_i}{dx} \right)^2} \quad (4.11)$$

The EN-ISO 4287 international standard [68] suggests calculating the derivative term in (4.10) and (4.11) as,

$$\frac{dz_i}{dx} = \frac{1}{60 \cdot \Delta x} (z_{i+3} - 9 \cdot z_{i+2} + 45 \cdot z_{i+1} - 45 \cdot z_{i-1} + 9 \cdot z_{i-2} - z_{i-3}) \quad (4.12)$$

However, an accurate measure of m_a or m_q requires complex instruments which are expensive and habitually not available. Therefore m_a is often approximated by applying different empirical correlations in the form $m_a = x \cdot (R_q)^y$, where x and y are parameters whose values change depending on the bibliographic reference considered [72]–[74].

Parameters R_q and m_a for an interface formed by two conforming rough surfaces can be calculated as [75],

$$R_{q, \text{joint}} = \sqrt{R_{q1}^2 + R_{q2}^2} \quad (4.13)$$

$$m_{a, \text{joint}} = \sqrt{m_{a1}^2 + m_{a2}^2} \quad (4.14)$$

subscripts 1 and 2 denoting both contacting surfaces.

4.4.2 The proposed GA-Optimized Fractal Model

Mathematical methods accounting for multiscale effects, such as fractal-based algorithms, can provide a detailed description of the ECR and thus accurate solutions. Fractal methods are also appealing because allow dealing with multiscale topographies since they exhibit scale invariance features, so measurements are independent of sample length and instrument resolution [67]. The fractal-based ECR theory developed by Kogut and Komvopoulos (KK) [67] assumes a fractal geometry to describe the surface topography, elastic-plastic deformation of the interfacial asperities, and size-dependent ECR of the microcontacts in the real contact area. The KK fractal model applies a fractal approach to describe the roughness of a contact interface by means of scale-invariant parameters. The three-dimensional KK surface topography is generated by means of a truncated two-variable Weierstrass-Mandelbrot function,

$$z(x, y) = L \left(\frac{G}{L} \right)^{D-2} \left(\frac{\ln \gamma}{M} \right)^{0.5} \sum_{m=1}^M \sum_{n=0}^{n_{\max}} \gamma^{(D-3)n} (\cos \varphi_{m,n} - \cos A) \quad (4.15)$$

where A can be expressed as,

$$A = \left\{ \frac{2 \cdot \pi \cdot \gamma^n (x^2 + y^2)^{0.5}}{L} \cos \left[\tan^{-1} \left(\frac{y}{x} \right) - \frac{\pi \cdot m}{M} \right] + \varphi_{m,n} \right\} \quad (4.16)$$

(x, y) being the surface points considered in the model, $z(x, y)$ the elevation coordinate of such points, L the sampling length, D ($2 < D < 3$) the fractal dimension, G the fractal roughness, $\gamma > 1$ a scaling

parameter, M the number of superposed ridges applied to generate the surface profile, n the frequency index with n_{\max} the upper limit of n , and $\varphi_{m,n}$ ($0 < \varphi_{m,n} < 2\pi$) a random phase angle. The fractal dimension D is a measure of the complexity of the fractal pattern, thus quantifying the weight of the high-frequency components.

The KK fractal model accounts for elastic-plastic deformation of the interface asperities. This model assumes that the contact between two rough surfaces can be modeled by means of a rough rigid surface in contact with a smooth elastic-plastic medium.

It is noted that in the following paragraphs some of the parameters are normalized with respect to the apparent contact area A_a , thus resulting in dimensionless parameters that are marked with an asterisk.

When $r < l$, l being the average mean free path of the electrons in the contacting materials, that is, $l = (l_1 + l_2)/2$, and r the radius of the apparent area of contact A_a , it is assumed that the electrons pass across the contact area without experiencing any scattering, so the constriction resistance is dominated by the Sharvin mechanism. Alternatively, when $r > l$, the constriction resistance is dominated by the scattering of electrons across the contact area and thus by the Holm mechanism [67].

When dealing with cast aluminum substation connectors, the radius r of the apparent area of contact A_a is of the order of micrometers ($r \sim 10^{-6}$ m), whereas the mean free path of the electrons for aluminum can vary from some tens to several hundred angstroms ($l \sim 10^{-9}$ m to $3 \cdot 10^{-8}$ m), depending on their energy level [76]. Therefore, the second condition ($r > l$) is accomplished in this case and thus the ECR is dominated by the Holm mechanism.

According to the KK formulation, the ECR based on the Holm formulation [77] is calculated as the sum of individual parallel resistances corresponding to the constriction resistances of the contact points established during the installation of the electrical connection. The dimensionless Holm electrical conductivity C_H^* is calculated as follows,

$$C_H^* = \frac{2\sqrt{2}}{\sqrt{\pi}} \left(\frac{D-1}{D-2} \right) (a'_L)^{0.5} \cdot B \quad (4.17)$$

where

$$B = \sqrt{2} \left(\frac{a'_L}{a'_S} \right)^{\frac{D-2}{2}} - (\sqrt{2}-1) \left(\frac{a'_L}{a'_C} \right)^{\frac{D-2}{2}} - 1 \quad (4.18)$$

$a'_S = a'_S/A_a$ and $a'_C = a'_C/A_a$ being, respectively, the smallest dimensionless truncated microcontact area and the critical dimensionless truncated microcontact area and A_a the apparent area of contact. They set the threshold value between elastic and fully plastic deformation areas. So, when the area of the asperities accomplishes $a' > a'_C$, the asperities experiment an elastic deformation whereas when $a' < a'_C$ they experiment a fully plastic deformation. The dimensionless critical truncated micro-contact area a'_C is defined as:

$$a'_C = \frac{a'_C}{A_a} = \frac{\left(2^{(9-2D)} \pi^{(D-2)} b^{-1} G^{(2D-4)} \left(\frac{E}{KY} \right)^2 \ln \gamma \right)^{1/(D-2)}}{A_a} \quad (4.19)$$

with $b = [0.5 \cdot \pi \cdot (0.454 + 0.41\nu_1)]^2$, ν_1 being the Poisson's ratio of the softer material in the electrical connection and E [$\text{N} \cdot \text{m}^{-2}$] the reduced elastic modulus given by,

$$E = [(1 - \nu_1^2)/E_1 + (1 - \nu_2^2)/E_2]^{-1} \quad (4.20)$$

Subscripts 1 and 2 referring respectively, to the softer and harder material, Y [N/m²] being the yield strength and $K = HB/Y$ the dimensionless ratio of the hardness to the corresponding yield strength.

The value of the largest truncated microcontact area a'_{L*} , can be found by solving the implicit equation of the dimensionless contact pressure $P^* = P/(A_0 \cdot E)$,

$$P^* = \frac{KY}{E} \left(\frac{D-1}{3-D} \right) a'_{L*} \left[\left(\frac{a'_{c*}}{a'_{L*}} \right)^{(3-D)/2} - \left(\frac{a'_{s*}}{a'_{L*}} \right)^{(3-D)/2} \right] + P \quad (4.21)$$

P [N·m⁻²] being the contact pressure and,

$$P = \left[1 - \left(\frac{a'_{c*}}{a'_{L*}} \right)^{(5-2D)/2} + 1 \right] \frac{2^{(1-2D)/2} (D-1)}{3\pi^{(4-D)/2} (5-2D)} (\ln \gamma)^{0.5} G^{*(D-2)} (a'_{L*})^{(4-D)/2} \quad (4.22)$$

It is noted that the only unknown variable in (4.21) is a'_{L*} , so it can be solved by applying a numerical method for solving equations, such as the Newton-Raphson algorithm.

4.4.2.1 KK GA-Optimized Fractal Model

The truncated two-variable Weierstrass-Mandelbrot fractal function in (4.15) includes different parameters (L , G , D , M , g and n_{max}) that must be tuned to generate a three-dimensional geometry with a surface roughness similar to that of the real contact interface. The selection of the optimal values of such parameters to accurately reproduce the real rough surface requires the application of specific optimization tools. Since parameters L , L_0 and L_s can be selected beforehand for the specific application, they are assumed as constant values during the optimization process. For consistency, it is suggested to consider values of L almost 20 times the highest value of the measured arithmetical mean roughness R_a of the two contacting interfaces. The number of ridges M to be superposed to generate the fractal surface can be determined as [78],

$$M = \text{round}(\log_{10}(L/L_0)/\log_{10}g) \quad (4.23)$$

L_0 being the smallest characteristic length which is in the order of equilibrium atomic distance, that is $L_0 \approx 0.5$ nm.

According to [67], [78], the upper limit n_{max} of the frequency index n can be calculated as,

$$n_{max} = \text{int}[\log_{10}(L/L_s)/\log g] \quad (4.24)$$

L_s being the lower cutoff corresponding to the size of individual particles [79], usually considered of about the material's interatomic distance [80].

In this paper the optimal values of the parameters G , D , M , g and n_{max} are determined by the GA algorithm. Only parameters G , D and g are changed at each iteration by applying the GA rules, since L is considered as a constant value and parameters M and n_{max} are calculated from (4.23) and (4.24), respectively. The three-dimensional surface topography is iteratively generated from (14.15) and the L , G , D , M , g and n_{max} parameters values explored by the GA algorithm. Next, at each iteration, the surface roughness parameters R_a , R_y and R_z are evaluated by applying equations (4.4), (4.8) and (4.9) for each fractal surface obtained. Then an error or objective function is evaluated by comparing the calculated values of R_a , R_y and R_z with those obtained from experimental measurements (R_{a_meas} , R_{y_meas} and R_{z_meas}). The selected objective function to be minimized by the GA algorithm is as follows,

$$\mathcal{E} = \left(1 - \frac{R_a}{R_{a_meas}} \right)^2 + \left(1 - \frac{R_y}{R_{y_meas}} \right)^2 + \left(1 - \frac{R_z}{R_{z_meas}} \right)^2 \quad (4.25)$$

Note that (4.25) evaluates the quadratic difference between the values of R_a , R_y and R_z calculated from the fractal surface generated from (4.15) and those measured by means of a surface roughness tester, that is, R_{a_meas} , R_{y_meas} and R_{z_meas} .

This iterative approach is applied until the error e is below a certain threshold value as shown in Fig. 4.13.

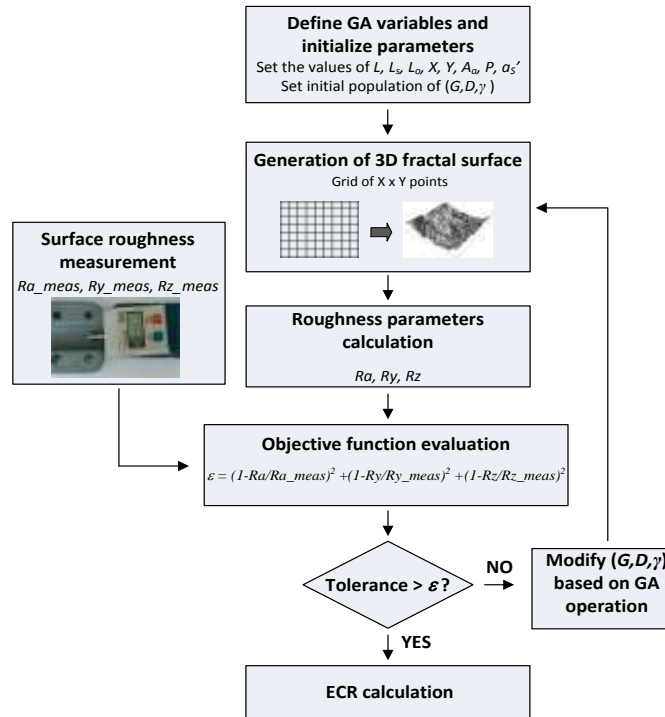


Figure 4.13. GA-based optimized fractal model of the ECR.

4.4.3 Reference ECR Models

This section develops the HG (Holm-Greenwood) and CMY (Cooper, Mikic and Yovanovich) models, which are widely applied and used as reference models for accuracy comparison purposes.

4.4.3.1 Holm-Greenwood model

Holm theory of smooth contacts [61] has pioneered ECR models. It assumes that the electrical current across rough contact surfaces flows through circular a-spots (small circular spots). According to the Holm model, the constriction of the current paths through the a-spots generates the ECR. Greenwood realized that the asperities are often grouped forming clusters [14], [81] and thus improved the Holm's model by adding an additional term to the ECR equation to account for the clusters effects. According to the HG (Holm-Greenwood) model, the ECR can be calculated as,

$$ECR = \rho \left(\frac{1}{2na} + \frac{1}{2\alpha} \right) \quad (4.26)$$

r being the electrical resistivity of the contacting surfaces, n the number of a-spots, a the radius of the

a-spots and α the cluster radius. It is noted that the first term in (26) is due to Holm whereas the second term was added by Greenwood. To calculate (4.26) it is required an accurate knowledge of parameters n , a , and α , although this information is often difficult to obtain.

However, according to [82], the ECR of a fixed area interface is independent of the number and geometrical distribution of the a-spots. This means that the first term in (26), that is, $1/(2na)$, is negligible compared to the second term, $1/2\alpha$. Therefore by only knowing the cluster radius α , it is possible to predict the ECR.

The real area of contact A_c [m²] is related to the mechanical load F [N] and the plastic flow stress H [N/m²] as,

$$A_c = F/H \quad (4.27)$$

The cluster radius α can be inferred from the real area of contact as

$$\alpha = \sqrt{A_c / \pi} \quad (4.28)$$

Finally, the ECR can be obtained as follows,

$$ECR = \frac{\rho}{2\alpha} = \sqrt{\frac{\rho^2 \pi H}{4F}} \quad (4.29)$$

Since (29) does not consider effects such as surface roughness or the apparent area of contact, its accuracy is expected to be limited. For example, when analyzing substation connectors with different geometries and, thus, different apparent contact areas, the results predicted by (4.29) will be the same, which is no realistic.

4.4.3.2 CMY Model

Cooper, Mikic and Yovanovich (CMY) developed a statistical thermal model for the contact resistance of rough surfaces [75] which was improved in later works [83]–[86]. This model can also be applied to the analysis of electrical contacts because of the close similarity between the thermal and the electric models of the contact resistance [87]. The CMY model of the ECR for conforming rough surfaces [75] assumes that asperities in the contact interface present a peaks-valleys Gaussian distribution and are randomly distributed across the apparent area of contact. The CMY model assumes isotropic rough surfaces and plastic deformation of the interfacial asperities. This model calculates the ECR [Ω] as,

$$ECR = A_a \cdot \left(1.25 \sigma_{joint} \frac{m_{joint}}{Rq_{joint}} (p_{rel})^{0.95} \right)^{-1} \quad (4.30)$$

the electrical conductivity of the joint σ_{joint} [$\Omega^{-1} \cdot m^{-1}$] being calculated as,

$$\sigma_{joint} = 2\sigma_1\sigma_2 / (\sigma_1 + \sigma_2) \quad (4.31)$$

σ_1 and σ_2 are, respectively, the electrical conductivities of the two contacting surfaces. The dimensionless relative pressure p_{rel} at the interface is calculated as [75],

$$p_{rel} = \left(P / \left[c_1 \left(1.62 \cdot \frac{R_{q,joint}}{R_{q,0}} m_{a,joint} \right)^{c_2} \right] \right)^{1/(1+0.071c_2)} \quad (4.32)$$

$m_{a,joint}$ being the average slope of the asperities in the joint, P the contact pressure [N·m⁻²], $R_{q,0} = 1 \mu m$, $H_0 = 3178$ Mpa and parameters c_1 [N·m⁻²] and c_2 (dimensionless) are calculated from the Brinell hardness H_B [N·m⁻²] of the softer material as [75],

$$c_1 = \left(4.0 - 5.77 \frac{H_B}{H_0} + 4.0 \left(\frac{H_B}{H_0} \right)^2 - 0.61 \left(\frac{H_B}{H_0} \right)^3 \right) H_0 \quad (4.33)$$

$$c_2 = 0.37 + 0.442 \frac{H_B}{c_1} \quad (4.34)$$

However, the CMY estimation of the ECR given by (30) depends on the slope $m_{a,joint}$. Although it can be measured by using three-dimensional optical profilers or laser interferometers, they are expensive and scarcely found in industrial environments, thus limiting their applicability in numerous industry applications. Another possibility is the estimation of $m_{a,joint}$ from the measured values of the surface roughness, but this estimation is often inaccurate [88] when applying the approximations found in the literature [72]–[74]. These shortcomings in the measurement or estimation of $m_{a,joint}$ limit the applicability of the CMY model.

Finally, the ECR is related to the dimensionless Holm electrical conductivity CH^* as,

$$ECR = \frac{1}{C_H} \quad (4.35)$$

where

$$C_H = \frac{C_H^* \cdot A_a^{1/2}}{\rho_1 + \rho_2} \quad (4.36)$$

Since, as indicated in Fig. 4.14, the analyzed substation connectors dealt with has two identical contact areas with the conductors the ECR must be calculated as,

$$ECR = \frac{2}{C_H} \quad (4.37)$$

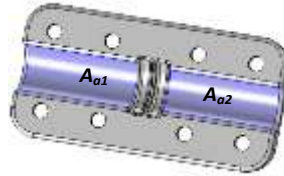


Figure 4.14. Contact interfaces ($Aa_1 = Aa_2 = Aa$) between the conductors and the substation connector.

4.4.4 Experimental

Three types of substation connectors from the catalogue of SBI Connectors and AAAC (All Aluminum Alloy Conductor) conductors (SALCA 593, 32 mm diameter) were studied. The studied substation connectors are made of A356.0 aluminum alloy with T6 heat-treatment and the AAAC conductors of 1350 Al alloy.

Table 4.9 summarizes the electrical and mechanical properties of the connectors' and conductors' material required for the different models.

Table 4.9. Aluminum properties

Variable	Description	Value	Model
ρ_1	Electrical resistivity	$5.2 \cdot 10^{-8} \Omega \cdot m$	HG-CMY-GA

	of connector's Al		
ρ_2	Electrical resistivity of conductor's Al	$2.9 \cdot 10^{-8} \Omega \cdot m$	HG-CMY-GA
Y	Yield strength of conductor's Al	73 MPa	HG- GA
H	Plastic flow stress of conductor's Al	219 MPa	HG
ν_1	Poisson's ratio of connector's Al	0.33	GA
ν_2	Poisson's ratio of conductor's Al	0.33	GA
E_1	Young modulus of connector's Al	70 GPa	GA
E_2	Young modulus of conductor's Al	70 GPa	GA
HB	Brinell hardness of conductor's material	150 MPa	CMY

Table I only provides information about Y , H and HB of the conductor material since it is the softer material in the contact.

Fig. 4.15 shows the aluminum substation connectors analyzed.

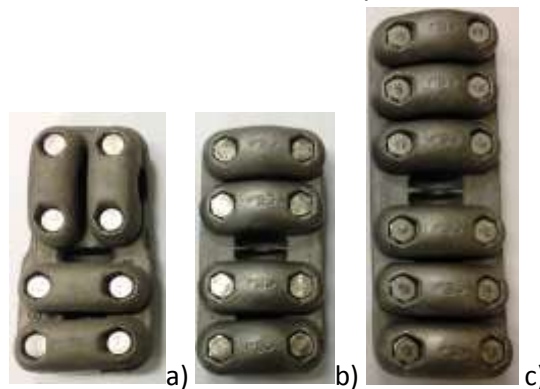


Figure 4.15. Analyzed substation connectors. a) S330TLS T-type substation connector. b) S330SLS coupler connector. c) S330SNS coupler connector.

To minimize the film resistance due to the formation of a nanometric layer of alumina and to improve substation connectors' thermal performance, a chemical solution was applied at the contacting surfaces for 45 minutes [57]. Next, the contacting surfaces were cleaned and the connectors and conductors were assembled following the standard assembly method [11]. This surface treatment provides almost complete removal the alumina film formed at the contact interface, and thus of the film component of the contact resistance.

The surface roughness of both the substation connectors and conductors dealt with was measured by using an inexpensive Mitutoyo Surftest 211 surface roughness tester, which provides fast measurements of the of R_a , R_y and R_z parameters according to the EN-ISO 4287 standard [68].



Figure 4.16. Roughness measurements performed with Mitutoyo Surftest 211 surface roughness tester on both connector's and conductor's surfaces.

The ECR of the connector-conductor system was measured by means of a digital micro-ohm meter Raytech Micro-Centurion II, which provides a maximum output current of 200 A_{DC} and a measurement accuracy of $\pm 0.01\mu\Omega$. It is based on the 4-terminal measurement technique. The ECR was measured as,

$$ECR = R_{AB} - R_{cond} - R_{conn} \quad (4.35)$$

R_{AB} being the resistance measured between points A and B (see Fig. 4), R_{cond} the resistance of the portion of the conductor between terminals A and B , and R_{conn} the resistance of the connector, which can be calculated from electromagnetic three-dimensional FEM (finite-element method) simulations. The resistance of the conductor was measured similarly, by using a conductor length of 1 m and then the result was scaled proportionally to the length of the conductor between points A and B shown in Fig. 4.17.

The axial force F at the contact interface has to be measured to determine the contact pressure P in (4.18) and (4.32) and the real area of contact A_c in (4.27). The axial force F was measured by means of the experimental torque clamp test, using the same type of stainless steel bolts and nuts required to join the connectors and conductors analyzed. After applying a suitable torque to the M10 bolts (35 N·m), which was controlled by means of a calibrated HBM TB1A torque transducer, the axial force was measured by means of a SENSOTEC D/7080-07 calibrated dynamometer.

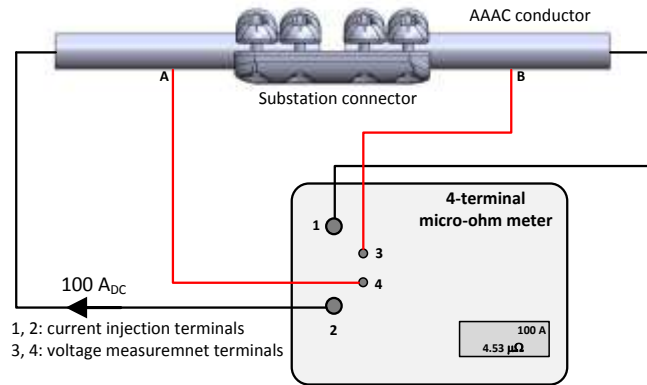


Figure 4.17. ECR measurement by using a micro-ohm meter based on the 4-terminal method.

4.4.5 Results

In this section the measurements of the ECR measurements of three aluminum substation connectors' models (S3300TLS, S3300SLS and S3300SNS shown in Fig. 4.18) are compared with the results obtained from the three different ECR models detailed in previous sections.

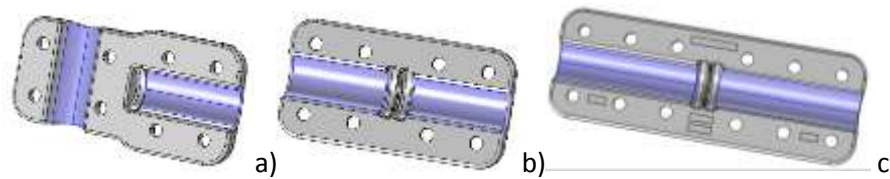


Figure 4.18. Apparent area (in blue) of contact in the three analyzed substation connectors a) S3300TLS, b) S3300SLS and c) S3300SNS.

Table 4.10 shows the parameters required to determine the ECR of the analyzed substation connectors and their values.

Table 4.10. Substation connectors' parameters

Variable	Description	Value	Model
$F_{,TLS}^1$	Contact axial force ²	4x15500 N	HG-CMY-GA
$F_{,SLS}^1$	Contact axial force ²	4x15500 N	HG-CMY-GA
$F_{,SNS}^1$	Contact axial force ²	6x15500 N	HG-CMY-GA
$A_{av,TLS}$	Apparent area of contact (S3300TLS connector)	$2 \times 29.5 \cdot 10^{-4} \text{ m}^2$	CMY-GA
$A_{av,SLS}$	Apparent area of contact (S3300SLS connector)	$2 \times 32.5 \cdot 10^{-4} \text{ m}^2$	CMY-GA
$A_{av,SNS}$	Apparent area of contact (S3300SNS connector)	$2 \times 49.5 \cdot 10^{-4} \text{ m}^2$	CMY-GA

² S3300TLS and S3300SLS connectors have four bolts in each contact interface, whereas the S3300SNS connector has six. The total axial force results from multiplying the axial force in each bolt by the number of bolts.

The apparent area of contact A_a indicated in Fig. 5, was calculated using a 3D-CAD software. For the three analyzed connectors, the two contact areas have the same size, and thus $A_{a1} = A_{a2} = A_a$.

Table III summarizes the results of the surface roughness measurements performed with the Mitutoyo SurfTest 211 surface roughness tester. It is noted that the data shown in Table 4.11 are the average results of 15 measurements done in different points of the analyzed surfaces.

Table 4.11. Surface roughness measurements.

Variable	Description	Value
Ra_{connec}	Arithmetical mean roughness of the connector's surface	4.08 mm
Ra_{cond}	Arithmetical mean roughness of the conductor's surface	0.36 mm
Ry_{connec}	Maximum roughness height of the connector's surface	30.45 mm
Rz_{connec}	Average maximum roughness height of the connector's surface	28.30 mm

Table 4.12 summarizes the parameters used to generate the three-dimensional fractal contact interfaces for each substation models analyzed. Note that the parameters the G , D , M , γ and n_{max} were obtained from the GA optimization algorithm by applying the method detailed in Fig. 4.13.

Table 4.12. Parameters used in the GA-fractal model.

Variable	Description	S3300TLS	S3300SLS	S3300SNS
		connector	connector	connector
G	Fractal roughness	$1.0427 \cdot 10^{-7}$	$6.5789 \cdot 10^{-8}$	$4.8985 \cdot 10^{-8}$
D	Fractal dimension	2.3194	2.3084	2.3012
g	Scaling parameter	1.4030	1.4375	1.5433
M	Number of superposed ridges	36	30	45
n_{max}	Upper limit of the frequency index	27	25	21
-	Grid size	500x500	500x500	500x500
L	Sample length	0.1 mm	0.1 mm	0.1 mm
L_s	Cutoff length	10 nm	10 nm	10 nm
L_o	Smallest characteristic length	0.5 nm	0.5 nm	0.5 nm
a'_s	Smallest truncated microcontact area	$6 \cdot 4.5 \cdot 10^{-10}$ m	$6 \cdot 4.5 \cdot 10^{-10}$ m	$6 \cdot 4.5 \cdot 10^{-10}$ m

The smallest truncated microcontact area a'_s shown in Table 4.12 was estimated as six times the lattice dimension of the contacting material [89].

Fig. 4.17 shows the three-dimensional fractal surfaces of the contact interfaces obtained by applying (12) with $L = 0.1$ mm, $L_s = 10$ nm and a grid size of 500x500 points.

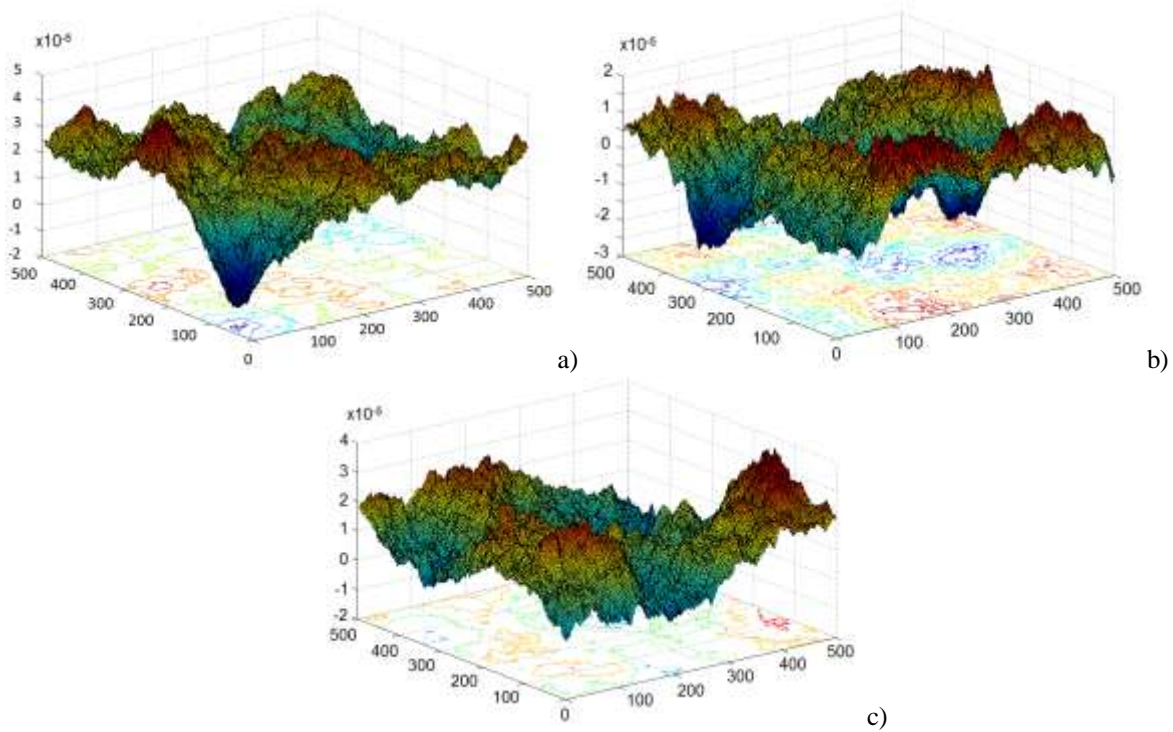


Figure 4.19. Plot of the three-dimensional fractal surface [m] of a 100 μ m x100 μ m square section (0.01 mm² with a resolution of 500x500 points) of the contact interface of the substation connectors analyzed. a) S330TLS. b) S330SLS. c) S330SNS.

Table 4.13 summarizes the measured ECR values and those obtained with the GA-optimized fractal model proposed in this paper and the reference HG and CMY models.

Table 4.13. ECR Results. Comparison Between Measured and Predicted Values Of The ECR From The Different Models Analyzed.

Substation connector	Measured values	GA-fractal Model	HG Model	CMY Model*
S330TLS	5.55 $\mu\Omega$	5.54 $\mu\Omega$	4.26 $\mu\Omega$	3.57–7.67 $\mu\Omega$
Difference		0.1%	23.2%	26.4–38.1%
S330SLS	5.26 $\mu\Omega$	5.89 $\mu\Omega$	4.26 $\mu\Omega$	3.56–7.65 $\mu\Omega$
Difference		11.9%	19.0%	26.0–45.4%
S330SNS	6.69 $\mu\Omega$	6.53 $\mu\Omega$	3.48 $\mu\Omega$	2.37–5.10 $\mu\Omega$
Difference		2.3%	47.9%	23.7–64.5%

* R_q calculated from (3) and (4) and m_a from [17] and [19]

To account for the inherent deviations among different samples, the measured ECR values displayed in Table V are the average values of five units of each substation connector model. According to the results summarized in Table V, the proposed GA-optimized fractal ECR model is the one providing better results when compared to measured data, although the predictions made by both the HG and CMY models are of the same order of magnitude than measurements.

5. Electromagnetic-thermal model for high-capacity substation connectors

This chapter performs an state of the art of the main ampacity models presented in the technical literature and a discussion about the applicability of these methods to HTLS conductors.

Ampacity models for HTLS conductors have been analyzed with the aim to have available, fast and accurate electromagnetic-thermal models for conductors with which to compare the results provided by the 3D-FEM simulation, during the development of simulation tools that will be described in sections 5.4 and 5.5.

The state of the art of electromagnetic and thermal modeling of electric devices will be also briefly summarized in chapter 0.

After that, the Multiphysics electromagnetic-thermal model developed to simulate the thermal behavior of substation connectors will be described and the 3D-FEM simulation tool implemented to simulate the short-time and peak withstand current and temperature rise tests will be presented.

5.1 State of the art

5.1.1 Ampacity models for conductors

Many steady-state ampacity models, based on thermal equilibrium equation of conductors, are found in the technical literature. The first ampacity model, based on thermal equilibrium equation, was given in 1958 by House and Truttel [90]. It was followed by Morgan contribution in 1982 [91], and by the more recent models developed by CIGRE [92] and IEEE [93] in 1992 and 2007, respectively. Nowadays, these two last models are considered the most prominent works about steady-state ampacity calculation of conductors. However, a specific ampacity model for HTLS conductors has not been developed yet. Currently, it has been studied the applicability of the traditional models to new operating condition of new technology conductors [94].

The thermal equilibrium equation for conductors can be expressed as follows [95]:

$$Q_J + Q_M + Q_S + Q_{Cor} = Q_{Conv} + Q_R + Q_E \quad (5.1)$$

Where left terms are heating sources: Q_J is the joule heating in W/m; Q_M magnetic heating in W/m, Q_S solar heating in W/m and Q_{Cor} corona heating in W/m; right terms are cooling source: Q_{Conv} is convective cooling (W/m), Q_R , radiative cooling (W/m) and Q_E evaporative cooling (W/m).

Since corona heating and evaporative cooling can be considered negligible comparing to the other terms, eq. (5.1) can be rewritten as:

$$Q_J + Q_M + Q_S = Q_{Conv} + Q_R \quad (5.2)$$

5.1.1.1 Internal heating due to electric current

Joule heating is the phenomenon generating heating losses when an electric current passes through a material with finite electrical conductivity. Thus, electric energy is converted to heat through resistive losses in the material. In the case of alternating currents, heat gain is greater, due to the skin and magnetic effect. To take into account these phenomena, Morgan model provides correction factors, which vary depending on the number of layers of non-ferrous wire.

Also CIGRE model considers effects of alternating currents and proposes two different calculations of heating, one for non-ferrous conductors and the other for steel core conductors. For ferrous conductors CIGRE adjusts the Joule losses term by taking into account skin and magnetic effects. This additional term results in an overall reduction in the ampacity rating on ferrous conductors typically between 0-3% depending on the number of wire layers and the ampacity rating being evaluated. For non-ferrous conductors, CIGRE computes Joule heating in the same manner as the IEEE method.

The IEEE model uses AC resistance values obtained from manufacturer's data-sheet, that take into account skin and magnetic effects. Since different materials compose the HTLS conductor, the use of IEEE model to calculate internal heating appears to be the more precise [95].

5.1.1.2 Convective cooling

Convective cooling is the cooling effect from airflow around the conductor. Both CIGRE and IEEE methods evaluate forced and natural convection.

The IEEE standard presents two equations for forced convection heat loss rate. The first one is appropriated for low wind speeds, whereas the second one for high wind speeds. The larger result of these two is then used for the convective cooling term in the heat balance equation. If the wind direction influence has to be considered, IEEE multiplies the convective cooling by the wind direction factor, called K_{angle} .

The CIGRE standard introduces convective cooling by means of dimensional analysis that shows that certain non-dimensional groups of parameters are useful in convective calculation. Considering the difficulty in solving analytically the constitutive equations, in the study of convection it is almost essential the experimental analysis on physical models, supported by the dimensional analysis. In the last century, the dimensional theory has been profoundly investigated: its highest achievement is the Buckingham theorem (or pi-theorem), which states that any equation modeling a physical problem can be rearranged in terms of dimensionless ratios [96]. This method allows generalizing the experimental results by means of pure numbers, summarized in the following table, each of which is a group of some of the physical quantities affecting the convective phenomenon.

Table 5.1. Dimensionless numbers related with convective phenomena description.

Variable	Expression	Description
Reynolds number	$Re = \frac{\rho L w}{\mu}$	Represents the ratio between inertial and friction forces.
Nusselt number	$Nu = \frac{h L}{k}$	Represents the incidence of the convective mechanisms on the heat exchange. It is the ratio between the heat that is exchanged by convection between the surface and the fluid, and the heat that would exchange the same surface by conduction through a layer of fluid with zero velocity of

		thickness L .
Prandtl Number	$Nu = \frac{C_p \cdot \mu}{k}$	Represents the ratio between the availability of the fluid to carry momentum and its availability to carry heat; it depends on the nature of the medium and its physical state.
Grashof Number	$Gr = \frac{g\beta(T_w - T_\infty)L^3}{\mu^2}$	Represents the ratio between the inertia forces of buoyancy and the square of the friction forces.

ρ being (kg/m³) the air volumetric mass density, w a characteristic velocity of the fluid with respect to the object (m/s), L a characteristic linear dimension (m), μ (Pa·s) the dynamic viscosity of air, C_p (J/(kg·K)) the specific heat of air, k (W/(m·K)) its thermal conductivity, g (m/s²) is the gravity of Earth, β (1/K) the thermal expansion coefficient, T_w (K) the surface temperature and T_∞ (K) the fluid temperature far from the object's surface.

As in the IEEE standard, CIGRE standard also divides the total convection heat loss rate into two parts (forced and natural convective cooling) and in addition introduces a third part, corresponding only to low wind speeds.

IEEE uses a tabular method to determine the air viscosity, air density and thermal conductivity while CIGRE uses formulas to determine these terms. The effect of these different methods is that, at wind speeds less than 5 fps (5.49 km/h) CIGRE calculates a slightly higher value for convective cooling than IEEE does. At higher wind speeds IEEE calculates a higher value. The difference for the convective cooling term between the two methods is less than 4% for all wind speeds.

However, at different wind angles there is a greater variation between the two methods. At wind angles greater than 10 degrees, CIGRE method calculates values up to 7% higher than IEEE. At wind angle less than 10 degrees IEEE calculates a higher value. At 0 degree attack angle, IEEE calculates a convective cooling term 18% higher than CIGRE [97].

Since applicability of dimensionless equations used in CIGRE model is reduced to a maximum value of conductor's temperature of about 100 °C, the use of IEEE model to calculate also the convective cooling appears the more precise than CIGRE model [95].

5.2 Electromagnetic-thermal simulation of power devices

In order to design the power devices such as substation connectors, the current carrying capacity (or ampacity) should be determined exactly since it is limited by the maximum operating temperature. The temperature rise in the power devices is primarily due to Joule's losses although induced eddy currents also have a minor contribution. Many authors in the last years have studied this problem and proposed various methods to calculate temperature rise in power devices and, mainly, in power conductors. A brief summary of the state of the art is reported as follows.

In 2002 T. Takahashi, T. Ito, T. Okamoto and T. Imajo [98] proposed two temperature rise calculation programs for a protection pipe and cable. The program for a protection pipe is based on an equation of heat conduction and the Romberg integration algorithm. The program for power cable temperature is based on a thermal equivalent circuit and the application of a fast inversion Laplace transform

algorithm. The cable is assumed as a line heat source in a uniform medium and the transient temperature rise is calculated by the one-dimensional heat conduction equation in the cylindrical coordinates system.

Other authors proposed coupled electromagnetic-thermal model to simulate the temperature distribution of XLPE cable [99], based on the finite-element method; the temperature distributions in single phase and three phase cable with different phases arrangement were calculated without taking into account the temperature dependency of material properties, due to the quite small temperature rise of the conductor with the applied current rate.

In 2008, a work related to the temperature rise of the high voltage GIS busbar was presented [100]. The temperature rise in GIS busbar is due to Joule's losses in the conductor and the induced eddy current in the tank. Heating-loss should be exactly calculated because power losses of conductor, calculated by the magnetic field analysis, are used as the input data to predict the temperature rise for the thermal analysis. The required analysis, conducted by means of the commercial software ANSYS™, is a couple-field multiphysics problem that accounts for the interactions between three-dimensional ac harmonic magnetic and fluid fields. Considering the natural convection and the radiation from the tank to the atmosphere, the heat transfer calculation is performed using the finite-volume software CFX™.

Other authors apply similar methods to simulate the temperature rise of busbars [101], [102]. In 2002 S. W. Kim et al. proposed a coupled finite element–analytic method where the power losses of a busbar were calculated from the magnetic field analysis and were used as the input data to predict the temperature rise [103]. The authors reported the difficulty to correctly apply the heat transfer coefficient on the boundaries, because the coefficient is not a constant, but depends on temperature as well as model geometry among others. The heat transfer coefficient was calculated according to the model geometry and varying temperature and was coupled with the finite element method. The heat transfer mechanism was done by the natural convection and the radiation from the tank to the atmosphere. The authors introduced the Nusselt number proposed by Churchill and Chu [104] in order to calculate the temperature-dependent heat transfer coefficient exactly.

Finally, it should be mentioned the only journal article concerning to electromagnetic and thermal behavior of substation connectors present in technical bibliography [105]. This work deals with a 400 kV, 3000 A, 50 Hz extra-high-voltage expansion substation connector used to connect two substation busbars of 150 mm diameter each. The substation connector has four aluminum wires, which provide the conductive path between both busbars. The authors of the paper reported that tests showed an unequal current distribution through the wires, which was mainly attributed to the proximity effect. A three-dimensional finite elements method approach was applied to improve the design and evaluate the electromagnetic and thermal behavior of both the original and improved versions of the connector. The applied methodology to simulate electromagnetic thermal behavior of substation connector can be considered the started point to develop a more complex coupled model, by introducing more accurate heat transfer calculation, and resistivity dependence of temperature.

In conclusion, it can be stated that a realistic transient electromagnetic-thermal 3D-simulation method for predicting the result of heating tests in complex-shaped electrical connectors as the one developed in this thesis has not been studied and developed yet.

5.3 Electromagnetic-Thermal model for substation connectors

In this section, the electromagnetic-thermal model developed to simulate the thermal behavior of the high capacity substation connector is presented.

Joule power losses calculated in the electromagnetic analysis are the heat source used as input data of the thermal analysis, which allows predicting the temperature evolution and distribution in the considered domain.

5.3.1 Electromagnetic analysis

Since the supply frequency is 50 Hz, the quasi-static approximation applies [106] and the displacement current can be neglected [107], so Maxwell's equations become,

$$\vec{\nabla} \cdot \vec{E} = \rho_e / (\epsilon_o \cdot \epsilon_r) \quad (5.3)$$

$$\vec{\nabla} \cdot \vec{B} = 0 \quad (5.4)$$

$$\vec{\nabla} \wedge \vec{E} = -\partial \vec{B} / \partial t \quad (5.5)$$

$$\vec{\nabla} \wedge \vec{B} = \mu_o \cdot \mu_r \cdot \vec{J} \quad (5.6)$$

$\vec{\nabla} \cdot$ and $\vec{\nabla} \wedge$ being, respectively, the divergence and rotational operators, E (V/m) the electric field strength, B (T) the magnetic flux density, J (A/m²) the electric current density, and ρ_e (C/m³) the free electric charge density. The charge continuity equation is also considered,

$$\vec{\nabla} \cdot \vec{J} = -\frac{\partial \rho_e}{\partial t} \quad (5.7)$$

The Ohm's law establishes the relationship between the current density and the electric field as,

$$\vec{J} = \sigma_e \cdot \vec{E} \quad (5.8)$$

where σ_e (S/m) is the electrical conductivity.

From (5.8) the resistive or Joule power losses per unit volume (W/m³) can be calculated as,

$$P_j = \vec{J} \cdot \vec{E} \quad (5.9)$$

Since the electrical conductivity σ_e is the inverse of the resistivity ρ_e , which depends on temperature [108], [109], it can be written as,

$$\sigma_e = \frac{1}{\rho_{e,0} \cdot [1 + \alpha_e \cdot (T - T_0)]} \quad (5.10)$$

T being the actual temperature, $\rho_{e,0}$ the resistivity at $T_0 = 293.15$ K and α_e the temperature coefficient. Therefore, from (5.8) and (5.10), (5.9) results in,

$$P_j = \vec{J} \cdot \vec{J} \cdot \rho_{e,0} \cdot [1 + \alpha_e \cdot (T - T_0)] \quad (5.11)$$

Resistive losses P_j are the heat source applied in the heat conduction equation detailed below, this being the linkage between the electromagnetic and thermal equations.

5.3.2 Thermal analysis

The well-known three-dimensional heat conduction equation can be expressed as [110]:

$$\rho \cdot C_p \cdot \frac{\partial T}{\partial t} = -\vec{\nabla} \cdot \vec{q} + \vec{J} \cdot \vec{E} \quad (5.12)$$

ρ (kg/m³) being the volumetric mass density, C_p (J/(kg·K)) the specific heat capacity and \vec{q} (W/m²) the heat flux density. The term $\vec{J} \cdot \vec{E}$ (W/m³) represents the specific power due to the Joule effect, that is, the heat source as in (5.11).

The link between the temperature gradient and the heat flux density is provided by the Fourier's law of heat conduction,

$$\vec{q} = -k \cdot \vec{\nabla} T \quad (5.13)$$

k (W/(m·K)) being the thermal conductivity of the considered material. By combining (5.11), (5.12) and (5.13), the heat conduction equation results in [111],

$$\rho \cdot C_p \cdot \frac{\partial T}{\partial t} = k \cdot \nabla^2 T + \vec{J} \cdot \vec{J} \cdot \rho_{e,0} \cdot [1 + \alpha_e \cdot (T - T_0)] \quad (5.14)$$

The initial temperature condition for (5.14) is expressed as,

$$T(x, y, z, 0) = f(x, y, z) \quad (5.15)$$

where $f(x, y, z)$ is the initial ($t = 0$) temperature distribution in the considered domain.

The natural convection and radiation boundary conditions for (5.14), can be expressed as [112],

$$-\vec{n} \cdot (-k \cdot \vec{\nabla} T) = h \cdot (T_\infty - T) + \varepsilon \cdot \sigma \cdot (T_\infty^4 - T^4) \quad (5.16)$$

\vec{n} being the unit vector normal to the boundary of the analyzed domain, h (W/(m²·K)) the convection coefficient, T_∞ (K) the air temperature, T (K) the surface temperature, ε the dimensionless emissivity coefficient and σ (W/(m²·K⁴)) the Stefan–Boltzmann constant. To calculate the surface-to-ambient radiation it is assumed that the ambient behaves as a black body at temperature T_∞ .

5.3.3 Heat transfer coefficients

In this thesis it is assumed that the cooling effect contribution is due to the thermal radiation and natural convection although forced convection is also possible but not applied during the experimental tests carried out. The heat transfer due to convection is often based on coefficients obtained empirically since it is a complex phenomenon and depends upon several variables comprising surface dimensions and shape, flow regime, fluid temperature and properties like density, specific heat, thermal conductivity or kinematic viscosity among others [113], [114]. Diverse heat transfer correlations for isothermal surfaces of the most usual geometries are found in the bibliography [115], [116]. Since the surfaces of the conductor and connector are not isothermal during the thermal evolution, this paper deals with heat transfer coefficients that change with temperature, so during simulations they are reevaluated at each time step.

Correlations for horizontal cylinders

A great number of correlations for natural convection from horizontal cylinders is available in the technical literature. Different correlations have been considered and compared to model the convective heat transfer on conductor's surfaces and cylindrical parts of connectors. These correlations have been

chosen considering the limits of applicability of the different formulas, including the nominal diameter of the cylinder D , the ratio between the length and the nominal diameter L/D or the Rayleigh number among others.

Table 5.2 summarizes the final conductor temperature in steady state condition, estimated by applying the analyzed correlations, whereas Fig. 5.1 shows and compares the estimated temperature vs the time, when using the different correlations, and the experimental measurements.

Table 5.2. Final conductor temperature in steady state condition, calculated by applying the different analyzed correlations.

Correlation	Reference	Nusselt Number	Predicted Equilibrium Temperature (°C)	Experimental Equilibrium Temperature (°C)
Churchill and Chu	[104]	$Nu_D^{1/2} = 0.60 + 0.387 \left(\frac{Gr_D Pr}{[1 + (0.559/Pr)^9]^{16/9}} \right)^{1/6}$	227.54	226.6
Kuehn and Goldstein	[117]	$Nu_D = 2 / \ln(A)$ $A = 1 + \frac{2}{\left[\left(0.518 Ra_D^{1/4} [1 + (0.559/Pr)^{3/5}]^{-5/12} \right)^{1/15} + (0.1 Ra_D^{1/8})^{1/15} \right]^{15}}$	231.58	226.6
Ayrton and Kilgour	[118]	$Nu_D = 1.61 (Gr_D Pr)^{0.141}$	211.20	226.6
Wamsler	[119]	$Nu_D = 0.480 (Gr_D Pr)^{0.25}$	215.03	226.6
Fand et al.	[120]	$Nu_D = 0.474 Ra_D^{0.25} Pr^{0.047}$	218.15	226.6

where Ra is the dimensionless Rayleigh number, which depends on the characteristic length L_c (m) and Pr is the dimensionless Prandtl number defined below. Note that for the surface of the conductors and the barrels of the connector L_c is the diameter of the cylinder D and for the flat surface of the connector L_c corresponds to the ratio between the surface area and the perimeter.

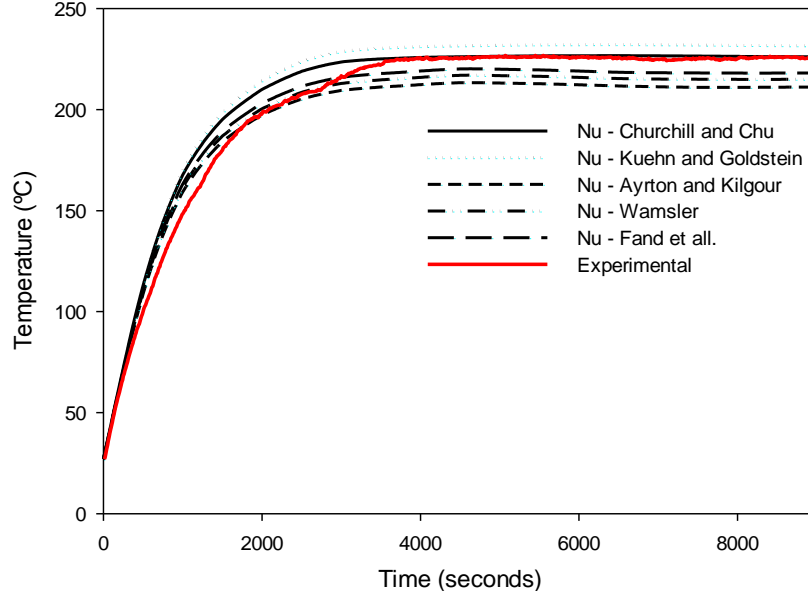


Figure 5.1. Estimated ACSS conductor temperature using different analyzed correlations (in black) and experimental measurements (in red).

As shown in Table 5.2 and Figure 5.1, the correlation which better fits with experimental data are Churchill and Chu's [104] and Kuehn and Goldstein's [117] formulas. Therefore, these correlations have been considered and implemented in the heat transfer model presented in the manuscript.

Correlations for flat surfaces

The Nusselt numbers of McAdams [121] have been applied for the remaining surfaces, since they have been modelled as flat surfaces with downward and upward cooling. According to McAdams, the Nusselt number for downward cooling must be calculated as,

$$Nu_{Lc} = 0.27 \cdot Ra_{Lc}^{1/4} \quad 10^5 < Ra_{Lc} < 10^{10} \quad (5.17)$$

Note that (5.17) has been used in the connectors' bottom parts (Model A: the body of the connector; Model B: palm's surfaces). The McAdams' Nusselt number for upward cooling is expressed as,

$$Nu_{Lc} = 0.54 \cdot Ra_{Lc}^{1/4} \quad 10^4 < Ra_{Lc} < 10^7 \quad (5.18)$$

which has been applied to the upper parts of the connectors (Model A: caps; Model B: palms' upper surfaces).

From the dimensionless Nusselt number, the characteristic length L_c (m) and the thermal conductivity k (W/(m·K)), the convective coefficient h can be calculated as[122],

$$h = \frac{Nu_{Lc} \cdot k}{L_c} \quad (5.19)$$

From the dimensionless Prandtl and Grashof numbers, one can calculate the Rayleigh number as,

$$Ra_{Lc} = Gr_{Lc} \cdot Pr \quad (5.20)$$

whereas the dimensionless Prandtl number is obtained as,

$$Pr = C_p \cdot \mu / k \quad (5.21)$$

the Grashof number is,

$$Gr_{Lc} = \frac{g \cdot \beta \cdot \rho^2 \cdot L_c^3 \cdot (T_w - T_\infty)}{\mu^2} \quad (5.22)$$

C_p (J/(kg·K)) being the specific heat of air, k (W/(m·K)) its thermal conductivity, μ (Pa·s) the dynamic viscosity of air, g (m/s²) is the gravity of Earth, β (1/K) the thermal expansion coefficient, ρ (kg/m³) the air volumetric mass density, T_w (K) the surface temperature and T_∞ (K) the fluid temperature far from the object's surface.

Air properties such as μ , ρ and k change with the temperature T_{film} of the air film, so they are taken from values tabulated in [123] and updated at each time step, where T_{film} is defined as [124],

$$T_{film} = \frac{T_w + T_\infty}{2} \quad (5.23)$$

Radiative heat transfer

Emissivity ε in (5.16) plays a key role in calculating the radiative heat exchange. It is known that emissivity highly depends upon the condition and aging of the radiating surface, although it is often difficult to determine. It is known that for aluminum conductors, emissivity lies in the range 0.2-0.9 [125].

5.4 3D-Finite Element Analysis of the Short-Time and Peak Withstand Current Tests in Substation Connectors

5.4.1 Introduction

The fact that the world is more electrical nowadays than few decades ago is a reality. According to data compiled by the International Energy Agency [126], the world electricity generation has almost quadrupled during the last four decades, with a steady growing tendency. Due to the fast expansion of transmission systems worldwide, power networks are becoming more complex and dense. Short-circuit currents are increasing, thus growing the risk of damage, since they can exceed the breaking capacity of the related protections [127]. Short-circuits in power systems can lead to severe faults [128], therefore it is crucial to ensure that the fault currents are below the limits of the equipment involved. The occurrence of short circuit faults develops unusual heating levels and temperatures of the components involved, since the electrical protections take some time to clear such faults currents [129].

Standard short-time withstand current tests and peak withstand current tests, commonly referred as short-circuit tests, are applied to several electrical devices, including power transformers, switchgear, controlgear and substation connectors, among others. Therefore, there is a persistent attention in these standard tests, both in constructing improved facilities to perform the demanding tests, which include

modern digital measuring systems [130], as well as in developing software tools to realistically simulate the performance of different power devices when subjected to short-circuit tests.

It is well-known that short-circuits generate thermal and electromechanical stresses [19], [20], so power systems are designed and tested to ensure that electrical and mechanical devices involved can withstand short-circuit conditions. To this end such devices are tested and certified in accordance with the short-time withstand current and peak withstand current tests, as defined by different international standards [21]–[23].

Substation connectors are required to endure a short-time withstand current of around tens kiloamps, usually within 1 s [22] to ensure adequate behavior under short-circuit conditions. However, the thermal stress generated may increase the contact resistance, thus affecting contact stability [24] and, therefore, the expected service life, due to the increase of the electrical resistance and associated power losses. Therefore, with the aim of ensuring reliable operation, connectors should not suffer from excessive overheating during short-circuit conditions [25], thus, their suitable thermal behavior must be ensured. Due to the huge current requirements in terms of required instantaneous power of these demanding short-circuit tests [26], they must be carried out in very specific and expensive laboratory facilities, in which customers often have to face long waiting times. Therefore, short-time withstand current tests are expensive, due to the laboratory facilities requirements, time-consuming due to the laborious installation of the experimental setup and destructive, since the test object is usually rejected once tested.

An attractive and cost-effective solution is to dispose of an advanced modelling tool to perform realistic simulations to determine the thermal stresses at which substation connectors are subjected during short-time withstand current and peak withstand current tests, from which and from experience, the risk of increasing the contact resistance can be estimated. Thanks to this modelling tool to assist the connectors' design process, an optimized design can be achieved, thus, satisfying the electromagnetic and thermal requirements imposed by the international standards [105] and ensuring to pass the compulsory laboratory tests imposed by the standards.

Modelling the short-time withstand current test and peak withstand current test in substation connectors results in a challenging multiphysics problem because electric, magnetic and thermal equations must be formulated and solved altogether. In this problem, the heat source is primarily due to the Joule's losses caused by the main current and the induced eddy currents, and therefore, both skin and proximity effects must be taken into account. In addition, conductive, convective and radiative phenomena must be taken into account to accurately model the thermal behavior of the connector. Several authors have attempted to develop electromagnetic and thermal coupled mathematical formulations to model the temperature rise or the temperature distribution in different power devices such as power conductors and cables, busbars, surge arresters or transformers [101]–[103], [131]–[136] among others, by means of 2D- and 3D-FEM approaches. Nevertheless, the abovementioned references do not analyze the problem under study, that is, the thermal analysis of the short-circuit test, although in [137] a transient 3D-FEM model to simulate the short-time withstand current capability of an air circuit breaker is presented. At the authors' knowledge, no attempts have been done to model the electromagnetic and thermal behavior of substation connectors during the standard short-time and peak withstand current tests, which can be a fast and valuable tool to optimally design the thermal behavior of such power devices, which can be especially useful during the design and optimization

stages [105]. In this thesis, a multiphysics 3D FEM-based model is proposed to accurately determine the thermal behavior of complex-shaped electrical connectors during the short-time withstand and peak withstand current tests, which is a novelty since it cannot be found in the technical literature. The proposed model deals with heat transfer coefficients whose values are automatically adapted to the geometry of the connector and conductors, fluid properties such as density, viscosity or thermal conductivity and surface temperatures. Furthermore, it also calculates the transient temperature distribution in both the connector and the power conductors or busbars to which the connector is linked. Finally, the results provided by the simulation tool are validated by means of experimental data. It is worth noting that, although the tool presented here has been focused to simulate the performance of power connectors, the approach carried out can also be applied to many other types of power devices.

5.4.2 The Short-Time Withstand Current And Peak Withstand Current

According to the IEC 62271-1:2007 standard [22], the rated short-time withstand current, often denoted as I_k , is the root-mean-square (RMS) value of the current, which the analyzed electrical device can withstand under specified conditions during a prescribed short time. These standards also specify the rated duration t_k of the short-circuit to be 1 s, although 0.5 s, 2 s and 3 s are also permitted for switchgear.

IEC [22], [138] also defines the rated peak withstand current, denoted as I_p , as the peak value of the first major loop (see Fig. 2) of the rated short-time withstand current which the electrical device under analysis can withstand under specified conditions. I_t must be selected according to the DC time constant ($\tau = L/R$) of the loop under test.

It is worth noting that substation connectors and other electrical devices must be designed to safely withstand their associated rated short-time and peak withstand currents, that is, without causing any mechanical damage to their components. Although the IEC-62271-1 standard does not specify any temperature limit for the short-time current withstand test, it states that the temperature of the object reached during this test must not be enough to produce significant damage and so to demonstrate its thermal capability [138], [139].

Therefore, the study of the short-time withstand current and peak withstand current tests is of great interest in low and high voltage applications, including vacuum and air circuit breakers [24], [137], [140] or transformers [130] among others, whose results are very valuable in order to optimize the design and behavior of such electrical devices [137]. The differential equation governing the making of an R - L inductive loop is given by,

$$V_o \sin(\omega t + \theta_v) = R \cdot i(t) + L \cdot \frac{di(t)}{dt} \quad (5.24)$$

Therefore, the transient short-circuit current flowing through an inductive shorted loop can be written as [137],

$$i(t) = \underbrace{-I_0 \cdot \sin(\theta_v - \varphi) \cdot e^{-\frac{R}{L}t}}_{\text{DC component term}} + I_0 \cdot \sin(\omega t + \theta_v - \varphi) \quad (5.25)$$

where $I_0 = V_o / \sqrt{R^2 + (\omega L)^2}$ and $\varphi = \text{tg}^{-1}(\omega L / R)$. From (5.25) it is deduced that by a tight control of the voltage phase angle θ_v during the making instant, the peak value of the transient short-circuit current

can be changed from I_0 to $2 \cdot I_0$. For example, when $\theta_v = \varphi$ the DC component term in (5.25) is null and thus the peak value of the current results in I_0 . Conversely, when $\theta_v = \varphi + 90^\circ$, the DC term is maximum, and the peak value of the current is $2 \cdot I_0$. Fig. 5.2 shows the short-circuit current as described by (5.25).

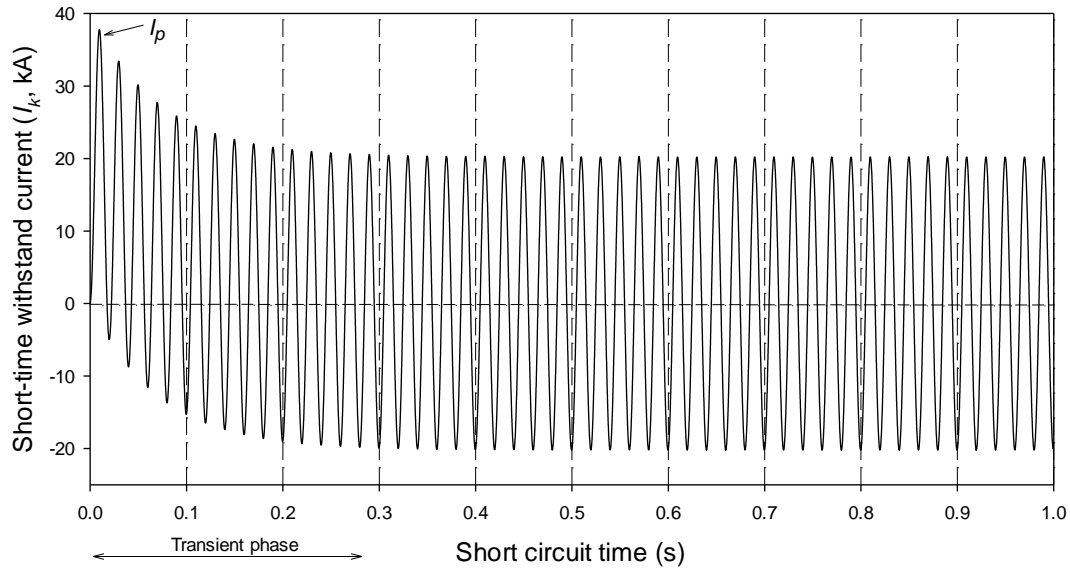


Figure 5.2. Short time withstand current (I_k) and peak withstand current (I_p).

5.4.3 The Analyzed Connectors

In this thesis, the thermal behavior of a J33SPK two-cap coupler substation connector (Model A) made of A356.0 cast aluminum alloy from the catalogue of SBI Connectors, has been analyzed by means of simulations and experimental laboratory tests. This connector is shown in Fig. 5.3a. This coupler connects two 32 mm diameter Hawthorn AAC (all aluminum conductor) conductors.

To further validate the coupled electromagnetic-thermal FEM model proposed, simulations are also conducted on a bimetallic terminal Class A for low- and medium-voltage applications, reference YAT450AM20C (Model B) from the catalogue of SBI Connectors, which is shown in Fig. 5.3b. The connector is composed of Al 99.5 % (barrel), and Cu 99.9 % (palm). It connects two 450 mm² AA-8030 AL conductors.



(a)



(b)

Figure 5.3. a) Two-cap J33SPK coupler substation connector. b) Bimetallic YAT450AM20C T connector.

The main characteristics of the analyzed connectors are summarized in Table 5.3.

Table 5.3. Analyzed connectors

Model	Connector	Conductor	Parts	Material
A	Coupler substation connector (J33SPK)	Hawthorn AAC 604.2 mm ²	AAC conductor	Aluminum
			Coupler connector	A356.0 alloy
			Bolts	Steel
B	Bimetallic terminal CLASS A (YAT450AM20C)	AA-8030 AL 450 mm ²	AA-8030 AL Conductor	Aluminum
			Terminal's barrel	Aluminum 99.5%
			Terminal's palm	Copper 99.9%

5.4.4 The 3D-FEM Model

The model proposed in this thesis is based on three-dimensional finite element modelling (3D-FEM) because it is a recognized means to simulate the electromagnetic and thermal behavior of three-dimensional objects with complex shapes [141], [142]. The problem under study has to be analyzed by applying a multiphysics approach, since it involves coupled electro-magnetic-thermal physics. To this end, the COMSOL® Multiphysics package [143] has been used.

The implemented 3D electromagnetic-thermal model is fully described in section 5.3.

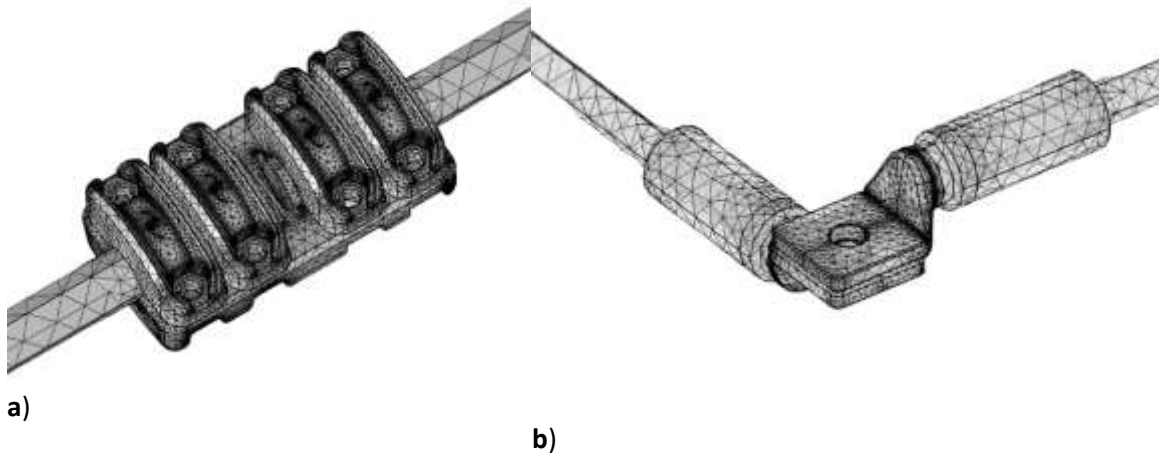


Figure 5.4. a) Model A. Mesh of the two-cap J33SPK coupler substation connector. b) Model B used to validate the 3D-FEM model proposed in this thesis. Mesh of the YAT450AM20C bimetallic compression connector

Table 5.4 summarizes the magnetic and electric parameters applied in the 3D-FEM model.

Table 5.4. Electric and magnetic parameters considered in the model

Quantity	Symbol	Unit	Value
Free-space permeability	μ_0	N/A ²	$4\pi \times 10^{-7}$
Aluminum relative permeability	$\mu_{r,Al}$	-	1
A356 alloy relative permeability	$\mu_{r,A356}$	-	1
Copper relative permeability	$\mu_{r,Cu}$	-	1
Air relative permeability	$\mu_{r,air}$	-	1

Free-space permittivity	ϵ_0	F/m	8.85×10^{-12}
Aluminum relative permittivity	$\epsilon_{r,Al}$	-	1
A356 alloy relative permittivity	$\epsilon_{r,A356}$	-	1
Copper relative permittivity	$\epsilon_{r,Cu}$	-	1
Air relative permittivity	$\epsilon_{r,air}$	-	1
Aluminum reference resistivity	ρ_{Al}	$\Omega \cdot m$	2.77×10^{-8}
A356 alloy reference resistivity	ρ_{A356}	$\Omega \cdot m$	4.44×10^{-8}
Copper reference resistivity	ρ_{Cu}	$\Omega \cdot m$	1.68×10^{-8}
Aluminum temp. coefficient	α_{Al}	1/K	0.0041
A356 alloy temp. coefficient	α_{A356}	1/K	0.0028
Copper temp. coefficient	α_{Cu}	1/K	0.0039

Table 5.5 summarizes the thermal parameters applied in the 3D-FEM model.

Table 5.5. Thermal Parameters Considered In the model

Quantity	Symbol	Units	Value
Aluminum mass density	ρ_{Al}	kg/m ³	2700
A356.0 alloy mass density	ρ_{A356}	kg/m ³	2685
Copper mass density	ρ_{Cu}	kg/m ³	8700
Aluminum specific heat capacity	$C_{p,Al}$	J/(kg·K)	900
A356.0 alloy specific heat capacity	$C_{p,A356}$	J/(kg·K)	900
Copper specific heat capacity	$C_{p,Cu}$	J/(kg·K)	385
Aluminum thermal conductivity	k_{Al}	W/(m·K)	160
A356 alloy thermal conductivity	k_{A356}	W/(m·K)	151
Copper thermal conductivity	k_{Cu}	W/(m·K)	400
Stefan–Boltzmann constant	σ	W/(m ² ·K ⁴)	$5.6704 \cdot 10^{-8}$

The Nusselt number of Kuehn and Goldstein [117] has been used for the horizontal cylindrical surfaces of the connectors and the conductors.

In addition, for model B, due to the testing loop was placed at short distance to the floor ($h_{wall} = 50$ mm), the effect of the plane on heat transfer (considered as an adiabatic wall) has been taken into account. Two-dimensional simulation of natural convection around an isothermal cylinder of diameter $d = 27$ mm, placed above an adiabatic wall, has been studied by solving the Navier-Stokes equations for conservation of momentum and the continuity equation for conservation of mass, coupled to heat transfer equations.

The results indicate the effect of weakened natural convection flow in the near-wall cylinder, causing a decline in heat transfer and, consequently, a reduced Nusselt number.

$$Nu_{near-wall} = 0.8 \cdot Nu_{unobstructed} \quad (5.26)$$

The ratio between the Nu number of the unobstructed free convection and the Nu number with the presence of the adiabatic wall has been calculated and implemented in the heat-transfer equation for model B.

Emissivity values considered in this thesis are summarized in Table 5.6.

Table 5.6. Emissivity Values Considered In the Model

Part	Emissivity
AA-8030 AL conductor [123]	0.50
AAC conductor [123]	0.50
Connectors' surfaces [144]	0.46

5.4.5 Simulation and experimental results

Simulations were carried out by using as input the experimental current acquired during the short-circuit tests conducted in two high power laboratories.

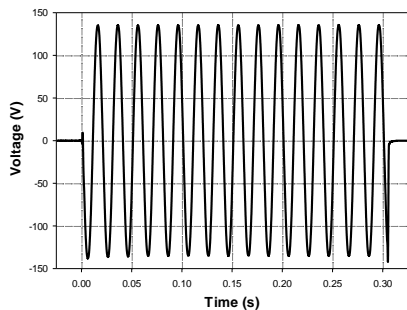
5.4.5.1 Model A. Short-time and peak withstand current tests according to the IEC-62271-1:2007 standard.

The prescribed parameters of the short-time and peak withstand current tests are summarized in Table 5.7.

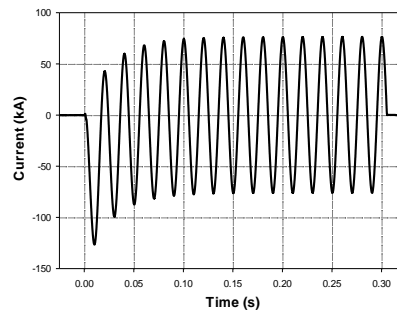
Table 5.7. Prescribed and achieved parameters for peak withstand current and short-time withstand current tests.

Test	Highest current (kA _{peak})		RMS value of the ac component (kA)	Joule-integral (kA ² ·s)		Test duration (ms)
	Prescribed	Achieved		Prescribed	Achieved	
Peak withstand current	125	126.6	55.1	-	939	307
Short-time withstand current	-	80.55	51.6	2500	2686	1009

Figs. 5.5 and 5.6 show the experimental values of the voltage and current during the peak withstand current test and the short-time withstand current test, respectively. The experimental values of the currents are used as input in the simulations.



(a)



(b)

Figure 5.5. Experimental voltage and current values during the peak withstand current test.

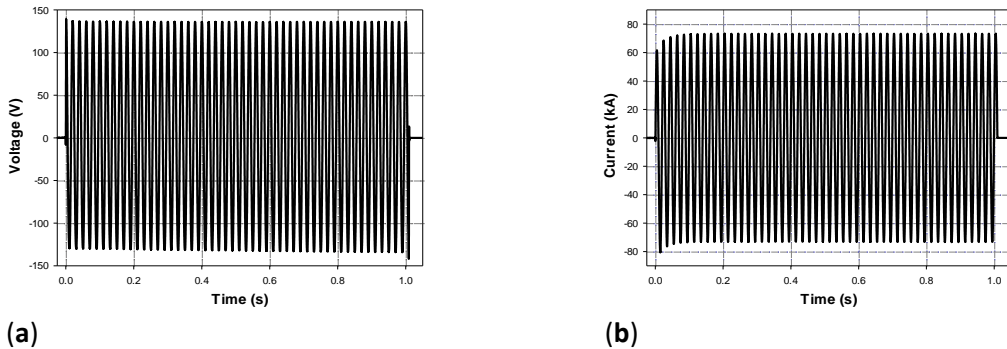


Figure 5.6. Experimental voltage and current values during the short-time withstand current test.

Figs. 5.7 show the temperature distribution at the surfaces of the connector and conductors upon completion of the peak withstand current test and the short-time withstand current test.

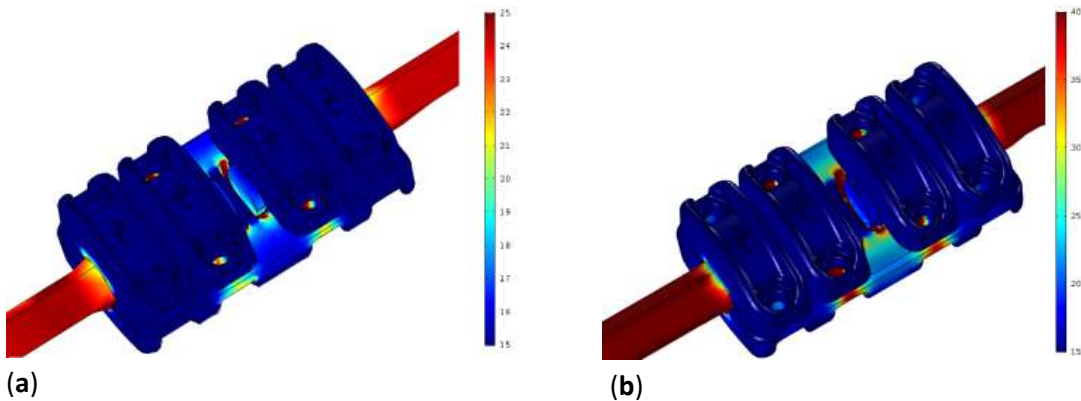
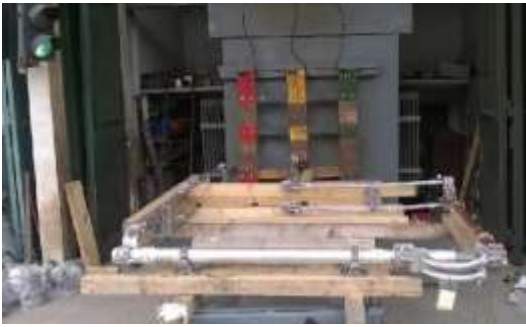


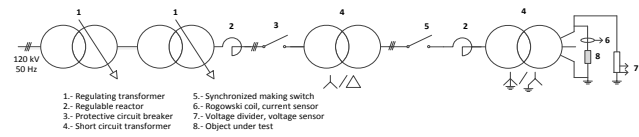
Figure 5.7. Model A. a) Simulated temperature distribution (°C) upon completion of the peak withstand current test (t = 0.3 s) according to the IEC-62271-1:2007 standard. a) Simulated temperature distribution (°C) upon completion of the short-time withstand current test.

To verify the simulation results by means of experimental data, short-time and peak withstand current tests in accordance to the IEC-62271-1:2007 standard were carried out in Veiki laboratory (Budapest, Hungary). As shown in Fig. 5.8a, test loop included two J33SPK couplers and Hawthorn AAC conductors.

The tests were carried out at atmospheric conditions (15 °C). The experimental setup includes two three-phase regulating transformers, two three-phase short-circuit transformers, two reactor sets, a protective circuit breaker and a synchronized making switch. Output current and voltage were measured with a calibrated DCM-1 Rogowski coil (uncertainty 0.59%) and a calibrated 1kV/100V R-C-R voltage divider (uncertainty 0.26%), respectively, as shown in Fig. 5.8b. Temperature measurements were performed by means of a set of calibrated K-type thermocouples placed in the connectors' bodies and the central points of each conductor. The output signals of the thermocouples were connected to an acquisition card through an analog converter. Temperature measures were registered every 100 ms.



(a)



(b)

Figure 5.8. a) Tested loop. b) Test circuit to perform the short-time withstand current test and peak withstand current test.

Fig. 5.9 shows a comparison between simulation results and the experimental peak withstand current test, until reaching thermal equilibrium. Note that the current shown in Fig. 5.5b is only applied during the first 307 ms, so afterwards there is no current flowing through the tested loop.

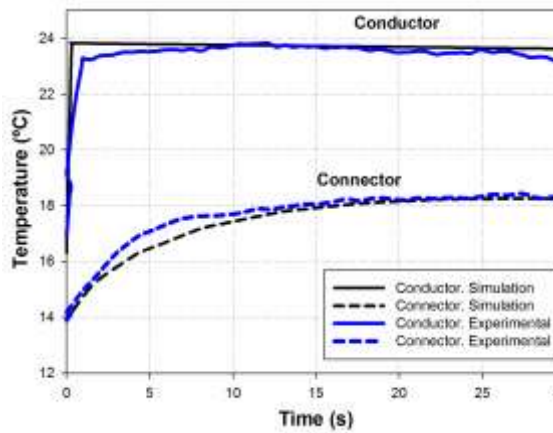


Figure 5.9. Temperature evolution during the peak withstand current test until reaching the equilibrium temperature. Bottom part of the J33SPK coupler substation connector (connector's body) and AAC conductor. Experimental versus 3D-FEM simulation results.

Fig. 5.10 shows a comparison between simulation and experimental results of the short-time withstand current test, until reaching thermal equilibrium. The current displayed in Fig. 5.6b is only applied during the first 1009 ms, after that moment there is not current flowing through the tested loop.

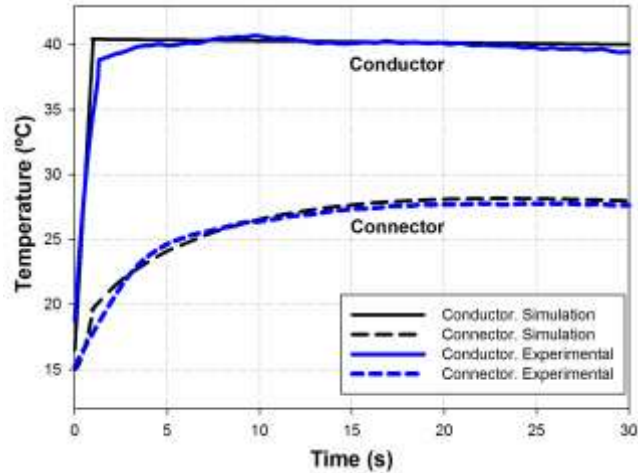


Figure 5.10. Temperature evolution during the short-time withstand current test until reaching thermal equilibrium. Bottom part of J33SPK coupler substation connector (connector’s body) and AAC conductor. Experimental versus 3D-FEM simulation results.

As shown in Figs. 5.9 and 5.10, the temperature distribution in the conductors and connectors in both transient and steady state conditions provided by the proposed simulation method shows good agreement with experimental data. Table 5.8 compares measured and simulated maximum temperatures reached during the tests. Results from Table 5.8 clearly indicate that differences between experimental and simulation results are always below 2.7%.

Table 5.8. Maximum temperature reached during the test for model a. Experimental versus simulation results.

Test	Part	T_{measured} (°C)	$T_{\text{simulated}}$ (°C)	Difference (%)
Peak withstand current test	AAC Conductor	23.9	23.8	0.4%
	J33SPK Connector	18.8	18.3	2.7%
Short-time withstand current test	AAC Conductor	40.7	40.4	0.7%
	J33SPK Connector	27.8	28.1	1.0%

5.4.5.2 Model B. Simulation of the short-circuit test according to IEC-61238-1:2003 standard

A second conductor-connector loop intended for low- and medium-voltage systems was tested in order to validate the accuracy and performance of the proposed simulation method. According to the IEC-61238-1:2003 standard [145] which regulates short-circuit tests for low- and medium-voltage connectors, the short-circuit current must raise the temperature of the reference conductors from an initial value of 35 °C or below to 250-270 °C. The duration of the short-circuit current shall be in the range [0.9, 1.05] s when applying a maximum current of 25 kA. If the required short-circuit current exceeds this value, a longer duration up to 5 s with a current level between 25 kA and 45 kA can be applied to reach the 250-270 °C. For the Model B conductor-connector configuration, these requirements are fulfilled under the conditions shown in Table 5.9.

Table 5.9. Values Achieved During The Short-Circuit Test Conducted According To The IEC-61238-1:2003 Standard.

Highest peak current (kA)	Current (kA_{RMS})	Voltage (V_{RMS})	Joule-integral ($kA^2 \cdot s$)	Test duration (ms)
57.12	36.06	158.89	2960	2275

Figs. 5.11a and 5.11b show the experimental values of the voltage and current during the short-circuit test, which are used as input in the simulations.

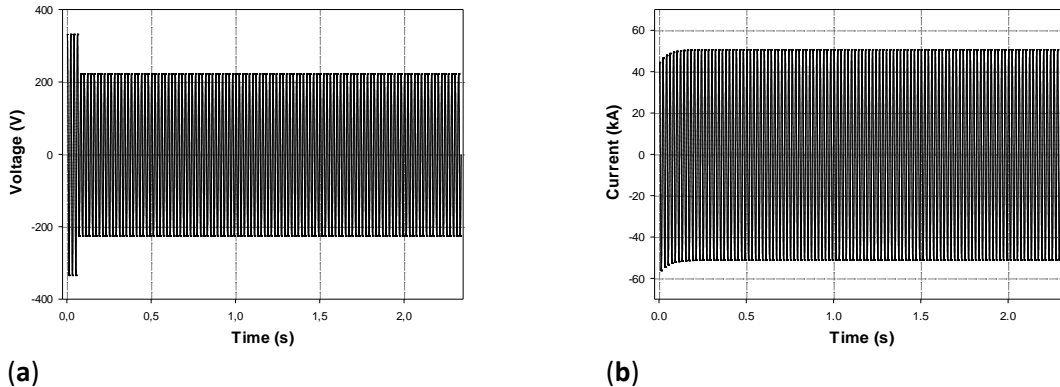


Figure 5.11. Test voltage and current measured during the short-circuit test.

Figs. 5.12a and 5.12b show the temperature distribution at the conductors' and connector's surfaces obtained.

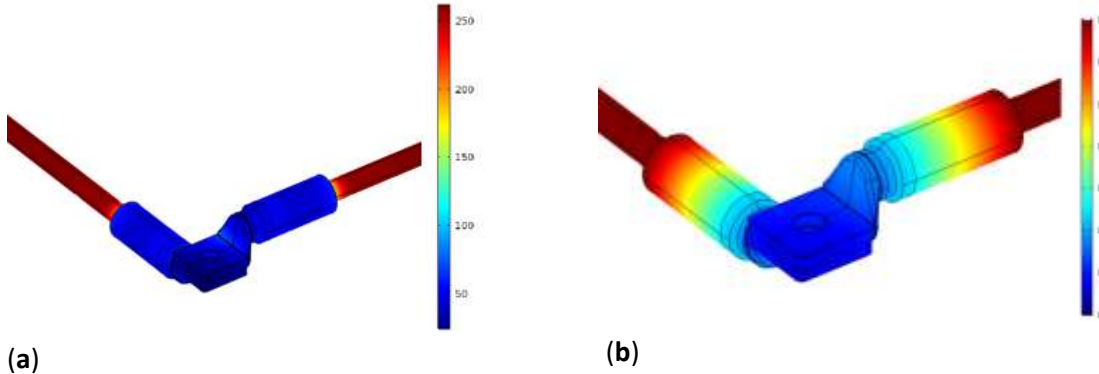


Figure 5.12. Model B. a) Simulated temperature distribution ($^{\circ}C$) upon completion of the short-circuit test ($t = 2.275$ s) according to the IEC-61238-1:2003 standard. Conductors and YAT450AM20C bimetallic compression connector. b)) Simulated temperature distribution ($^{\circ}C$) of the YAT450AM20C bimetallic compression connector at equilibrium temperature ($t = 450$ s).

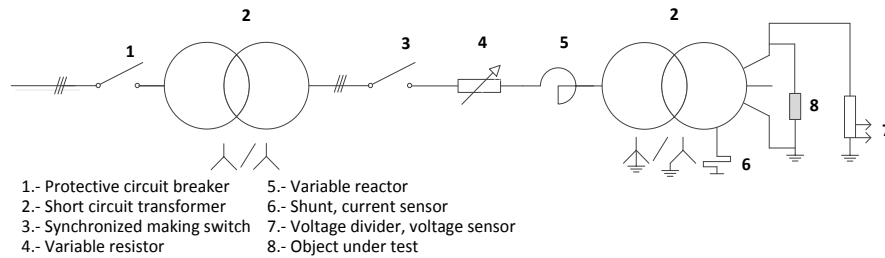
As aforementioned, with the aim to further verify the accuracy of the proposed simulation method, a bimetallic YAT450AM20C terminal for low- and medium-voltage applications was also tested according to the requirements of the IEC-61238-1:2003 standard [145]. The test was conducted in Tecnalia laboratory (Burtzeña-Barakaldo, Spain). In this case, the test object was a closed loop composed of three pairs of terminal connectors (including M20 bolt composed of A4 CL70 stainless steel) joining 450 mm^2 AA-8030 AL conductors, as shown in Fig 5.13. The experimental test was performed indoors at atmospheric conditions ($20 \text{ }^{\circ}C$). The experimental setup consists of two three-phase short-circuit

transformers, a set of variable resistors and reactors, a synchronized making switch and a protective circuit breaker. Output voltage and current were measured, respectively, with a calibrated voltage divider and a calibrated shunt, as shown in Fig. 5.13c. Temperature was recorded with an acquisition card connected to a set of thermocouples placed in the connectors' bodies and the middle points of the conductors.



(a)

(b)



(c)

Figure 5.13. a) Experimental setup. Tested loop composed of an AA-8030 AL conductor and class-A YAT450AM20C terminals. b) Bimetallic YAT450AM20C terminals. Thermocouples are placed at the barrel's surface. c) Test circuit to perform the short-circuit test.

Measured and simulated maximum temperature values are compared in Table 5.10.

Table 5.10. Maximum temperature reached during the test for Model B. Experimental versus FEM simulation results.

Part	T measured (°C)	T simulated (°C)	Difference (%)
AA-8030 AL conductor	259.6	258.8	0.3%
YAT450AM20C terminal (barrel)	84.5	85.6	1.3%

Results from Table 5.10 show that temperature differences between experimental and simulation results are lower than 1.3% for both the conductor and connector. Thus, the experimental results validate the feasibility and accuracy of the simulation method.

Fig. 5.14 compares simulation results and experimental short-circuit test results for both the AA-8030 AL conductor and YAT450AM20C terminal.

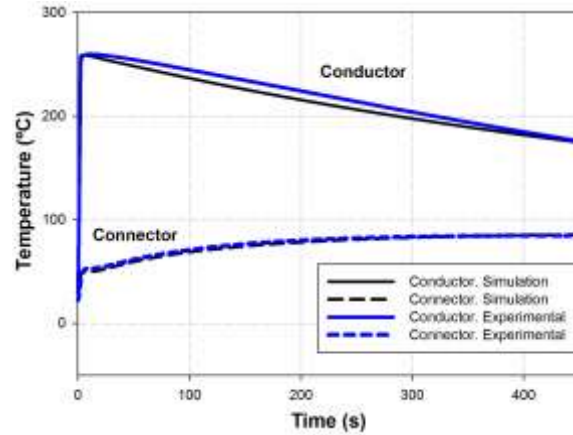


Figure 5.14. Temperature evolution during the short-circuit test according to the IEC 61238-1 standard and until reaching thermal equilibrium. Experimental versus 3D-FEM simulation results.

5.5 3D-Finite element analysis of the temperature rise test in substation connectors

5.5.1 Introduction

The new families of high-capacity substation connectors compatible with HTLS technology have to be designed to withstand, under rated operating conditions, temperatures higher than those found in the traditional application, to prevent failures that could have serious consequences on the power transmission system. Therefore, service temperature is a key design variable in high-capacity substation connectors. Moreover, before their installation, substation connectors have to be tested in accordance to the international standards. The ANSI/NEMA CC1-2009 standard [146] describes the procedures to carry out standardized temperature rise tests. The temperature rise test allows determining the substation connector's thermal behavior under both transient and steady state conditions and thus, evaluating if its size and design is compatible with the electromagnetic-thermal stress at which it is subjected during normal operational conditions. According to the ANSI/NEMA CC1-2009, the temperature rise must be performed at 100%, 125%, and 150% of the rated current, until attaining the equilibrium temperatures at each current level. The standard describes the equilibrium temperature as a constant temperature with $\pm 2^{\circ}\text{C}$ accuracy among three successive temperature measurements taken every five minutes. The rated current considered for this test must be obtained from tabulated values which establish the testing current as a function of the conductor size. The ANSI/NEMA CC1-2009 standard requires that under rated current conditions, the temperature of the tested connector does not exceed the temperature of reference conductors [146].

Temperature rise tests usually last a long time, are very power consuming and therefore, expensive. Thus, the development of a realistic simulation tool is essential for anticipating the results of the mandatory laboratory temperature rise tests in a fast way, which is especially useful during the design

and optimization phases of substation connectors [105]. Generally, the temperature rise in power devices is primarily resulting from Joule's losses due to the electrical current. In the technical bibliography, it has been developed coupled electric and thermal models to evaluate the temperature rise in power devices, including busbars, power conductors and cables [101]–[103], [131], [133], [147]–[149], although most of the references are based on 1D or 2D formulations or do not take into account radiative cooling effects. A realistic transient 3D simulation method for predicting the temperature rise in complex-shaped electrical connectors has not been studied and developed yet.

In this work a numerical method based on FEM simulations is presented to model the temperature rise in high-capacity substation connectors, although this approach is also useful to simulate the temperature rise of other types of connectors and power devices. The proposed coupled electric-thermal 3D-FEM transient analysis allows calculating the temperature distribution in both the connector and the conductors for a given test current profile.

5.5.2 The 3D-FEM model

The modeling method applied in this paper is based on coupled electric-thermal physics. Power losses calculated in the electric field analysis are used as the input data for the thermal analysis to predict the temperature rise in the analyzed geometry. The wide range of substation connectors' geometries and the need to solve coupled electric and thermal equations requires suitable calculation tools.

Complete 3D-FEM simulations together with the computation of the partial differential equations required to analyze in detail the studied phenomenon may become highly time demanding due to their computational burden when increasing the number of elements and equations to be solved simultaneously. Thus, the 3D geometric models dealt with have been prepared and simplified with the aim to reduce its complexity. Figs. 15.5 show the meshes of the analyzed domains for models I and II, respectively.

Moreover, the electromagnetic model has been simplified with the aim to reduce the computational time to solve the problem. A purely electric analysis is sufficient to accurately describe the behavior of the analyzed model.

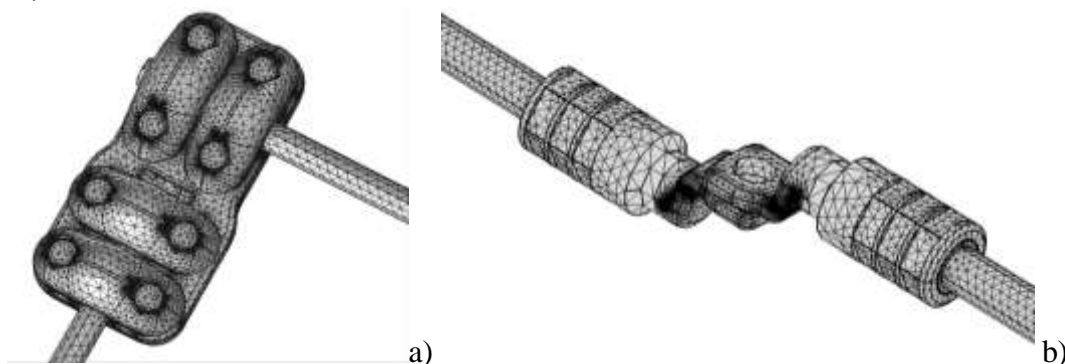


Figure 5.15. a) Model I. Mesh of the analyzed S210ZTLS high-capacity substation connector. b) Model II used to validate the simulation system proposed in this paper. Mesh of the analyzed ICAUL185 low-voltage bimetallic terminal connector.

Under the hypothesis that at the operating frequency (50 Hz) the inductive effects such as eddy currents are almost negligible, and therefore it is possible to calculate resistive power loss only by solving the electric field.

Electromagnetic analysis described in section 5.3.1 can be simplified by neglecting magnetic field calculations.

The main electric and magnetic parameters used in the 3D-FEM simulations are shown in Table 5.11.

Table 5.11. Main Electric and Magnetic Parameters

Parameter	Symbol	Units	Value
Free-space permittivity	ϵ_0	F m ⁻¹	8.85×10 ⁻¹²
Aluminum relative permittivity	$\epsilon_{r,Al}$	-	1
A356 alloy relative permittivity	$\epsilon_{r,A356}$	-	1
Steel relative permittivity	$\epsilon_{r,Fe}$	-	1
Copper relative permittivity	$\epsilon_{r,Cu}$	-	1
Air relative permittivity	$\epsilon_{r,air}$	-	1
Aluminum reference resistivity	ρ_{Al}	Ω m	2.77×10 ⁻⁸
A356 alloy reference resistivity	ρ_{A356}	Ω m	4.44×10 ⁻⁸
Steel core reference resistivity	ρ_{Fe}	Ω m	7.96×10 ⁻⁶
Steel bolts reference resistivity	ρ_{Bo}	Ω m	6.90×10 ⁻⁷
Copper reference resistivity	ρ_{Cu}	Ω m	1.68·10 ⁻⁸
Aluminum temp. coefficient	α_{Al}	K ⁻¹	0.0041
A356 alloy temp. coefficient	α_{A356}	K ⁻¹	0.004
Steel core temp. coefficient	α_{Fe}	K ⁻¹	0.0041
Copper temp. coefficient	α_{Cu}	K ⁻¹	0.0039
Contact resistance factor (substation connector) ¹	-	-	2
Contact resistance factor (bimetallic connector) ¹	-	-	0.5

¹Ratio between the contact resistance and the bulk resistance of the connector [151]

The main thermal parameters used in the 3D-FEM simulations are listed in Table 5.12.

Table 5.12. Main Thermal Parameters.

Parameter	Symbol	Units	Value
Aluminum density	ρ_{Al}	kg m ⁻³	2700
A356.0 alloy density	ρ_{A356}	kg m ⁻³	2685
Steel density	ρ_{Fe}	kg m ⁻³	7850
Copper density	ρ_{Cu}	kg m ⁻³	8700
Aluminum specific heat capacity	$C_{p,Al}$	J kg ⁻¹ K ⁻¹	900
A356.0 alloy specific heat capacity	$C_{p,A356}$	J kg ⁻¹ K ⁻¹	900

Steel specific heat capacity	$C_{p,Fe}$	$J\ kg^{-1}K^{-1}$	475
Copper specific heat capacity	$C_{p,Cu}$	$J\ kg^{-1}K^{-1}$	385
Aluminum thermal conductivity	k_{Al}	$W\ m^{-1}K^{-1}$	160
A356 alloy thermal conductivity	k_{A356}	$W\ m^{-1}K^{-1}$	151
Steel thermal conductivity	k_{Fe}	$W\ m^{-1}K^{-1}$	44.5
Copper thermal conductivity	k_{Cu}	$W\ m^{-1}K^{-1}$	400
Stefan–Boltzmann constant	σ	$W\ m^{-2}\ K^{-4}$	5.670373×10^{-8}

The Nusselt number defined by Churchill and Chu’s correlation [104] has been used in the conductors’ surfaces and cylindrical parts of the connectors, which have been modelled as horizontal cylinders,

$$Nu_{Lc} = \left\{ 0.60 + \frac{0.387 Ra_{Lc}^{1/6}}{\left[1 + \left(\frac{0.559}{Pr} \right)^{9/16} \right]^{8/27}} \right\}^2 \quad (5.32)$$

Ra_{Lc} being the Rayleigh number, with $10^{-5} < Ra_{Lc} < 10^{12}$.

Connectors’ surface emissivity values that have been considered in this analysis are summarized in Table 5.13.

Table 5.13. Emissivity values used in 3D-FEM simulation.

Part	Emissivity
1. ACSR conductors	0.45
2. AAAC conductors;	0.50
3. Connectors’ surfaces [35]	0.46
4. Steel bolts [152]	0.35

5.5.3 The analyzed high-capacity and bimetallic connectors

The main object of this analysis is a high-capacity substation T-connector prototype from SBI Connectors, which is shown in Fig. 5.16a (Model I). It connects two ACSS (Aluminum Conductor Steel Supported) LARK conductors of 20.5 mm diameter each. The connector is made of A356.0 cast aluminum alloy with T6 heat treatment.

With the aim to validate the model, the same simulation method has been applied to a low-voltage bimetallic terminal connector ICAUL185 that connects an AAAC (All Aluminum Alloy

Conductor) of 16.5 mm diameter to a terminal (Model II). The connector, shown in Fig. 5.16b is composed of Al 99.5 % (barrel), and Cu 99.9 % (palm).

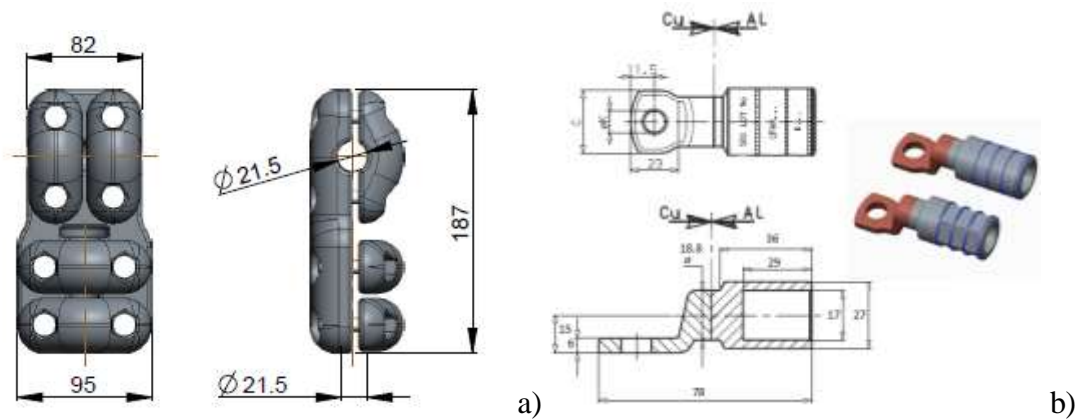


Figure 5.16. a) 2-D plot of the analyzed substation T-connector (Model I). b) 2-D plot of the analyzed bimetallic connector (Model II).

Table 5.14 summarizes the main characteristics of the analyzed connectors.

Table 5.14. Summary of the main characteristics of the analyzed connectors.

Model	Connector	Conductor	Parts	Material
Model I	Substation T-Connector	ACSS LARK d=20.5 mm	ACSS Conductor	Aluminum/Steel
			T-connector	A356.0 alloy
			Bolts	Steel
Model II	Bimetallic Connector	AAAC d=16.5 mm	ACCC Conductor	Aluminum
			Connector's Barrel	Aluminum 99.5%
			Connector's Palm	Copper 99.9%

5.5.4 Simulation and Experimental Results

5.5.4.1 Model I. Substation connectors: Temperature rise test according to the ANSI/NEMA CC1-2009 standard

When performing standard temperature rise tests, the rated current must be in accordance with the values suggested by the ANSI/NEMA CC1-2009, which depend on the conductor size. Since the analyzed connector is joined to two ACSS LARK conductors ($d = 20.5$ mm), the rated testing current must be $986 A_{rms}$.

With the aim to verify the simulation results, a temperature rise test according to the requirements of the NEMA CC1-2009 [4] was conducted in the AMBER-UPC laboratory, with Model I connectors. The test object was a closed loop circuit of three connectors, as shown in Fig. 5.17. The loop was composed of a S210ZTLST-connector, two S210ZA4P23LS terminal connectors and an ACSS LARK

conductor with diameter $d = 20.5$ mm. A torque of 35 N·m was applied to the M10 bolts of the connectors by means of a calibrated torque wrench, which allows maintaining the connection integrity and ensuring an adequate contact resistance.



Figure 5.17. Experimental test setup. a) Test loop composed of an ACSS conductor, a T-connector S210ZTLS and two terminal connectors S210ZA4P23LS. b) T-connector S210ZTLS. The five thermocouples placed in the different parts of the connector.

Experimental tests were performed at atmospheric conditions (28 °C, 982.7 hPa and 52.3% relative humidity). The experimental setup is the same described in section 4.2.2.1.

Figs. 5.18 show the temperature and time evolution of the convective coefficient h of the connector and the conductor in Model I.

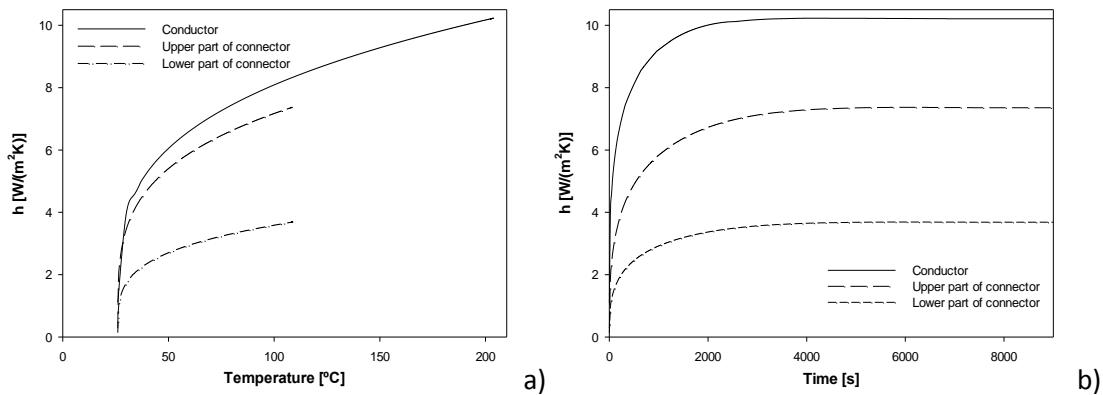


Figure 5.18. Model I. Evolution of the convective coefficients h a) with temperature and b) with time.

Figs. 5.19a and 5.19b show the temperature distribution under steady-state condition ($t = 9000$ s) on the conductors' and connector's surfaces. Fig. 5.19c compares simulation and experimental temperature-rise test results, for both the ACSS conductor and a point of the T-connector (cap 3).

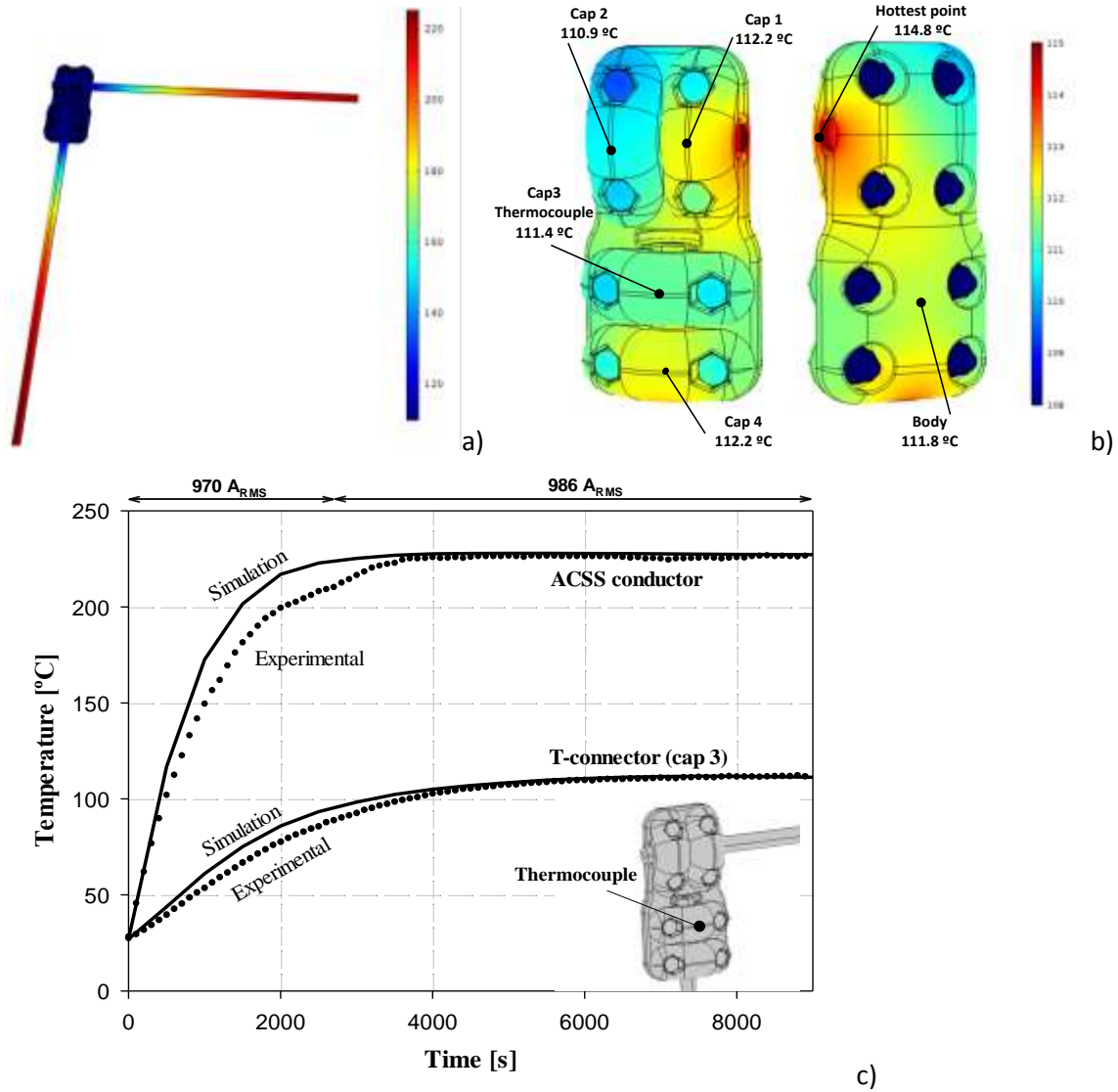


Figure 5.19. Model I. Three-dimensional plot of the simulated temperature distribution (°C) under steady-state conditions ($t = 9000$ s) when circulating a total current of $986 A_{RMS}$. a) Conductors and T-connector. b) T-connector. c) Temperature rise test according to

As shown in Fig. 5.19c, the temperature distribution in conductors and connectors in both transient and steady state conditions provided by the proposed simulation method shows a good agreement with the experimental data. It should be pointed out that the difference between experimental and simulation results during the transient part of the temperature rise test is because the simulation assumes a constant current of $986 A_{RMS}$ whereas the current delivered by the power transformer was not stable during the transient part as indicated in Fig. 5.19c.

Table 5.15 compares measured and simulated steady state temperatures for the connector and the conductors in Model I.

Table 5.15. Steady state temperature for Model I. Experimental versus FEM simulation results.

Part ¹	T measured (°C)	T simulated (°C)	Difference (%)
Conductor 1	226.6	227.5	0.4%
Conductor 2	226.8	227.6	0.3%
Cap 1	112.2	112.2	< 0.1%
Cap 2	107.5	110.9	3.1%
Cap 3	112.0	111.4	0.5%
Cap 4	115.2	112.2	2.6%
Body	111.5	111.8	0.3%
¹ See Fig. 5.19b			

Results presented in Table 5.15 show that differences between experimental and simulation results are below 3.1% in all simulated points of the geometry.

5.5.4.2 *Model II. Medium voltage connector: Current cycle test according to the ANSI C119.4 standard*

A second conductor-connector loop was tested in order to validate the accuracy and performance of the proposed simulation system.

According to the ANSI C119.4 standard, which regulates thermal cycling tests for low-voltage connectors, this test current must be adjusted to obtain a steady-state temperature increase on the control conductor surface of 100-105°C with respect to the ambient temperature [28]. For the conductor-connector dealt with in Model II, the steady-state condition is attained when applying a current of 517 A_{rms}. However, to accelerate the transient conditions, the current applied during the initial transient phase (first 1000 s) was set to 587 A_{rms}.

Whit the aim to verify the proposed simulation method, a thermal cycling test according to the requirements of the ANSI C119.4 standard [28] was conducted in AMBER-UPC laboratory, using Model II connectors.

The test object was a closed loop of five pairs of terminal connectors, joined by means of a steel bolt, as shown in Fig 5.20. The loop was composed of ten ICAUL185 terminals and an AAAC conductor with diameter d = 16.5 mm.



a)

b)

Figure 5.20. a) Experimental setup. Tested loop composed of an AAAC conductor and twelve bimetallic connectors ICAUL185. b) Bimetallic connector ICAU185. Thermocouples are placed at the barrel's surface.

The tests were performed at atmospheric conditions (20 °C). The experimental setup consisted of a single-phase transformer (10 kVA, 0-2.5 kA, 50 Hz) connected to the outer loop, which included the connectors described above. A calibrated Rogowski coil probe (Fluke i6000s Flex) was used to measure the output current provided by the transformer. To measure the temperature in steady state condition, sixteen K-type thermocouples with an AISI 316 external sheath of 1 mm diameter were placed on the terminal's barrel and on the top points of each conductor. An extra K-type thermocouple was used to measure the room temperature.

Figs. 5.21a and 5.21b show the temperature and time evolution of the convective coefficient h of the connector and the conductor in Model II.

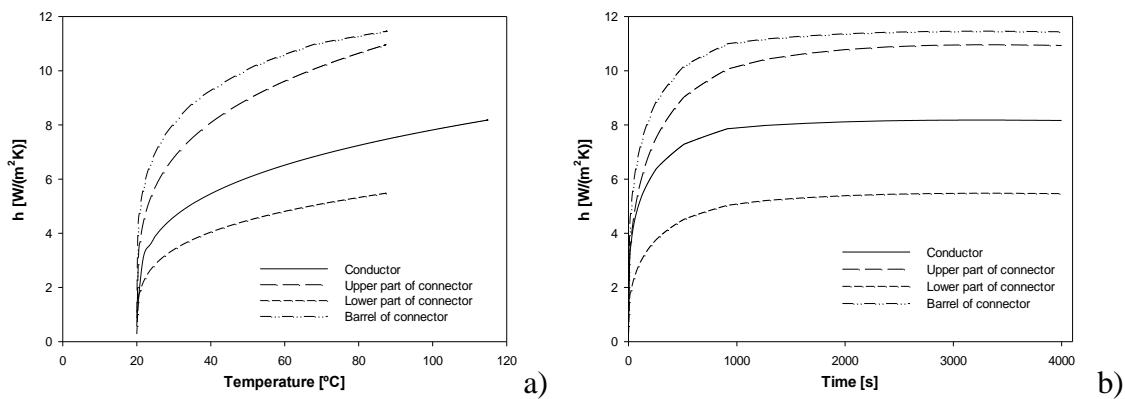
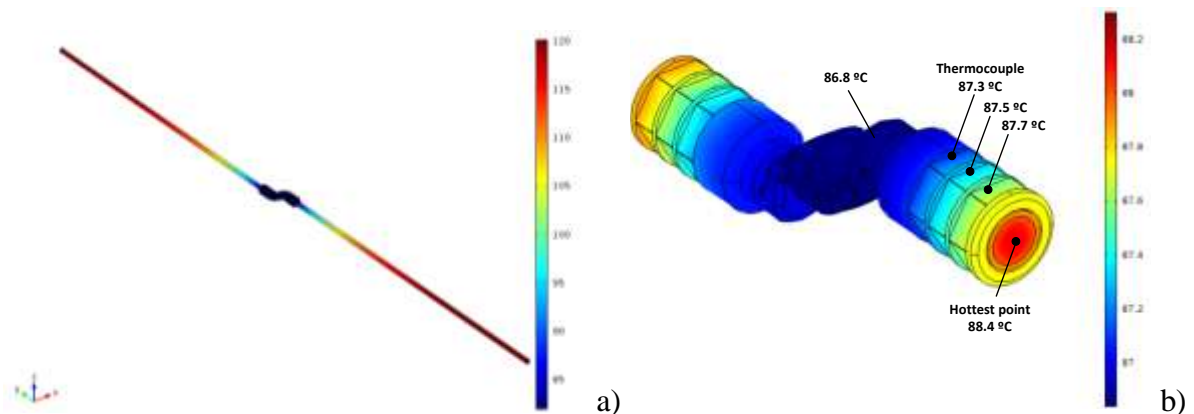


Figure 5.21. Model I. Evolution of the convective coefficients h a) with temperature and b) with time.

Figs. 5.22a and 5.22b show the temperature distribution at the conductors' and connector's surfaces obtained from FEM simulations, whereas Fig. 5.22c compares simulation results and experimental temperature rise test results for both the AAAC conductor and connector (cap 3).



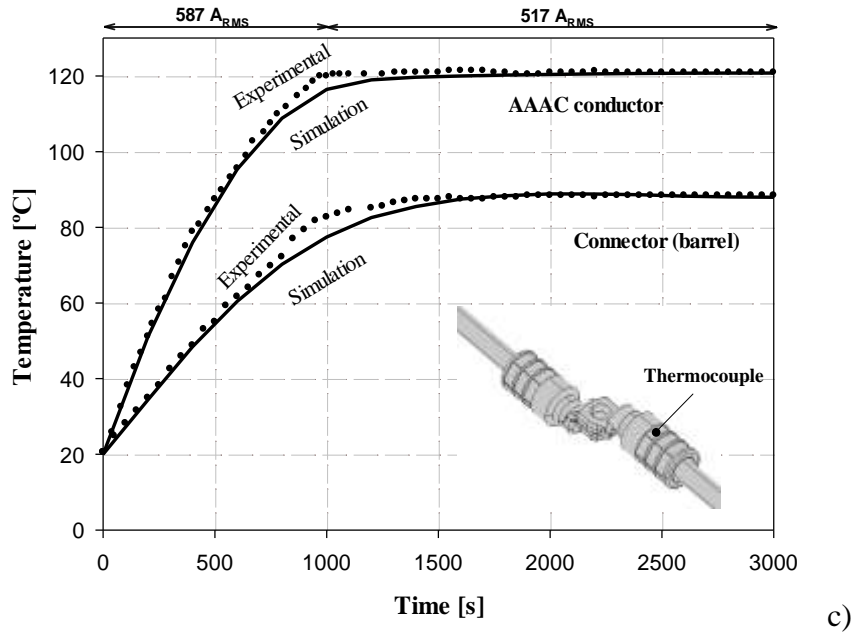


Figure 5.22. Model II. Three-dimensional plot of the simulated temperature distribution (°C) under steady-state conditions ($t = 3000$ s) when circulating a current of 517 Arms. a) Conductors and bimetallic connector. b) Bimetallic connector. c) Thermal cycling test according to ANSI C119.4. Bimetallic connector nº4 (barrel). Experimental versus FEM simulation results when circulating a current of 517 Arms.

Measured and simulated steady state temperature values are compared in Table 5.16.

Table 5.16. Steady state temperature for model ii. Experimental versus fem simulation results.

Part	T measured (°C)	T simulated (°C)	Difference (%)
Conductor 1	120.8	120.76	< 0.1%
Barrel 1	88.4	87.3	1.5%

Results from Table 5.16 show that differences between experimental and simulation are lower than 1.5% for both conductor's and connector's temperatures. Thus, the experimental results validated the feasibility and accuracy of the simulation method.

A variable time-step solver has been used to solve the problem to increase computation speed. It is noted that the elapsed time required to run a complete simulation is about 90 minutes for the T-connector S210ZTLS and about 30 minutes for the bimetallic connector ICAUL185 using an Intel Xeon CPU E5-2626 processor with 32 GB of RAM.

6. Testing and validation of High-Capacity substation connectors

In this chapter the experimental short-circuit and temperature rise tests carried out to validate the final product developed in this thesis are described.

International standards must be considered in order to evaluate substation connectors' performance. The ANSI/NEMA CC1 standard [7] provides standard test methods and performance requirements to evaluate the electrical and mechanical characteristics of substation connectors under normal operating conditions. However, this standard does not apply directly to HTLS connectors, for which there is no specific standard.

6.1 Short time and peak withstand current test

6.1.1 Requirements

According to IEC 62271-1:2007 [29] standard, depending on the capacity of the laboratory facilities where the test is to be carried out, it is possible to:

- Perform a single short-circuit where the transient (peak withstand current test) and stationary (short-time withstand current test) phase are combined.
- Perform two short-circuits, the first with the transient part of duration $t = 0.3$ s (peak withstand current test) and the second (short-time withstand current test) where the stationary short-circuit current is applied during the normal test time.

Due to the test current value chosen to validate high-capacity substation connectors, and the characteristics of the laboratory facilities, the test was performed in two stages. The current value and duration of each short-circuit are shown through Table 6.1.

Table 6.1. Prescribed and achieved Parameters for Peak Withstand Current and Short-Time Withstand Current Tests

Test	Highest current (kA _{peak})		RMS value of the ac component (kA)	Joule-integral (kA ² ·s)		Test duration (ms)
	Prescribed	Achieved		Prescribed	Achieved	
Peak withstand current	125	128.2	60.05	-	1140.8	303
Short-time withstand current	-	78.5	52.62	2500	2831.6	1009

To verify that the connector has not suffered significant damage due to the peak and short-time withstand current tests, it has to accomplish a main requirement: the connector must not have suffered visible damages. Moreover, the measured resistance of the connectors must not increase by more than 20 % after the test.

6.1.2 Test Setup

With the aim to validate the high capacity substation connector, short-time and peak withstand current tests according to the requirements of the IEC 62271-1:2007 [29] standard was conducted in the VNL-Veiki laboratory (Budapest, Hungary). The test object was a closed loop circuit of 8 connectors, as shown in Fig. 6.1. The loop was composed of four S285TLS T-connectors, four S285A4P23LS terminal connectors and a GTACSR-464 CONDOR-GREELEY conductor with diameter $d = 27.6$ mm.

The connectors have been manufactured with A356.0 Sr-modified aluminum alloy. Moreover, connectors have been assembled with the new installation procedure for high capacity substation connectors described in section 4.1 (Installation procedure No. 3 in Table 4.1). A torque of 35 N·m was applied to the M10 bolts of the connectors by means of a calibrated torque wrench, which allows maintaining the connection integrity and ensuring an adequate contact resistance.

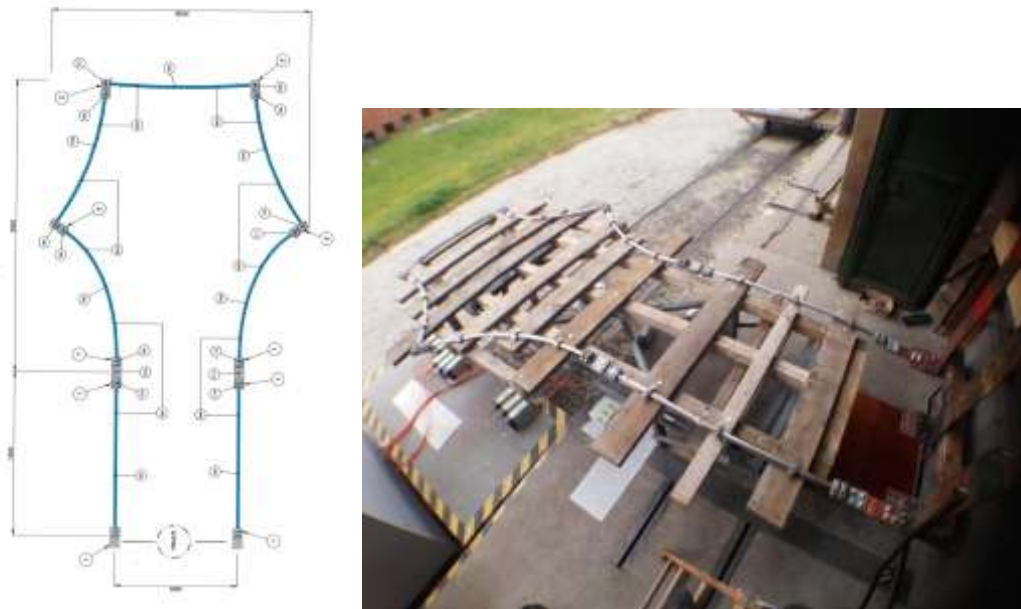


Figure 6.1. Experimental setup for Peak Withstand Current and Short-Time Withstand Current Tests

The tests were carried out at atmospheric conditions (17 °C). The experimental setup includes two three-phase regulating transformers, two three-phase short-circuit transformers, two reactor sets, a protective circuit breaker and a synchronized making switch. Output current and voltage were measured with a calibrated DCM-1 Rogowski coil (uncertainty 0.59%) and a calibrated 1kV/100V R-C-R voltage divider (uncertainty 0.26%), respectively.

Temperature measurements were performed by means of a set of calibrated K-type thermocouples placed in the connectors' bodies and the central points of each conductor. The output signals of the

thermocouples were connected to an acquisition card through an analog converter. Temperature measures were registered every 100 microseconds.

6.1.3 Results

Figs. 6.2 and 6.3 show the mean value of the temperature evolution for HTLS conductors (in blue), T285A4P23LS terminals (in red) and S285TLS (in green), for peak and short-time withstand current test, respectively.

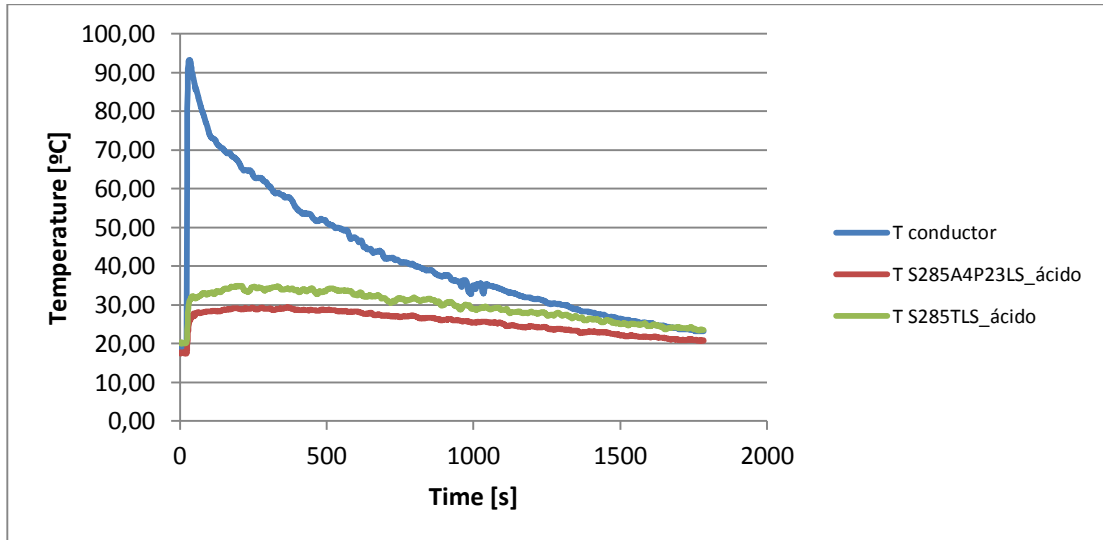


Figure 6.2. Peak withstand current test. Temperature evolution for HTLS conductors and high capacity substation connectors (mean values).

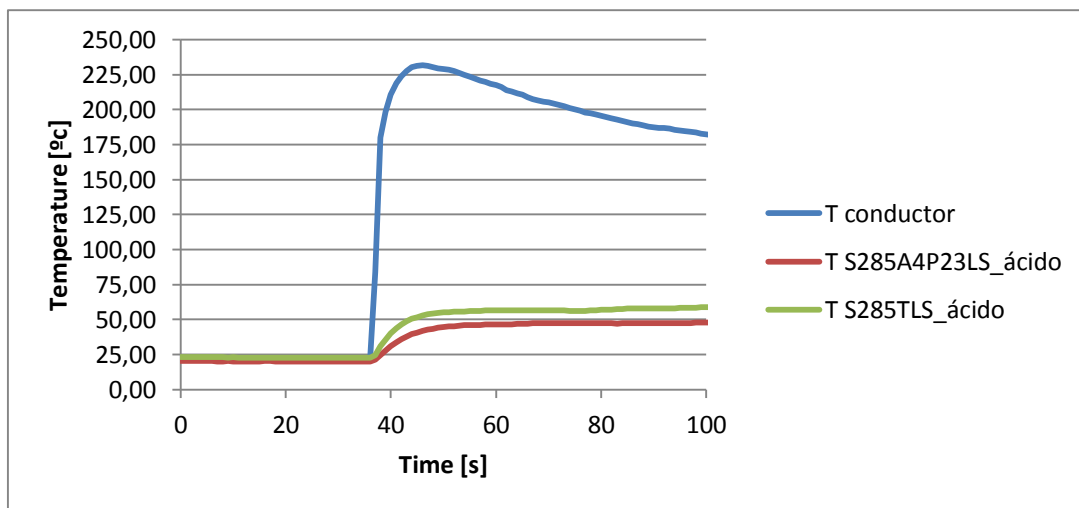


Figure 6.3. Short-time withstand current test. Temperature evolution for HTLS conductors and high capacity substation connectors (mean values).

As shown in Figs. 6.2 and 6.3, the thermal behavior of high-capacity connectors is very good, since their temperature is much lower than that reached from the cable.

Table 6.2 shows the resistance values of each connector before and after the short-time and peak withstand current test. It can be observed that the resistance variation between measurements taken before and after the test is small and that, in all cases, it decreases.

Moreover, through the visual inspection of the connectors after the test, no damage has been experienced from the high-capacity substation connectors.

Table 6.2. Measured resistance of each connector before and after the short-time and peak withstand current test.

Measuring point	Connector	R before the test (μOhm)	R after the test (μOhm)	Temperature of connector before the test ($^{\circ}\text{C}$)	Temperature of connector after the test ($^{\circ}\text{C}$)	Calculated resistance (at reference temperature 20 $^{\circ}\text{C}$)		
						R before the test (μOhm)	R after the test (μOhm)	Final/Initial value
R01	S285A4P23LS	19.29	18.41	16.50	29.50	19.56	17.74	90.66%
R02	S285TLS	13.55	11.90	17.00	30.00	13.71	11.44	83.43%
R03	S285TLS	17.12	16.03	17.70	29.50	17.28	15.44	89.38%
R04	S285TLS	14.18	14.43	17.40	29.50	14.33	13.90	97.02%
R05	S285TLS	15.02	15.03	17.00	30.20	15.20	14.44	94.99%
R06	S285A4P23LS	20.34	20.00	16.40	27.80	20.64	19.39	93.98%

Therefore, the requirements of the IEC 62271-1:2007 [29] standard are accomplished, so it can be stated that the high-capacity substation connectors are well designed to withstand an electrodynamic and thermal stress caused by short-time and peak currents. Therefore, after the test, the connection integrity and an adequate contact resistance are ensured.

6.2 Temperature rise test

6.2.1 Thermal requirements

As already explained, the temperature rise test according to the ANSI NEMA CC1- 2009 standard [4], has to be determined at 100%, 125%, and 150% of the rated current until reaching thermal equilibrium. During the first steps of the design phase of high-capacity substation connectors, a FEM simulation of temperature rise test was carried out following the specifications of NEMA-CC1 standard. It was found

that the equilibrium temperature at the third level of current (i.e. 150% of the rated current) exceeded 300 °C for the reference conductor. This temperature value is higher than twice the maximum operating temperature of the conductor and therefore, testing high capacity substation connector at this current level has no sense. In addition to the obvious deterioration of the mechanical properties of the conductor, no contact aid compound (grease) used to install connectors is able to withstand this temperature level.

Therefore, due to the lack of specific regulations for HTLS connectors, it has been suggested to perform the temperature rise test at **100%, 110% and 120%** of the nominal current for conductor.

6.2.2 Test Setup

With the aim to validate the high capacity substation connector, a temperature rise test according to the requirements of the NEMA CC1-2009 [4] was conducted in the AMBER-UPC laboratory. The test object was a closed loop circuit of three connectors, as shown in Fig. 6.4. The loop was composed of a S285TLS T-connector, two S285A4P23LS terminal connectors and a GTACSR-464 CONDOR-GREELEY conductor with diameter $d = 27.6$ mm.

The connectors have been manufactured with A356.0 Sr-modified aluminum alloy. Moreover, connectors were assembled with the new installation procedure for high capacity substation connectors described in section 4.1 (Installation procedure No. 3 in Table 4.1). A torque of 35 N·m was applied to the M10 bolts of the connectors by means of a calibrated torque wrench, which allows maintaining the connection integrity and ensuring an adequate contact resistance.



Figure 6.4. Experimental setup of the proposed temperature rise test performed to validate high-capacity substation connectors. The terminals placed at both the extremities of testing loop are making the connection with the power transformer and are not object of the test.

Table 6.3 describes the main characteristics of the conductor. The length of the conductors is such that it ensures that the temperature of one connector does not affect that of the adjacent connector or that of the conductor away from the connectors.

Table 6.3. Main characteristics of the HTLS conductor used to perform the test.

Name	Nominal diameter (mm)	Nominal section (mm ²)	Resistance @ 20°C (Ω/km)	Length (m)	Maximum operating temperature (°C)	Ampacity @ 150 °C (A)

Trefinasa GTACSR-464 CONDOR- GREELEY	27.6	464.60	0.0708	3.00	150	1275
---	------	--------	--------	------	-----	------

Experimental tests were performed indoor, at atmospheric conditions ($T_{\text{room}}=22^{\circ}\text{C}$). The experimental setup to conduct the temperature rise test is the same described in section 4.2.2.1.

Table 6.4. Three current levels settled to perform the temperature rise test.



I_1 - 100% of the nominal current (A_{rms})	I_2 - 110% of the Nominal current (A_{rms})	I_3 - 120% of the nominal current (A_{rms})
1275	1402	1530


Table 6.4 shows the three current levels settled to perform the temperature rise test, calculated according to the IEEE 738-2006 standard [93].

6.2.3 Results

From collected temperature data, an equilibrium temperature of 163.2, 198.6 and 239.8 °C were obtained for step one, two and three, respectively. Table 6.5 summarizes the mean equilibrium temperatures for the different types of tested connectors.

Table 6.5. Test results and evaluation of the condition of the high-capacity substation connectors after the test.

Part	Picture	Mean Equilibrium Temperature (°C)			Observations
		Step 1	Step 2	Step 3	
Conductor GTACSR-464 CONDOR- GREELEY		163.2	198.6	239.8	There are not significant changes in the conductor.
S285TLS connector		97.4	114.3	134.7	There are no significant changes in the connector. The contact aid compound has not reached its melting point. The connection integrity is maintained after the thermal stress.

S285A4P23LS connector		94.3	110.1	129.6	<p>There are no significant changes in the connector.</p> <p>The contact aid compound has not reached its melting point.</p> <p>The connection integrity is maintained after the thermal stress.</p>
----------------------------------	---	-------------	--------------	--------------	--

As can be observed through Table 6.5, the requirements of the ANSI/NEMA CC1 are accomplished.

All the high-capacity substation connectors pass the test because their temperature is always lower than reference conductor's temperature.

Therefore, it can be concluded that the new material and installation procedure (described in section 0) proposed for the high-capacity substation connector allow ensuring a proper electromagnetic and thermal behavior when operating at conditions imposed by HTLS conductors.

Moreover, it is important to observe that in normal operating conditions (100% of nominal current) high-capacity connectors reach the maximum temperature of 97.6 °C. This operating temperature allows ensuring that also its mechanical performance remains good and stable, as can be observed by means of the following picture (source [35]) where main mechanical properties (UTS and Yield strength) are plotted as function of temperature.

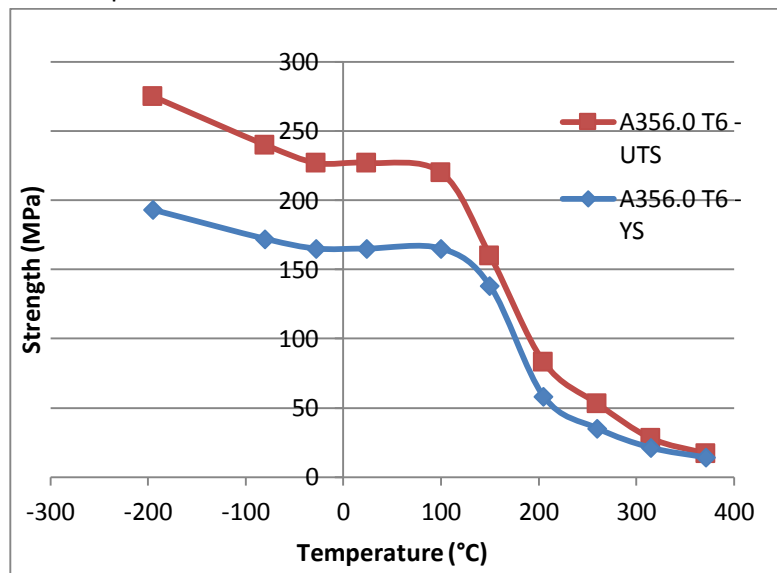


Figure 6.5. Ultimate tensile strength and Yield Strength as function of temperature for standard A356.0 Aluminum alloy.

As shown in Fig. 6.5, at 100 °C A356.0 aluminum alloy approximately maintains the same properties shown at room temperature.

In conclusion, it can be stated that high-capacity substation connector is able to maintain a good electro-magnetic, thermal and also mechanical behavior during normal operating conditions, when installed with HTLS conductors.

7. Conclusions

HTLS conductors, with an almost identical section that that of the conventional ones, allow increasing the nominal current capacity [2], with an allowable increase in operating temperature. However, the increase of power lines capacity imposes more severe operating conditions on devices such as substation connectors, involved in transmission and distribution systems, which are subjected to higher loads and have to operate at higher temperatures.

The main objective of this thesis is to contribute to the development of a new family of high-capacity substation connectors compatible with HTLS technology.

The first aspect that has been analyzed to develop the high-capacity substation connectors is the **selection of the base material**. At present, substation connectors are manufactured by using A356 cast aluminum alloy due to its good castability and physical properties. It has been explained that aluminum alloy in as-cast conditions cannot be used in high-voltage applications because it exhibits relatively poor mechanical properties and, as consequence, has to be exposed to heat or chemical treatments. **Heat treatments** are very common processes in foundry to obtain higher mechanical properties. Currently, it is a common practice to expose substation connectors to T6 heat treatment, which consists of a solution heat treatment, water quenching and artificial aging [7], before their installation.

However, due to the new operating conditions introduced by HTLS technology, A356 alloy needs to be further improved to accomplish the requirements of high-capacity substation connectors. In this thesis, a **chemical treatment**, also known as modification, which consists in the addition of small quantities of a modifier element to the melt, has been proposed. Modification allows changing the morphology of the eutectic silicon phase from flake-like to fine fibrous [8].

Chemical treatment, as abovementioned, is not currently used to manufacture substation connectors, therefore, the introduction of the chemical modification in the manufacturing process of substation connector is one of the contributions of this thesis.

With the aim to characterize the microstructure and main physical properties of the A356 Sr-modified alloy, some specimens of material have been melted in Giga Foundry (Santpedor, Barcelona) and subsequently the T4 and T6 heat treatment were applied. Moreover, some specimens have not been treated with the aim to characterize also material in as-cast condition. Strontium was chosen as modifier agent, due to the strong modifying action at low concentrations. The modification has been performed with the addition of 0.03% of Strontium.

To validate the effectiveness of the proposed chemical cleaning, main physical properties of the traditional and the improved material have been characterized in order to ensure the reliability of the high-capacity substation connectors.

Mechanical properties (ultimate tensile strength and elongation to failure) of the improved material have been evaluated through a tensile test performed with a universal tensile testing machine. From the results it can be stated that the Sr-modified alloy presents better mechanical properties than the standard alloy, especially for the thermal treatments T0 and T4.

Electrical resistivity measurements have been performed at room temperature to compare electrical properties of both un-modified and Sr-modified alloys. Results obtained show that for both alloys the T6 heat treatment is the one that allows obtaining a lower resistivity, whereas the T0 (as cast) is the one that provides a higher resistivity. Comparing the electrical resistivity values of the un-modified A356.0 alloy and the A356.0-Sr0.03 modified alloy at 20 °C, a decrease of more than 15% of the resistivity can be observed in the case of the modified alloy for the three analyzed heat treatments. For the T6 heat treatment the **decrease of electrical resistivity is of 18%**. This fact is very important as it will allow a better thermal behavior of the high-capacity substation connector.

Moreover, electrical resistivity, which is the main parameter that affects the operating temperature of the connector, has been evaluated in a wide range of temperatures, from cryogenic up to 200 °C, with the aim to find out the temperature coefficient of resistivity in the temperature range where high-capacity connector will operate.

Finally, a novel experimental method to measure **thermal conductivity** coupled with 3D-FEM thermal simulations has been proposed in this thesis to characterize thermal conductivity of un-modified and Sr-modified alloys. Obtained results show that for both alloys the T6 heat treatment is the one that allows obtaining a higher thermal conductivity. Analyzing thermal conductivity values of the un-modified A356.0 alloy and the A356.0-Sr0.03 modified alloy at room temperature, it can be observed that thermal conductivity in modified alloy slightly increases for the three analyzed heat treatments, compared with the un-modified alloy. Higher thermal conductivity will allow a better thermal behavior of the high-capacity substation connector.

The **contact resistance** is the main variable which defines the energy-efficiency, the stable performance and the long-term service of an electrical connection.

It has been explained that the contact surface preparation is essential to guarantee proper contact between connector and conductor since the contact resistance can notably degrade substation connectors' performance. Many studies demonstrated that if HTLS cables will replace traditional conductors, the installed population of connectors will age more rapidly and the number of connector failures will increase due to the increased aging effects of higher temperature and current density. Therefore, with the aim to reduce the contact resistance and, therefore, improve the thermal behavior of high capacity substation connectors, a new installation procedure has been proposed in this thesis. It consists on a **chemical cleaning** on coupling parts between conductor and connector's surfaces, before conventional installation. The chemical cleaning treatment proposed in this thesis allows a **reduction of the contact resistance** of substation connectors **of about 50%**, which allows an important improvement in the thermal performance of such device.

The thermal behavior of connectors installed with the new installation procedure has been compared with the traditional one. To this end, temperature rise, thermal cycle and short-time withstand current tests has been performed in the AMBER-UPC laboratory with connectors installed with both traditional and new installation procedure. Obtained results shows a lower operating temperature and lower degradation for connectors installed with the new installation procedure, proposed in this thesis. Moreover, the temperature coefficient of contact resistance has been determined through an experimental test.

To accurately predict the thermal behavior of high-capacity substation connectors in operating conditions imposed by HTLS conductors, it is important to be able to **estimate the electrical constriction resistance**. Different ECR models available in the technical bibliography (Holm-Greenwood, Cooper-Mikic-Yovanovich and Kogut and Komvopoulos models) have been analyzed and compared with experimental room temperature resistance measurements, to find out the most suitable model for substation connectors. The model that shows the better agreement with experimental data is the Kogut and Komvopoulos fractal model for conductive rough surfaces, which assumes fractal geometry, elastic-plastic asperities and size-dependent micro-contacts ECR to estimate ECR. However, fractal models are based on several parameters dependent on the nature of the contacting surface and specifically on the surface roughness, whose values need to be tuned for each particular application.

In this thesis a software tool based on a fractal model of the rough surfaces and a genetic algorithm approach to determine the optimum values of the parameters of the fractal model have been developed to obtain an accurate prediction of the contact resistance. Experimental results have proved the suitability of the proposed method, which can be applied to other electrical equipment.

In this thesis advanced **3D-FEM modelling tools** to perform realistic simulations to determine the thermal stresses at which substation connectors are subjected during **short-time and peak withstand current and temperature rise tests** have been developed.

Substation connectors must pass compulsory short-time withstand current test and peak withstand current test, which require very high-power laboratory facilities since they consume huge amounts of electrical power. Such tests are destructive and expensive and the customers frequently have to face long waiting times to do the tests. Therefore there is the need to develop specific software tools to simulate such tests in a realistic and economical manner. To this end, in this thesis an electromagnetic-thermal multiphysics 3D-FEM tool to simulate the transient thermal behavior of substation connectors during the standard short-circuit tests has been developed. Experimental results from standard short-circuit tests conducted in high-current laboratories have proved the suitability and accuracy of the proposed 3D-FEM model.

Moreover, temperature rise tests are time consuming, require the use of high-power-test-laboratory facilities, which are very expensive and consume large amounts of power. Therefore, it is crucial to dispose of a reliable tool also for predicting temperature rise tests results for substation connectors, especially during their design and improvement stages. In this thesis a transient numerical-FEM approach to simulate the temperature rise in high-capacity substation connectors has been presented, which shows accurate solution and allows avoiding the realization of preliminary factory tests, thus saving energy-related costs and time involved in planning and performing such tests. Experimental results have validated the feasibility and usefulness of the proposed methodology.

The realistic multiphysics methods proposed in this thesis to simulate short-time and peak withstand current and temperature rise tests allows satisfying the electrical and thermal requirements imposed by the compulsory standard tests, thus ensuring an adequate electromagnetic and thermal behavior of the connectors under study. These methods are also applicable to other connector types and power devices, which may be a valuable tool to assist the design process of substation connectors including those compatible with the HTLS technology.

Finally the thesis deals with **the loop inductance**, as reported in Appendix A. The inductance of the round nonmagnetic conductor forming a circular loop, which corresponds to the most typical testing loop configuration, has been analyzed under alternating current. The estimation of the loop inductance is very important since it determines voltage drop in conductors. Thus an increase of reactive power consumption limits conductor's ampacity and the current output capacity of the power transformers used to perform the tests. In addition an initial estimation of the loop inductance is required to determine the voltage set-point during the short-time withstand current and peak withstand current tests. The inductance estimated through formulas has been compared with FEM simulations and experimental measurements. Moreover, a simple setup to minimize the power requirements when conducting short-circuit tests, based on the reduction of reactive power consumption has been proposed in this thesis.

The device is based on placing a wired conductor forming a closed inner loop concentric with the testing loop. The decrease of reactive power is related to the effect of the mutual inductance between the inner and outer loops. Three-dimensional finite element method (3D-FEM) has been applied to optimize this problem, allowing changing the geometric and material properties of the inner loop.

References

- [1] CIGRE, "Coping with Limits for Very High Penetrations of Renewable Energy - Adaptation aux limites atteintes avec des pénétrations très importantes d'énergies renouvelables," *Electra* 527 - C1/C2/C6.18. pp. 74–79, 2013.
- [2] A. A. P. da Silva and J. M. de Barros Bezerra, "A Model for Uprating Transmission Lines by Using HTLS Conductors," *Power Delivery, IEEE Transactions on*, vol. 26, no. 4. pp. 2180–2188, 2011.
- [3] A. Gomez Exposito, J. R. Santos, and P. C. Romero, "Planning and Operational Issues Arising From the Widespread Use of HTLS Conductors," *Power Systems, IEEE Transactions on*, vol. 22, no. 4. pp. 1446–1455, 2007.
- [4] NEMA, "ANSI/NEMA CC 1: Electric Power Connection for Substations," 2009. [Online]. Available: https://global.ihs.com/doc_detail.cfm?document_name=ANSI%252FNEMA CC 1&item_s_key=00081224. [Accessed: 15-Oct-2015].
- [5] J. J.-A. J. J.-A. Wang, J. K. Chan, and J. A. Graziano, "The Lifetime Estimate for ACSR Single-Stage Splice Connector Operating at Higher Temperatures," *IEEE Trans. Power Deliv.*, vol. 26, no. 3, pp. 1317–1325, Jul. 2011.
- [6] M. G. Day and A. Hellawell, "The Microstructure and Crystallography of Aluminium-Silicon Eutectic Alloys," *Proc. R. Soc. London A Math. Phys. Eng. Sci.*, vol. 305, no. 1483, 1968.
- [7] G. E. TOTTEN, *Email a friend ASM Handbook Volume 4E: Heat Treating of Nonferrous Alloys*. A S M INTERNATIONAL, 2016.
- [8] A. M. A. Mohamed and F. H. Samuel, "A Review on the Heat Treatment of Al-Si-Cu/Mg Casting Alloys," in *Heat Treatment - Conventional and Novel Applications*, InTech, 2012.
- [9] M. H. Mulazimoglu, R. A. L. Drew, and J. E. Gruzleski, "The effect of strontium on the electrical resistivity and conductivity of aluminum-silicon alloys," *Metall. Trans. A*, vol. 18, no. 6, pp. 941–947.
- [10] N. N. Dzekster and V. V. Izmailov, "Some methods for improving aluminium contacts," in *Thirty-Sixth IEEE Conference on Electrical Contacts, and the Fifteenth International Conference on Electrical Contacts*, 1990, pp. 518–520.
- [11] Burndy, *Electrical Contacts: Principles and Applications*. CRC Press, 1999.
- [12] M. Braunovic, N. K. Myshkin, and V. V. Konchits, *Electrical Contacts: Fundamentals, Applications and Technology*. 2006.
- [13] T. Campbell, R. K. Kalia, A. Nakano, P. Vashishta, S. Ogata, and S. Rodgers, "Dynamics of Oxidation of Aluminum Nanoclusters using Variable Charge Molecular-Dynamics Simulations on Parallel Computers," *Phys. Rev. Lett.*, vol. 82, no. 24, pp. 4866–4869, Jun. 1999.
- [14] P. G. Slade, *Electrical Contacts*. CRC Press, 2014.
- [15] R. L. Jackson, "Generation, Transmission and Distribution, IEE Proceedings C," *Generation, Transmission and Distribution, IEE Proceedings C*, vol. 129, no. 4. pp. 177–184, 1982.
- [16] A. Oberg, A. Bohlin, and K. E. Olson, "The influence of Contact Surface Preparation on the Performance of Copper and Aluminium Connectors," in *16th ICEC*, 1992, p. 476.
- [17] M. Braunovic, "Evaluation of different contact-aid compounds for aluminum-to-copper connections," in *Thirty-Sixth IEEE Conference on Electrical Contacts, and the Fifteenth International Conference on Electrical Contacts*, 1990, pp. 509–517.
- [18] M. Braunovic, "Evaluation of different contact aid compounds for aluminum-to-copper connections," *IEEE Trans. Components, Hybrids, Manuf. Technol.*, vol. 15, no. 2, pp. 216–224, Apr. 1992.

- [19] J. Schlabbach and K. H. Rofalski, *Power System Engineering: Planning, Design, and Operation of Power Systems and Equipment*. Weinheim, Germany: WILEY-VCH Verlag GmbH & Co., 2008.
- [20] F. Capelli, J.-R. Riba, and D. Gonzalez, "Optimization of short-circuit tests based on finite element analysis," in *2015 IEEE International Conference on Industrial Technology (ICIT)*, 2015, pp. 1368–1374.
- [21] International Electrotechnical Commission, "IEC-60694. Common specifications for high-voltage switchgear and controlgear standards." p. 179, 1996.
- [22] International Electrotechnical Commission, "IEC 62271-1:2007. High-voltage switchgear and controlgear - Part 1: Common specifications." International Electrotechnical Commission, p. 252, 2007.
- [23] "ANSI C37.51a-2010 Switchgear - Metal-Enclosed Low-Voltage AC Power Circuit Breaker Switchgear Assemblies -Conformance Test Procedures." .
- [24] J. Qu, Q. Wang, J. Zhang, H. Zhao, G. Wu, and X. Li, "3-D Transient Finite-Element Analysis and Experimental Investigation of Short-Circuit Dynamic Stability for Air Circuit Breaker," *IEEE Trans. Components, Packag. Manuf. Technol.*, vol. PP, no. 99, pp. 1–1, 2015.
- [25] X. Guan, N. Shu, B. Kang, and M. Zou, "Multiphysics Analysis of Plug-In Connector Under Steady and Short Circuit Conditions," *IEEE Trans. Components, Packag. Manuf. Technol.*, vol. 5, no. 3, pp. 320–327, Mar. 2015.
- [26] R. Wilkins, T. Saengsuwan, and L. O'Shields, "Short-circuit tests on current-limiting fuses: modelling of the test circuit," *Gener. Transm. Distrib. IEE Proc. C*, vol. 140, no. 1, pp. 30–36, Jan. 1993.
- [27] ANSI/NEMA, "ANSI/NEMA CC1. Electric Power Connection for Substation." Rosslyn, Virginia, 2009.
- [28] "ANSI C119.4 Connectors for use between aluminum to aluminum and aluminum to cooper conductors designed for normal operation at or below 93 degree C and copper to copper conductors designed for normal operation at or below 100. degree C." 2011.
- [29] "IEC 62271-1:2007 | IEC Webstore." .
- [30] "IEC 61238-1 Ed. 2.0 b:2003, Compression and mechanical connectors for power cables for rated voltages up to 30 kV (Um = 36 kV) – Part 1: Test methods and requirements," 2003.
- [31] *Increasing Capacity of Overhead Transmission Lines; Needs and Solutions*. 2010.
- [32] "Guide for Qualifying High Temperature Conductors for Use on Overhead Transmission Lines," 2010.
- [33] "High-Temperature, Low-Sag Transmission Conductors," 2002.
- [34] *WG B2.55 Conductors for the Uprating of Existing Overhead Lines* . .
- [35] J.R. Davis & Associates. and ASM International. Handbook Committee., *Aluminum and aluminum alloys*. ASM International, 1993.
- [36] W. D. Callister and D. G. Rethwisch, *Fundamentals of materials science and engineering*, vol. 21. Wiley New York, 2013.
- [37] M. M. Makhlof and H. V. Guthy, "The aluminum–silicon eutectic reaction: mechanisms and crystallography," *J. Light Met.*, vol. 1, no. 4, pp. 199–218, 2001.
- [38] C.-A. Gandin, "Experimental Study of the Transition from Constrained to Unconstrained Growth during Directional Solidification.," *ISIJ Int.*, vol. 40, no. 10, pp. 971–979, 2000.
- [39] S. G. Shabestari and H. Moemeni, "Effect of copper and solidification conditions on the microstructure and mechanical properties of Al–Si–Mg alloys," *J. Mater. Process. Technol.*, vol. 153, pp. 193–198, 2004.
- [40] K. T. Kashyap, S. Murali, K. S. Raman, and K. S. S. Murthy, "Casting and heat treatment variables of Al–7Si–Mg alloy," *Mater. Sci. Technol.*, vol. 9, no. 3, pp. 189–204, Mar. 1993.
- [41] P. B. Crosley and L. F. Mondolfo, "The modification of aluminum-silicon alloys," *Mod Cast*, vol. 49,

- no. 3, pp. 99–100, 1966.
- [42] S. A. Kori, B. S. Murty, and M. Chakraborty, “Development of an efficient grain refiner for Al–7Si alloy and its modification with strontium,” *Mater. Sci. Eng. A*, vol. 283, no. 1, pp. 94–104, 2000.
- [43] L. Heusler and W. Schneider, “Influence of alloying elements on the thermal analysis results of Al–Si cast alloys,” *J. Light Met.*, vol. 2, no. 1, pp. 17–26, 2002.
- [44] A. M. Gokhale and G. R. Patel, “Analysis of variability in tensile ductility of a semi-solid metal cast A356 Al-alloy,” *Mater. Sci. Eng. A*, vol. 392, no. 1, pp. 184–190, 2005.
- [45] X. Jian, H. Xu, T. T. Meek, and Q. Han, “Effect of power ultrasound on solidification of aluminum A356 alloy,” 2005.
- [46] W. F. (William F. Smith, *Structure and properties of engineering alloys*. McGraw-Hill, 1981.
- [47] J. F. Hernandez Paz, © Juan, and F. Hernandez Paz, “Heat Treatment and Precipitation in A356 Aluminum Alloy,” 2003.
- [48] S. Shivkumar, S. Ricci, C. Keller, and D. Apelian, “Effect of solution treatment parameters on tensile properties of cast aluminum alloys,” *J. Heat Treat.*, vol. 8, no. 1, pp. 63–70, Mar. 1990.
- [49] P. Ji-Hua, X.-L. Tang, J.-T. He, and X. De-Ying, “Effect of heat treatment on microstructure and tensile properties of A356 alloys.”
- [50] J. E. Gruzleski, B. M. Closset, and A. F. Society, “The treatment of liquid aluminum-silicon alloys.” American Foundrymen’s Society, Inc., Des Plaines, IL, IL, p. xiii, 256, 1990.
- [51] S.-Z. Lu and A. Hellawell, “The mechanism of silicon modification in aluminum-silicon alloys: Impurity induced twinning,” *Metall. Trans. A*, vol. 18, no. 10, pp. 1721–1733, Oct. 1987.
- [52] M. H. Mulazimoglu, R. A. L. Drew, and J. E. Gruzleski, “The electrical conductivity of cast Al–Si alloys in the range 2 to 12.6 wt pct silicon,” *Metall. Trans. A*, vol. 20, no. 3, pp. 383–389, Mar. 1989.
- [53] J. R. (Joseph R. . Davis, *Tensile testing*. ASM International, 2004.
- [54] R. Franz and G. Wiedemann, “Ueber die Wärme-Leitungsfähigkeit der Metalle,” *Ann. der Phys. und Chemie*, vol. 165, no. 8, pp. 497–531, 1853.
- [55] P. G. Slade, “Front Matter,” in *Electrical Contacts*, CRC Press, 2014, p. FM1-xliv.
- [56] “IEEE Std 1283-2013 (Revision of IEEE Std 1283-2004),” *IEEE Std 1283-2013 (Revision of IEEE Std 1283-2004)*. pp. 1–47, 2013.
- [57] F. Capelli, J.-R. Riba, A. Rodriguez, and S. Lalaouna, “Research Towards Energy-Efficient Substation Connectors,” in *3rd International Congress on Energy Efficiency and Energy Related Materials (ENEFM2015)*, 2016.
- [58] M. Leidner, H. Schmidt, and M. Myers, “Simulation of the Current Density Distribution within Electrical Contacts,” in *2010 Proceedings of the 56th IEEE Holm Conference on Electrical Contacts*, 2010, pp. 1–9.
- [59] M. Ciavarella, G. Murolo, and G. Demelio, “The electrical/thermal conductance of rough surfaces—the Weierstrass–Archard multiscale model,” *Int. J. Solids Struct.*, vol. 41, pp. 4107–4120, 2004.
- [60] C. Zhai, D. Hanaor, G. Proust, and Y. Gan, “Stress-Dependent Electrical Contact Resistance at Fractal Rough Surfaces,” *J. Eng. Mech.*, no. 5, p. B4015001, 2015.
- [61] R. Holm, *Electric Contacts - Theory and Application* Springer. New York: Springer-Verlag, 1967.
- [62] J. A. Greenwood and J. B. P. Williamson, “Contact of Nominally Flat Surfaces,” *Proc. R. Soc. A Math. Phys. Eng. Sci.*, vol. 295, no. 1442, pp. 300–319, Dec. 1966.
- [63] W. E. Wilson, S. V. Angadi, and R. L. Jackson, “Surface separation and contact resistance considering sinusoidal elastic–plastic multi-scale rough surface contact,” *Wear*, vol. 268, no. 1–2, pp. 190–201, Jan. 2010.
- [64] N. S. Noh Sung Kwak, J. Jongsoo Lee, and Y. H.-A.-B. C. of M. D. to M. E. C. R. Yong Hoon Jang, “Genetic-Algorithm-Based Controlling of Microcontact Distributions to Minimize Electrical

- Contact Resistance," *IEEE Trans. Components, Packag. Manuf. Technol.*, vol. 2, no. 11, pp. 1768–1776, Nov. 2012.
- [65] Z. Wang, W. Wang, Y. Hu, and H. Wang, "A Simplified Numerical Elastic-Plastic Contact Model for Rough Surfaces," in *Advanced Tribology*, Berlin, Heidelberg: Springer Berlin Heidelberg, 2009, pp. 159–166.
- [66] N. S. Noh Sung Kwak, J. Jongsoo Lee, and Y. H.-A.-B. C. of M. D. to M. E. C. R. Yong Hoon Jang, "Genetic-Algorithm-Based Controlling of Microcontact Distributions to Minimize Electrical Contact Resistance," *IEEE Trans. Components, Packag. Manuf. Technol.*, vol. 2, no. 11, pp. 1768–1776, Nov. 2012.
- [67] L. Kogut and K. Komvopoulos, "Electrical contact resistance theory for conductive rough surfaces," *J. Appl. Phys.*, vol. 94, no. 5, p. 3153, Aug. 2003.
- [68] ISO, "ISO 4287:1997 Geometrical Product Specifications (GPS) -- Surface texture: Profile method -- Terms, definitions and surface texture parameters." p. 25, 1997.
- [69] A. A. Akbari, A. M. Fard, and A. G. Chegini, "An Effective Image Based Surface Roughness Estimation Approach Using Neural Network," in *2006 World Automation Congress*, 2006, pp. 1–6.
- [70] A. . Baker and W. . Giardini, "Developments in Australia's surface roughness measurement system," *Int. J. Mach. Tools Manuf.*, vol. 41, no. 13, pp. 2087–2093, 2001.
- [71] F. F. Ling, "On Asperity Distributions of Metallic Surfaces," *J. Appl. Phys.*, vol. 29, no. 8, p. 1168, Jun. 1958.
- [72] L. H. Tanner and M. Fahoum, "A study of the surface parameters of ground and lapped metal surfaces, using specular and diffuse reflection of laser light," *Wear*, vol. 36, no. 3, pp. 299–316, Mar. 1976.
- [73] V. W. Antonetti, T. D. Whittle, and R. E. Simons, "An Approximate Thermal Contact Conductance Correlation," *J. Electron. Packag.*, vol. 115, no. 1, p. 131, Mar. 1993.
- [74] M. A. Lambert and L. S. Fletcher, "Thermal Contact Conductance of Spherical Rough Metals," *J. Heat Transfer*, vol. 119, no. 4, p. 684, Nov. 1997.
- [75] M. G. Cooper, B. B. Mikic, and M. M. Yovanovich, "Thermal contact conductance," *Int. J. Heat Mass Transf.*, vol. 12, no. 3, pp. 279–300, Mar. 1969.
- [76] H. Kanter, "Slow-Electron Mean Free Paths in Aluminum, Silver, and Gold," *Phys. Rev. B*, vol. 1, no. 2, pp. 522–536, Jan. 1970.
- [77] R. Holm, *Electric Contacts*. Berlin, Heidelberg: Springer Berlin Heidelberg, 1967.
- [78] A. Banerji, *Fractal Symmetry of Protein Exterior*. Pune, India: Springer Basel, 2013.
- [79] C. G. Vayenas, R. E. White, and M. E. Gamboa-Aldeco, Eds., *Modern Aspects of Electrochemistry*, vol. 42. New York, NY: Springer New York, 2008.
- [80] X. Yin and K. Komvopoulos, "An adhesive wear model of fractal surfaces in normal contact," *Int. J. Solids Struct.*, vol. 47, no. 7, pp. 912–921, 2010.
- [81] J. A. Greenwood, "Constriction resistance and the real area of contact," *Br. J. Appl. Phys.*, vol. 17, no. 12, pp. 1621–1632, Dec. 1966.
- [82] M. Nakamura and I. Minowa, "Computer Simulation for the Conductance of a Contact Interface," *IEEE Trans. Components, Hybrids, Manuf. Technol.*, vol. 9, no. 2, pp. 150–155, Jun. 1986.
- [83] B. Mikic, "Analytical Studies of Contact of Nominally Flat Surfaces; Effect of Previous Loading," *J. Lubr. Technol.*, vol. 93, no. 4, p. 451, Nov. 1971.
- [84] B. B. Mikić, "Thermal contact conductance; theoretical considerations," *Int. J. Heat Mass Transf.*, vol. 17, no. 2, pp. 205–214, Feb. 1974.
- [85] M. M. Yovanovich, "Thermal contact correlations," *Am. Inst. Aeronaut. Astronaut.*, pp. 83–95, 1982.
- [86] M. M. Yovanovich, "Four decades of research on thermal contact, gap, and joint resistance in microelectronics," *IEEE Trans. Components Packag. Technol.*, vol. 28, no. 2, pp. 182–206, Jun.

- 2005.
- [87] G. Zavarise and D. Boso, "Electro-mechanical problems in superconducting coils." 05-Oct-2002.
 - [88] M. Bahrami, J. R. Culham, M. M. Yananovich, and G. E. Schneider, "Review of Thermal Joint Resistance Models for Nonconforming Rough Surfaces," *Appl. Mech. Rev.*, vol. 59, no. 1, p. 1, Jan. 2006.
 - [89] K. Komvopoulos and N. Ye, "Three-Dimensional Contact Analysis of Elastic-Plastic Layered Media With Fractal Surface Topographies," *J. Tribol.*, vol. 123, no. 3, p. 632, 2001.
 - [90] H. E. House and P. D. Tuttle, "Current-Carrying Capacity of ACSR," *Trans. Am. Inst. Electr. Eng. Part III Power Appar. Syst.*, vol. 77, no. 3, pp. 1169–1173, Apr. 1958.
 - [91] V. T. Morgan, "The thermal rating of overhead-line conductors Part I. The steady-state thermal model," *Electr. Power Syst. Res.*, vol. 5, no. 2, pp. 119–139, Jun. 1982.
 - [92] "The thermal behaviour of overhead conductors. Section 1 and 2: mathematical model for evaluation of conductor temperature in the steady state and the application thereof," 1992.
 - [93] "IEEE Standard for Calculating the Current-Temperature of Bare Overhead Conductors." pp. c1-59, 2007.
 - [94] A. Arroyo, P. Castro, R. Martinez, M. Manana, A. Madrazo, R. Lecuna, and A. Gonzalez, "Comparison between IEEE and CIGRE Thermal Behaviour Standards and Measured Temperature on a 132-kV Overhead Power Line," *Energies*, vol. 8, no. 12, pp. 13660–13671, Dec. 2015.
 - [95] A. A. P. Silva and J. M. B. Bezerra, "Applicability and limitations of ampacity models for HTLS conductors," *Electr. Power Syst. Res.*, vol. 93, pp. 61–66, 2012.
 - [96] E. Buckingham, "On Physically Similar Systems; Illustrations of the Use of Dimensional Equations," *Phys. Rev.*, vol. 4, no. 4, pp. 345–376, Oct. 1914.
 - [97] N. P. Schmidt, "Comparison between IEEE and CIGRE ampacity standards," *IEEE Trans. Power Deliv.*, vol. 14, no. 4, pp. 1555–1559, 1999.
 - [98] T. Takahashi, T. Ito, T. Okamoto, and T. Imajo, "Development of calculation system for transient temperature rise of power cables in protection pipe," in *IEEE/PES Transmission and Distribution Conference and Exhibition*, 2002, vol. 3, pp. 1899–1904.
 - [99] L. Yanmu, L. Yongchun, L. Yanming, S. Wenrong, Y. Peng, L. Junhao, Y. Y. Li, Y. Liang, Y. Y. Li, W. Si, P. Yuan, and J. Li, "Coupled Electromagnetic-Thermal Modeling the Temperature Distribution of XLPE Cable," in *Power and Energy Engineering Conference, 2009. APPEEC 2009. Asia-Pacific*, 2009, pp. 1–4.
 - [100] Jeong-Hoon Yoon, Heui-Sub Ahn, Jongung Choi, Il-Sung Oh, J.-H. Yoon, H.-S. Ahn, J. Choi, and I.-S. Oh, "An Estimation Technology of Temperature Rise in GIS Bus Bar using Three-Dimensional Coupled-Field Multiphysics," in *Conference Record of the 2008 IEEE International Symposium on Electrical Insulation*, 2008, pp. 432–436.
 - [101] K. Hameyer, J. Driesen, H. De Gersem, and R. Belmans, "The classification of coupled field problems," *IEEE Trans. Magn.*, vol. 35, no. 3, pp. 1618–1621, May 1999.
 - [102] G. Buonanno, "Effect of radiative and convective heat transfer on thermal transients in power cables," *IEE Proc. - Gener. Transm. Distrib.*, vol. 142, no. 4, p. 436, 1995.
 - [103] S. W. Kim, H. H. Kim, S. C. Hahn, B. Y. Lee, K. Y. Park, Y. J. Shin, W. P. Song, J. B. Kim, and I. H. Shin, "Coupled finite-element-analytic technique for prediction of temperature rise in power apparatus," *IEEE Trans. Magn.*, vol. 38, no. 2, pp. 921–924, Mar. 2002.
 - [104] S. W. Churchill and H. H. S. Chu, "Correlating equations for laminar and turbulent free convection from a horizontal cylinder," *Int. J. Heat Mass Transf.*, vol. 18, no. 9, pp. 1049–1053, Sep. 1975.
 - [105] J. Hernández-Guiteras, J.-R. Riba, and L. Romeral, "Improved design of an extra-high-voltage expansion substation connector through magnetic field analysis," *Simul. Model. Pract. Theory*, vol. 43, pp. 96–105, Apr. 2014.
 - [106] J. C. Maxwell and T. F. Torrance, *A dynamical theory of the electromagnetic field*. 1982.

- [107] J.-R. Riba, "Analysis of formulas to calculate the AC resistance of different conductors' configurations," *Electr. Power Syst. Res.*, vol. 127, pp. 93–100, Oct. 2015.
- [108] S. O. Kasap, *Principles of Electronic Materials and Devices*. McGraw-Hill, 2006.
- [109] IEC, "IEC 60287-1-1:2006. Electric cables - Calculation of the current rating - Part 1-1: Current rating equations (100 % load factor) and calculation of losses - General." p. 65, 2006.
- [110] M. N. Özişik, *Heat Transfer: A Basic Approach*. McGraw-Hill, 1985.
- [111] L. Acevedo, S. Usón, and J. Uche, "Numerical study of cullet glass subjected to microwave heating and SiC susceptor effects. Part I: Combined electric and thermal model," *Energy Convers. Manag.*, vol. 97, pp. 439–457, Jun. 2015.
- [112] E. Fernandez, E. Torres, I. Zamora, A. J. Mazon, and I. Albizu, "Thermal model for current limiting fuses installed in vertical position," *Electr. Power Syst. Res.*, vol. 107, pp. 167–174, Feb. 2014.
- [113] S. Kakaç and Y. Yener, *Convective Heat Transfer, Second Edition*. CRC Press, 1994.
- [114] B. Yu, S. Zhang, J. Yan, L. Cheng, and P. Zheng, "Thermal Analysis of a Novel Cylindrical Transverse-Flux Permanent-Magnet Linear Machine," *Energies*, vol. 8, no. 8, pp. 7874–7896, Jul. 2015.
- [115] J. H. Lienhard, *A Heat Transfer Textbook: Fourth Edition*. Courier Corporation, 2013.
- [116] A. Bejan, *Convection Heat Transfer*. John Wiley & Sons, 2013.
- [117] T. H. Kuehn and R. J. Goldstein, "Correlating equations for natural convection heat transfer between horizontal circular cylinders," *Int. J. Heat Mass Transf.*, vol. 19, no. 10, pp. 1127–1134, Oct. 1976.
- [118] V. T. Morgan and V. T., "The overall convective heat transfer from smooth circular cylinders," *Adv. heat Transf. Vol. 11. (A76-17076 05-34) New York, Acad. Press. Inc., 1975, p. 199-264.*, vol. 11, pp. 199–264, 1975.
- [119] F. Wamsler, "Die Wärmeabgabe geheizter Körper an Luft," *Ver Deut Ing Forschunash*, p. 98/99.
- [120] R. M. Fand, E. W. Morris, and M. Lum, "Natural convection heat transfer from horizontal cylinders to air, water and silicone oils for rayleigh numbers between 3×10^2 and 2×10^7 ," *Int. J. Heat Mass Transf.*, vol. 20, no. 11, pp. 1173–1184, 1977.
- [121] W. H. McAdams, *Heat Transmission*. 1954.
- [122] F. Yang, W. Ran, T. Chen, and X. Luo, "Investigation on the Factors Affecting the Temperature in Urban Distribution Substations and an Energy-Saving Cooling Strategy," *Energies*, vol. 4, no. 12, pp. 314–323, Feb. 2011.
- [123] IEEE, "IEEE Standard for Calculating the Current-Temperature of Bare Overhead Conductors." pp. c1-59, 2007.
- [124] J. Zhao, C. Cheng, Y. Song, W. Liu, Y. Liu, K. Xue, Z. Zhu, Z. Yang, D. Wang, and M. Yang, "Heat Transfer Analysis of Methane Hydrate Sediment Dissociation in a Closed Reactor by a Thermal Method," *Energies*, vol. 5, no. 12, pp. 1292–1308, May 2012.
- [125] C. S. Taylor and H. E. House, "Emissivity and Its Effect on the Current-Carrying Capacity of Stranded Aluminum Conductors [includes discussion]," *Trans. Am. Inst. Electr. Eng. Part III Power Appar. Syst.*, vol. 75, no. 3, Jan. 1956.
- [126] International Energy Agency, "Key World Energy Statistics 2015," Paris, France, 2015.
- [127] H. Li, A. Bose, and Y. Zhang, "On-line short-circuit current analysis and preventive control to extend equipment life," *IET Gener. Transm. Distrib.*, vol. 7, no. 1, pp. 69–75, Jan. 2013.
- [128] H. Wu, L. Yuan, L. Sun, and X. Li, "Modeling of Current-Limiting Circuit Breakers for the Calculation of Short-Circuit Current," *IEEE Trans. Power Deliv.*, vol. 30, no. 2, pp. 652–656, Apr. 2015.
- [129] M. Tartaglia and M. Mitolo, "An Analytical Evaluation of the Prospective I_{2t} to Assess Short-Circuit Capabilities of Cables and Busways," *IEEE Trans. Power Deliv.*, vol. 25, no. 3, pp. 1334–1339, Jul. 2010.

- [130] A. Palani, S. Santhi, S. Gopalakrishna, and V. Jayashankar, "Real-Time Techniques to Measure Winding Displacement in Transformers During Short-Circuit Tests," *IEEE Trans. Power Deliv.*, vol. 23, no. 2, pp. 726–732, Apr. 2008.
- [131] T. Takahashi, T. Ito, T. Okamoto, and T. Imajo, "Development of calculation system for transient temperature rise of power cables in protection pipe," in *IEEE/PES Transmission and Distribution Conference and Exhibition*, 2002, vol. 3, pp. 1899–1904.
- [132] Y. Y. Li, Y. Liang, Y. Y. Li, W. Si, P. Yuan, and J. Li, "Coupled Electromagnetic-Thermal Modeling the Temperature Distribution of XLPE Cable," in *2009 Asia-Pacific Power and Energy Engineering Conference*, 2009, pp. 1–4.
- [133] Jeong-Hoon Yoon, Heui-Sub Ahn, Jongung Choi, and Il-Sung Oh, "An Estimation Technology of Temperature Rise in GIS Bus Bar using Three-Dimensional Coupled-Field Multiphysics," in *Conference Record of the 2008 IEEE International Symposium on Electrical Insulation*, 2008, pp. 432–436.
- [134] Y. Spaeck-Leigsnering, E. Gjonaj, H. De Gerssem, T. Weiland, M. Giebel, and V. Hinrichsen, "Electro-Quasistatic-Thermal Modeling and Simulation of Station Class Surge Arresters," *IEEE Trans. Magn.*, vol. PP, no. 99, pp. 1–1, 2015.
- [135] C. Liao, J. Ruan, C. Liu, W. Wen, and Z. Du, "3-D Coupled Electromagnetic-Fluid-Thermal Analysis of Oil-Immersed Triangular Wound Core Transformer," *IEEE Trans. Magn.*, vol. 50, no. 11, pp. 1–4, Nov. 2014.
- [136] A. Arroyo, P. Castro, R. Martinez, M. Manana, A. Madrazo, R. Lecuna, and A. Gonzalez, "Comparison between IEEE and CIGRE Thermal Behaviour Standards and Measured Temperature on a 132-kV Overhead Power Line," *Energies*, vol. 8, no. 12, pp. 13660–13671, Dec. 2015.
- [137] X. Li, J. Qu, Q. Wang, H. Zhao, and D. Chen, "Numerical and Experimental Study of the Short-Time Withstand Current Capability for Air Circuit Breaker," *IEEE Trans. Power Deliv.*, vol. 28, no. 4, pp. 2610–2615, Oct. 2013.
- [138] IEEE, "IEEE Std C37.20.1-2015 (Revision of IEEE Std C37.20.1-2002). IEEE Standard for Metal-Enclosed Low-Voltage (1000 Vac and below, 3200 Vdc and below) Power Circuit Breaker Switchgear," *IEEE Std C37.20.1-2015 (Revision of IEEE Std C37.20.1-2002)*. IEEE, pp. 1–84, 2015.
- [139] IEEE, "IEEE Std C37.13.1-2006. IEEE Standard for Definite-Purpose Switching Devices for Use in Metal-Enclosed Low-Voltage Power Circuit Breaker Switchgear," *IEEE Std C37.13.1-2006*. IEEE, pp. c1-18, 2006.
- [140] Y. Geng, J. Yan, Z. Liu, and J. Yao, "Development of a 126kV single-break vacuum circuit breaker and type test," in *2013 2nd International Conference on Electric Power Equipment - Switching Technology (ICEPE-ST)*, 2013, pp. 1–4.
- [141] C. Holyk, H.-D. Liess, S. Grondel, H. Kanbach, and F. Loos, "Simulation and measurement of the steady-state temperature in multi-core cables," *Electr. Power Syst. Res.*, vol. 116, pp. 54–66, Nov. 2014.
- [142] G. K. Soulinaris, C. D. Halevidis, A. D. Polykrati, and P. D. Bourkas, "Evaluation of the thermal stresses and dielectric phenomena in the investigation of the causes of wildfires involving distribution power lines," *Electr. Power Syst. Res.*, vol. 117, pp. 76–83, Dec. 2014.
- [143] Comsol, "COMSOL 4.3 Multiphysics User's Guide." COMSOL, p. 1292, 2012.
- [144] C. Öhman, "Emittansmätningar med AGEMA E-Box. Teknisk rapport, AGEMA." 1999.
- [145] International Electrotechnical Commission, "IEC 61238-1:2003. Compression and mechanical connectors for power cables for rated voltages up to 30 kV (Um = 36 kV) - Part 1: Test methods and requirements." p. 115, 2003.
- [146] "ANSI/NEMA CC1. Electric Power Connection for Substation." Rosslyn, Virginia, 2009.
- [147] Y. Li, Y. Liang, Y. Li, W. Si, P. Yuan, and J. Li, "Coupled Electromagnetic-Thermal Modeling the Temperature Distribution of XLPE Cable," in *2009 Asia-Pacific Power and Energy Engineering*

- Conference*, 2009, pp. 1–4.
- [148] M. P. Paisios, C. G. Karagiannopoulos, and P. D. Bourkas, “Estimation of the temperature rise in cylindrical conductors subjected to heavy 10/350 μ s lightning current impulses,” *Electr. Power Syst. Res.*, vol. 78, no. 1, pp. 80–87, Jan. 2008.
- [149] M. Terracciano, S. Purushothaman, and F. de León, “Calculation of cable thermal rating considering non-isothermal earth surface,” *IET Gener. Transm. Distrib.*, vol. 8, no. 7, pp. 1354–1361, Jul. 2014.
- [150] “IEC 60287-1-1. Electric cables – Calculation of current rating – Part 1: Current rating equations (100% load factor) and calculation of losses.” 2006.
- [151] F. Capelli, J.-R. Riba, A. Rodriguez, and S. Lalaouna, “Research Towards Energy-Efficient Substation Connectors,” in *3rd International Congress on Energy Efficiency and Energy Related Materials (ENEFM2015)*, Springer, 2016.
- [152] Flir, “Flir i3 user’s manual,” Flir, 2011.
- [153] R. K.-H. Schlabbach J., “Wiley: Power System Engineering: Planning, Design, and Operation of Power Systems and Equipment - Juergen Schlabbach, Karl-Heinz Rofalski.” .
- [154] “IEC-60694-Common-Specifications-for-High-Voltage-Switch-Gear-and-Control-Gear-Standards.pdf - Uploady.com.” .
- [155] R. Wilkins, T. Saengsuwan, and L. O’Shields, “Short-circuit tests on current-limiting fuses: modelling of the test circuit,” vol. 140, no. 1, Jan. 1993.
- [156] J. C. Maxwell, *A Treatise on Electricity and Magnetism Volume 1*. Cambridge University Press, 2010.
- [157] F. W. Grover, *Inductance Calculations: Working Formulas and Tables*. Mineola, New York: Dover Publications, 1946.
- [158] H. Dwight, *Electrical coils and conductors, their electrical characteristics and theory.*, 1st ed. New York London: McGraw-Hill Book Co., 1945.
- [159] S. I. Babic, F. Sirois, and C. Akyel, “VALIDITY CHECK OF MUTUAL INDUCTANCE FORMULAS FOR CIRCULAR FILAMENTS WITH LATERAL AND ANGULAR MISALIGNMENTS,” *Prog. Electromagn. Res. M*, vol. 8, pp. 15–26, 2009.
- [160] Farhana Mohamad Yusop, M. K. M. Jamil, D. Ishak, M. Husaini, and S. Masri, “Investigation of electromagnetic force during short-circuit test in three-phase busbar system,” in *2011 IEEE Colloquium on Humanities, Science and Engineering*, 2011, pp. 340–344.
- [161] “Abstract—Electromagnetic forces on three-phase five-wire.”
- [162] W. S. Peterson and H. J. McCracken, “Movements of Overhead Line Conductors During Short Circuits,” *Trans. Am. Inst. Electr. Eng.*, vol. 48, no. 1, pp. 67–90, Jan. 1929.
- [163] P. L. Dowell, “Effects of eddy currents in transformer windings,” *Proc. Inst. Electr. Eng.*, vol. 113, no. 8, p. 1387, 1966.
- [164] D. A., “Extra losses caused in high current conductors by skin and proximity effects.,” *Cahier Technique, n.83, Cahier Technique Schneider Electric*, 1983.

Appendix

A. Inductance of the testing loop

One of the main problems that arise when performing short-circuit tests to large loops involving substation connectors is the inductive component of the loop impedance. Transformers used to perform short-circuit tests have a secondary winding with very few turns, producing a very low output voltage. The increase in the reactive component of the impedance, which is related to loop size, limits the current output capacity, because the reactive component tends to saturate the output of the transformer and absorbs large amounts of reactive power.

In this thesis the inductance of the most typical testing loop configuration (round nonmagnetic conductor forming circular loop) under alternating current (AC) supply has been analyzed, since it significantly determines the voltage drop in conductors, thus increasing reactive power consumption, limiting conductor's ampacity and the current output capacity of the power transformers used to perform the tests.

Moreover, a simple method to minimize the power requirements when conducting short-circuit tests, based on the reduction of reactive power consumption has been studied. It is based on placing a round conductor forming a closed inner loop concentric with the testing loop. The decrease of reactive power is related to the effect of the mutual inductance between the inner and outer loops.

Calculation of the inductance of conductive nonmagnetic conductors: round conductor forming a circular loop

The most common shape of testing loops involving substation connectors is almost circular. Therefore this configuration (see Fig. A-1) has been considered to estimate the inductance of the testing loops involving substation connectors.

In the technical literature there is not an exact closed-form solution for the inductance of a round conductor forming a circular loop which takes into account the eddy currents induced.

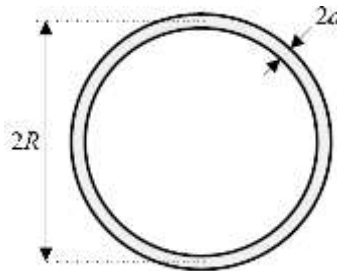


Figure 0.1. Round conductor forming a circular loop

However, an approximate formula for the total self-inductance in H/m which assumes an azimuthal current in a ring of major radius R with circular cross-section of radius a is given by:

$$L = \mu_0 \cdot R \cdot \left\{ \left[1 + \frac{2y+1}{8} \cdot (a/R)^2 \right] \cdot \ln \frac{8R}{a} - \frac{7}{4} + \frac{(y-1) \cdot (y-\frac{2}{3})}{16} \cdot (a/R)^2 \right\} \quad (\text{A.1})$$

where $y = 0$ for uniform current distribution, that is, low frequency operation, whereas $y = 1$ corresponds to the natural current distribution.

The results provided by formula (A.1) have been compared with those attained through two-dimensional finite element method (FEM) simulation and experimental measurements on a loop composed by substation connectors and HTLS conductor.

Results

Comparison with 2D-FEM simulations

In this section FEM simulations are taken as the reference method due to the flexibility and accuracy they provide and because in the technical literature is difficult to find internationally recognized experimental inductance measurements of the simple geometries analyzed in this work. Therefore, the results provided by the analytical formula are compared with the results obtained from FEM simulations at different frequencies.

The inductance of a circular loop of round conductor is analyzed for a particular geometry in which $a = 5$ mm, $R = 20$ mm as detailed in Figs A-2, where results provided by analytical formula and FEM simulations are shown.

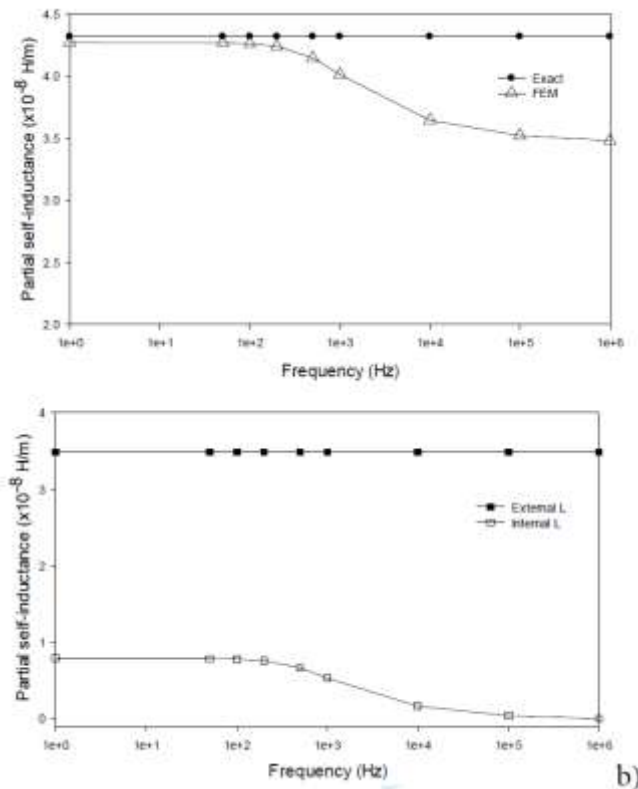


Figure 0.2. a) Total inductance obtained from the analytical formula (6.1) and FEM simulations of a circular loop of round conductor. $a = 5$ mm, $R = 20$ mm. b) External and internal partial-self inductances.

As shown in Figs. 6.7, the analytical formula given by Eq. (6.1) doesn't take into account eddy currents effects and, therefore, the average difference between FEM results and Eq. (6.1) at higher frequencies ($f= 1\text{MHz}$) is 9.2% for the total inductance. At low frequencies, where inductive effects are almost negligible, the formula shows good agreement with FEM results.

Comparison with experimental data

With the aim to validate the accuracy and the usefulness of formula (6.1) in practical application, inductance estimation provided by formula has been compared with result provided by experimental measurements.

Inductance measurements have been performed on a closed loop circuit of four substation connectors, as shown in Fig. A-3. The elements that compose the loop are:

- T-connector: S210ZTLS;
- Terminals: S210ZA4P23LS;
- Conductor ACSS LARK, with rated diameter $d = 20.5\text{ mm}$.

The substation connectors are from the SBI Connectors' catalogue. They connect ACSS LARK conductors of 20.5 mm diameter and 3 m length each one. The connectors are made of A356 cast aluminum alloy.

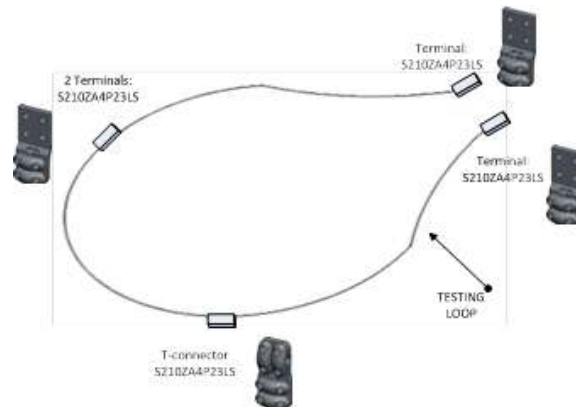


Figure 0.3. Experimental loop used to measure the conductor's inductance.

Inductance L (H/m) has been calculated as:

$$L = \frac{X}{2\pi f} \quad (\text{A.2})$$

Where f is the frequency of the power supply (50 Hz) and X is the total reactance of the testing loop, calculated from voltage V , current I and resistance R measurements of the loop, as shown in the following equation:

$$Z = \frac{V}{I} = \sqrt{R^2 + X^2} \quad (\text{A.3})$$

The AC waveform acquisitions of currents and voltages have been performed with an oscilloscope (Tektronix TPS 2024), whereas 4-wires resistance measurements by means of a micro-ohmmeter (Raytech Micro-Centurion).

For low-frequency application, the hypothesis of uniform current distribution is done.

Therefore equation A.1 becomes:

$$L = \mu_0 \cdot R \cdot \left\{ \left[1 + \frac{1}{8} \cdot (a/R)^2 \right] \cdot \ln \frac{8R}{a} - \frac{7}{4} + \frac{2}{16} \cdot (a/R)^2 \right\} \quad (\text{A.4})$$

Inductance measurements and estimation through eq. (A.4) are summarized and compared through Table A-1.

Table 0.1. Experimental and estimated values of loop inductance.

	Conductor radius a (m)	Loop radius R (m)	Inductance (H/m)	L
Formula (6.1)	0.0102	$4/\pi$	8.28 $\mu\text{H/m}$	
Experimental	-	-	8.11 $\mu\text{H/m}$	

It can be observed that approximate formula for the total self-inductance (A.1) allows estimating with a great accuracy the loop impedance of testing loops and, therefore, the power requirements to perform the short-circuit test.

Conclusion

In conclusion, it can be stated that the theoretical derivation of analytical formulas to calculate the inductance of different conductors' configurations offers technical difficulties even for simple geometries, especially when considering eddy currents effects. Although textbooks and lectures related to this topic usually include examples based on simple geometries, the theoretical analysis of variations of these examples is not trivial. Therefore a simulation system which allows obtaining accurate solutions have a great interest to estimate the inductance of the testing loop, and therefore the power requirements to perform short-circuit tests.

However, at low supply frequency (50 Hz) the comparison of the results provided by the formula with experimental data, shows that, when it is necessary a rough estimation of the loop inductance, the results provided by formula (A.1) is enough. It can predict the loop inductance in a rapid and effective manner, which results very useful in high power laboratories when rapid calculations on testing loops are needed. FEM simulations are usually computationally-intensive and time-consuming, thus being expensive and unpractical in the above mentioned application.

Optimization of short-circuit test based on finite-element analysis

Power systems have to be designed and tested to guarantee that devices involved can withstand the short-circuit current. Short-circuits produce both electromechanical and thermal effects, so when analyzing short-circuit consequences both effects must be considered [153]. Thus, power devices have to be tested and certified in accordance with IECs standards [154], which refer to the short-circuit tests as short-time withstand current and peak withstand current tests. However, short-circuit tests require the use of high-power-test-laboratory facilities, which are very expensive and consume large amounts of power [155]. Therefore, power requirements minimization in short-circuit tests is a challenging problem of great interest since it can help to reduce the cost of these expensive tests.

A simple setup to minimize the power requirements when conducting short-circuit tests for substation connectors is analyzed. Specifically, it is based on the reduction of the reactive power consumed during the test. One of the problems faced when performing short-circuit tests to large loops involving substation connectors is the inductive component of the impedance, which greatly increases with the loop size. Transformers specially designed to perform short-circuit tests usually have a secondary winding with very few turns, producing a very low output voltage. This increase in the reactive component of the impedance tends to saturate the output of the transformer used to perform these tests, therefore limiting the current output capacity of such transformer. The device is based on placing a wired conductor forming a closed inner loop (secondary or inner loop) concentric with the testing loop (primary or outer loop). The decrease of reactive power is related to the effect of the mutual inductance between the inner and outer loops, which can be considered as coaxial coils. The magnetic field produced by the testing loop interacts with the inner circuit, thus inducing a current flowing through the inner loop. Therefore there is a mutual induction between both circuits, which results in a reduction of the loop inductance and therefore in the reactive power demanded by the whole setup during the short-circuit test.

In the technical literature there are many studies analyzing the problem of mutual inductance calculation for coaxial circular coils [156]–[159][156], [157]. These contributions are based on the application of Maxwell's equations, Neumann's formula, and the Biot–Savart law. Moreover, many studies about the electrodynamics forces caused by short-circuit in busbars and conductors have been conducted [160]–[162]. However, no works dealing with the topic of this chapter are found.

Due to the testing loop, as well as the inner loop, are well-fastened to the ground, as recommended by IEC testing standards [2], it is ensured that, although high electromechanical forces are produced by short circuit currents, the clamps do not permit conductors' displacement. Thus, it can be asserted that, if electromechanical effects of short-circuit have to be evaluated, the presence of the inner loop would not influence test results.

Three-dimensional finite element method (3D-FEM) simulations are applied to optimize this problem, which allows changing the geometric and material properties of the inner loop and evaluating results for each case. The optimization process shows the potential of this method as a design tool to minimize the power requirements of short-circuits tests by optimizing the geometry of the experimental setup. Simulations allow minimizing the number of required experimental tests and the associated economic costs.

Testing Loop Setup

The object of this study is a closed loop circuit of four substation connectors, as shown in Fig. A-4. The elements that compose the loop are:

- T-connector: S210ZTLS;
- Terminals: S210ZA4P23LS;
- Conductor ACSS LARK, with rated diameter $d = 20.5$ mm.

The substation connectors are from the SBI Connectors' catalogue. They connect ACSS LARK conductors of 20.5 mm diameter and 3 m length each one. The connectors are made of A356 cast aluminum alloy.

With the aim to minimize the power requirements during the short-circuit test, by reducing the inductive load, a second closed loop, formed by a stranded cable, is placed concentric with the main loop as shown in Fig. A-4. The inner loop properties that determine its inductance and resistance (material, radius R , and wire diameter d) have been modified during the optimization process, with the aim to find optimal values.

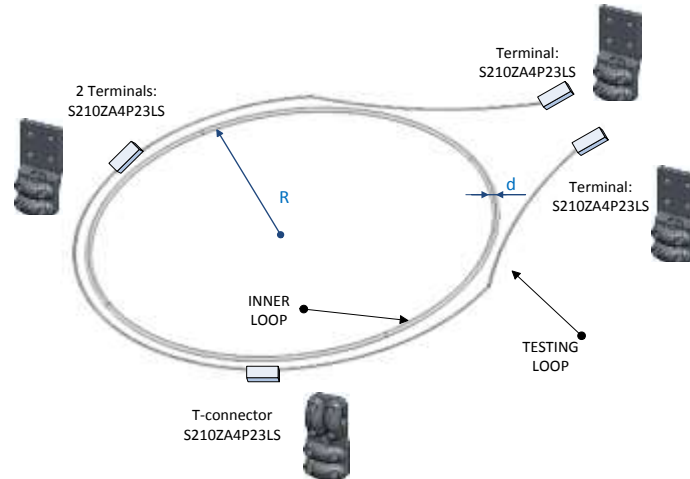


Figure 0.4. Optimization of short-circuit test. Testing loop setup.

The Fem Model

The finite element method is a versatile technique to solve partial differential equations over complex domains. The following subsection describes the electromagnetic equations applied in the FEM model to simulate the test loops.

Electromagnetic equations

The electromagnetic model used to solve the problem is the same described in section 5.3.1.

The main electric and magnetic parameters used in the 3D-FEM simulations are shown in Table A-2.

Table 0.2. Optimization of short-circuit test. Main Electric and Magnetic Parameters used in FEM simulations.

Parameter	Symbol	Units	Value
Free-space permeability	μ_0	NA^{-2}	$4\pi \cdot 10^{-7}$
Aluminum relative permeability	$\mu_{r,Al}$	-	1

Steel Core relative permeability	$\mu_{r,Fe}$	-	1
Copper relative permeability	$\mu_{r,Cu}$	-	1
Air relative permeability	$\mu_{r,air}$	-	1
Free-space permittivity	ϵ_0	$F\ m^{-1}$	$8.85 \cdot 10^{-12}$
Aluminum relative permittivity	$\epsilon_{r,Al}$	-	1
Steel Core relative permittivity	$\epsilon_{r,Fe}$	-	1
Copper relative permittivity	$\epsilon_{r,Cu}$	-	1
Air relative permittivity	$\epsilon_{r,air}$	-	1
Aluminum reference resistivity	ρ_{Al}	Ωm	$2.74 \cdot 10^{-8}$
Steel core reference resistivity	ρ_{Fe}	Ωm	$7.96 \cdot 10^{-6}$
Copper reference resistivity	ρ_{Cu}	Ωm	$1.68 \cdot 10^{-8}$
Reference Temperature	T_0	K	293.15
Aluminum temp. coefficient	α_{Al}	-	0.0041
Steel core temp. coefficient	α_{Fe}	-	0.0041
Copper temp. coefficient	α_{Cu}	-	0.0039

The 3D geometric model has been prepared and simplified to reduce its complexity and to minimize the computational burden without compromising results accuracy. The 3D geometry used in the FEM model doesn't consider the connectors since the electrical resistance of the connectors is way inferior to that of the conductor, so it can be considered negligible without affecting model accuracy. This assumption is supported by experimental measurements of the electrical resistance across the T-connector and along a length of one meter of the conductor. Resistance measurements were done by applying the 4-wires method between the points shown in Fig. A-5.

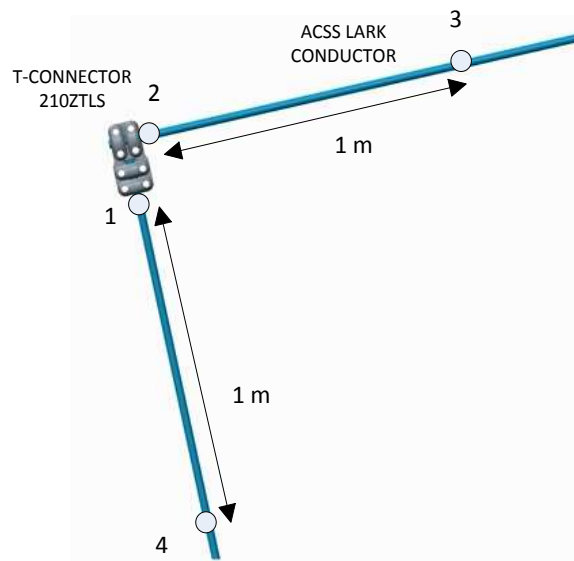


Figure 0.5. Reference scheme to measure the resistance of the T-connector and the ACSS Lark Conductor.

Table A-3 summarizes the results of the resistance measurements. The cable resistance has been measured along 1 m length; however the ACSS conductor has a total length of 12 m, so the connector resistance is negligible compared to the conductor resistance.

Table 0.3. Resistance measurements

Resistance Measurement			
Part	Reference points	Value	Unit
T-Connector	1-2	29.9	$\mu\Omega$
Lark Conductor	2-3 + 1-4	316	$\mu\Omega$

Thus, the external loop has been modeled as a single-turn conductor with circular cross-section and a total length of 12 m. It is composed by two materials, the steel core and the outer conductive part of aluminum. The inner loop has been modeled as a single-turn, whose radius, wire cross-section and wire material can be changed for optimization purposes.

The loops are considered, for simulations, a single-turn primary coil and single-turn secondary coil in a concentric coplanar arrangement. A three-dimensional sphere with radius of 2.5 m was used to model the surroundings air domain. The 3D geometry and mesh for simulation #5 are shown in Fig. A-6 and A-7, respectively.

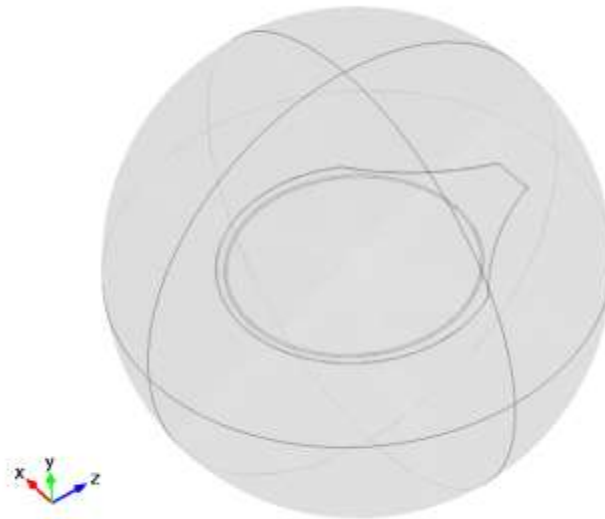


Figure 0.6. 3D modeled domain.

The external loop is modeled using the Single Turn Coil Domain feature of the Comsol® FEM package. A fixed voltage excites the outer single-turn coil, at a frequency of 50 Hz. The inner loop is also modeled using the Single Turn Coil Domain feature. To model the inner closed loop, the voltage drop across the coil is fixed at 0 V.

A full 3D model of the tested setup has been avoided due to the high computational resources required to perform the simulation. Therefore it was only simulated one-half of the model, taking

advantage of the existence of a planar symmetry (YZ axis) in the geometry, as shown in Fig. **¡Error! No se encuentra el origen de la referencia.**A-7.

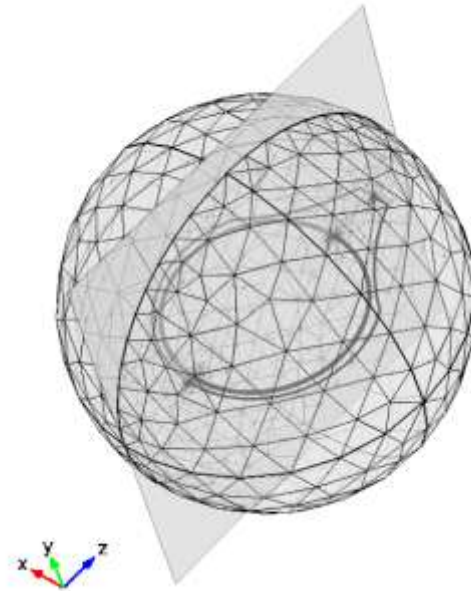


Figure 0.7. 3D mesh applied to the modeled domain.

Simulation Results

Different FEM simulations have been carried out to determine the most suitable configuration in order to minimize the inductive component of the impedance. For this purpose different loop configurations have been analyzed, which are summarized in Table A-4.

Table 0.4. Different loop configuration simulated.

Sim #	Inner loop configuration				Outer loop configuration		
	Loop radius (m)	Wire diameter d (mm)	Material	Applied voltage V_2 (V _{rms})	Wire diameter (mm)	Material	Applied voltage V_1 (V _{rms})
1	1.24	32	Aluminum	0	20.5	Aluminum/Steel	127.3
2	1.24	36	Aluminum	0	20.5	Aluminum/Steel	127.3
3	1.24	40	Aluminum	0	20.5	Aluminum/Steel	127.3
4	1.28	32	Aluminum	0	20.5	Aluminum/Steel	127.3
5	1.28	36	Aluminum	0	20.5	Aluminum/Steel	127.3
6	1.28	40	Aluminum	0	20.5	Aluminum/	127.3

						Steel	
7	1.24	32	Copper	0	20.5	Aluminum/ Steel	127.3
8	1.24	36	Copper	0	20.5	Aluminum/ Steel	127.3
9	1.24	30	Copper	0	20.5	Aluminum/ Steel	127.3
10	1.28	32	Copper	0	20.5	Aluminum/ Steel	127.3
11	1.28	36	Copper	0	20.5	Aluminum/ Steel	127.3
12	1.28	40	Copper	0	20.5	Aluminum/ Steel	127.3
13	Without inner loop				20.5	Aluminum/ Steel	127.3
14	Without inner loop				20.5	Aluminum/ Steel	147.1

In this section the results attained from the FEM electromagnetic simulations are presented.

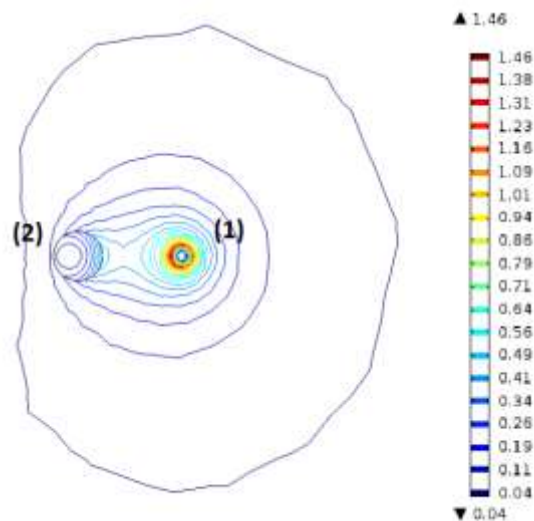


Figure 0.8. Distribution of the magnetic flux density B (T) around the outer active conductor (1) and the inner conductor (2).

Figure A-8 shows the magnetic flux distribution (B , T) distribution generated by both the inner and the active in the YZ symmetry plane where the coils are closer (simulation #5).

Figure A-9 shows the normal electrical current density in Amm^{-2} within both the outer active conductor and the inner conductor.

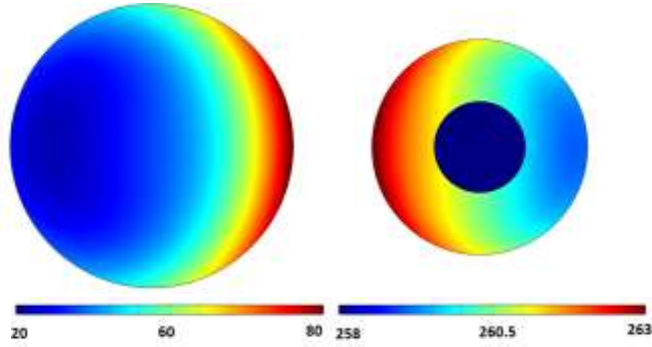


Figure 0.9. Normal current density distribution in A/mm² in the outer conductor. b) Current density distribution in the inner conductor.

Although the conductors' materials are assumed to be isotropic and the geometry perfectly symmetric, it can be observed that the current density distribution is not symmetrical across the conductors' cross-section. This phenomenon is due to the proximity effect [163], which is a consequence of electromagnetic interaction between both conductors, since the ac magnetic flux density generated by each conductor induces eddy currents in the other, thus affecting the current density. When the currents of the two nearby conductors have opposite directions, the current density is concentrated in the conductors' side closer to the nearby conductor and it is reduced in the opposite side [164], as shown in Fig. A-9.

Table A-5 summarizes the results of the FEM simulations of the fourteen analyzed loop configurations detailed in Table A-4. It shows the current I_1 in the outer active coil, the current induced in the inner coil I_2 , as well as the total apparent, active and reactive power absorbed by both loops. Note that the total apparent power in VA has been calculated as:

$$S = V_{1,rms} \cdot I_{1,rms} \quad (\text{A.5})$$

where $V_{1,rms}$ is the root-mean-square voltage in V and $I_{1,rms}$ the root-mean-square current in A of the outer active loop. The total active power P (W) was obtained by integrating the electromagnetic power loss along the analyzed volume (inner and outer loops). The total reactive power and the phase shift have been calculated as follows,

$$Q = \sqrt{S^2 - P^2} \quad (\text{A.6})$$

$$\varphi = \cos^{-1}(P/S) \quad (\text{A.7})$$

Table 0.5. Simulation Results

Sim #	Voltage	Current		Power			
	Exc. Volt. V_1 (V _{rms})	I_1 (kA _{rms})	I_2 (kA _{rms})	Apparent Power (MVA)	Active Power (MW)	Reactive Power (MVA _r)	Phase Shift (°)
1	127.3	38.68	19.19	4.9237	3.3068	3.6480	47.81
2	127.3	38.94	19.84	4.9559	3.3326	3.6681	47.74
3	127.3	39.07	21.26	4.9724	3.3566	3.6685	47.54
4	127.3	40.05	23.17	5.0980	3.5950	3.6146	45.16

5	127.3	40.42	24.68	5.1453	3.6358	3.6408	45.04
6	127.3	40.66	26.09	5.1756	3.6746	3.6448	44.77
7	127.3	38.92	19.96	4.9540	3.3142	3.6822	48.01
8	127.3	39.11	20.93	4.9780	3.3340	3.6966	47.95
9	127.3	39.24	22.44	4.9948	3.3646	3.6915	47.65
10	127.3	40.37	24.36	5.1391	3.6118	3.6557	45.35
11	127.3	40.64	25.95	5.1732	3.6536	3.6624	45.07
12	127.3	40.92	27.51	5.2087	3.6932	3.6730	44.84
13	127.3	35.05	-	4.4608	2.6336	3.6004	51.36
14	147.1	40.46	-	5.9501	3.5168	4.8996	51.37

Simulation results presented in Table A-5 prove that the effect of the inner loop (# 1-12) is to lower the phase shift between the voltage and current in the active loop, a clear prove that the inductive component of the impedance has been reduced when compared to cases #13 and #14, in which there is no inner loop. This tendency is more accentuated when the resistance of the inner loop decreases and the distance between the inner and outer loops lowers.

Comparing simulations #10 and #14, it is also important to note that, although the value of current flowing through the outer loop is the same, in the case #10 (with inner loop), the voltage applied is considerably lower, that is, to obtain a current of 40 kA, a typical value of short-circuit current for this kind of loop, it is necessary to apply 147.1 V_{rms} without internal loop (#14), whereas with inner loop only 127.3 V_{rms} (#10) are required. This behavior also involves a reduction of the reactive power and apparent power for the execution of the test. The reduction of the reactive power is about 25.4 %, from 4.8996 MVar (#14) to 3.6557 MVar (#10).

Experimental Results

In this section an experimental measurement is carried out to validate the simulation method. To this end, experimental rise temperature tests, according to the ANSI NEMA CC1 substation connectors' standard [4] are carried out, whose experimental setup is shown in Figs. A-10 and A-11.



Figure 0.10. Experimental test setup. Outer loop composed of an ACSS conductor, a T-connector S210ZTLS and four terminals S210ZA4P23LS. The internal loop is made of an aluminum stranded conductor with diameter of 32 mm.

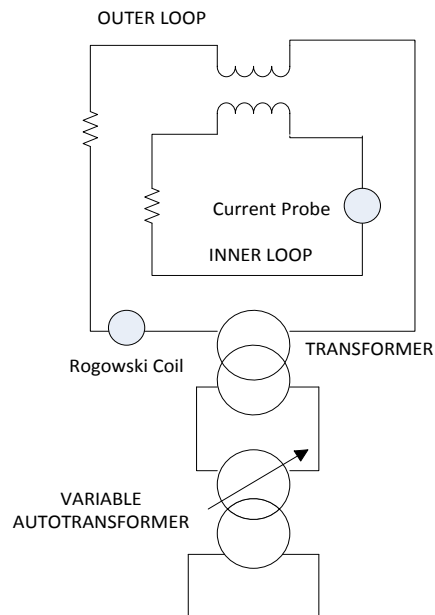


Figure 0.11. Electric diagram of the test setup.

The loop configuration is summarized in Table A-6. Therefore, an inner loop with 1.24 m radius using an aluminum wired conductor of 32 mm was tested.

Table 0.6. Test Setup. Loop Configuration.

Test #	Inner loop configuration				Outer loop configuration		
	Loop radius (m)	Wire diameter d (mm)	Mat.	Applied voltage V_2 (V _{rms})	Wire diameter (mm)	Mat.	Applied voltage V_1 (V _{rms})
A	1.24	32	Al	0	20.5	Al/ Steel	3.20

The experimental tests were performed at atmospheric conditions (28 °C, 982.7 hPa and 52.3% relative humidity). The experimental setup to conduct the temperature rise test is the same described in section 4.2.2.1.

The AC waveform acquisitions of currents and voltages have been performed with an oscilloscope (Tektronix TPS 2024). The phase shift between current and voltage in the active loop has been calculated by comparing both voltage and currents acquisitions of the oscilloscope during the test. The apparent power has been calculated by applying (A.5), and the total active and reactive powers have been calculated by applying (A.8) and (A.9).

$$P = S \cdot \cos\varphi \quad (\text{A.8})$$

$$Q = S \cdot \sin\varphi \quad (\text{A.9})$$

φ being the phase shift in °.

To measure the temperature in steady state condition, K-type thermocouples with an AISI 316 external sheath of 1 mm diameter were placed on the connectors' bodies and on the top points of each wire.

The loop configuration shown in Table A-6 was simulated with the same method detailed in section

Comparing values presented in Table A-7, it can be observed that differences between experimental and simulation results are lower than 3.7% for all variables simulated. Thus, the experimental results validated the feasibility and usefulness of the simulation method.

Table 0.7. Comparative results between simulations and the experimental test.

		Voltage	Current		Power			
		V_1 (V_{rms})	I_1 (A_{rms})	I_2 (A_{rms})	Apparent power (VA)	Active power (W)	Reactive power (VAr)	Phase shift (°)
Simul Test A		3.20	964	458	3088	2082	2280	47.6
Exp. Test. A		3.20	962	449	3078	2007	2335	49.3
Error Test A		-	0.2%	2%	0.3%	3.7%	2.4%	3.6%